4-15-2015 12:00 AM

Osteoarthritis Induced Glenoid Morphology and Bone Quality: An Evaluation of Augmented Glenoid Components

Nikolas K. Knowles
The University of Western Ontario

Supervisor
Dr. Louis M. Ferreira
The University of Western Ontario

Graduate Program in Mechanical and Materials Engineering
A thesis submitted in partial fulfillment of the requirements for the degree in Master of Engineering Science

Recommended Citation

Knowles, Nikolas K., "Osteoarthritis Induced Glenoid Morphology and Bone Quality: An Evaluation of Augmented Glenoid Components" (2015). *Electronic Thesis and Dissertation Repository*. 2752.
https://ir.lib.uwo.ca/etd/2752

OSTEOARTHRITIS INDUCED GLENOID MORPHOLOGY AND BONE QUALITY: AN EVALUATION OF AUGMENTED GLENOID COMPONENTS

(Thesis format: Integrated Article)

by

Nikolas Kelton Knowles

Graduate Program in Mechanical and Materials Engineering

A thesis submitted in partial fulfillment
of the requirements for the degree of
Master of Engineering Science

The School of Graduate and Postdoctoral Studies
The University of Western Ontario
London, Ontario, Canada

Abstract

Osteoarthritis of the glenoid results in regional bone density variations and bone loss that may compromise early component fixation and support. The two common morphologies, symmetric and asymmetric erosion, were characterized by bone density and morphology, and assessed on the basis of bone removal and bone quality in the context of augmented glenoid components. The bone strain field was also compared when different augmented glenoid components underwent simulated joint loading using finite element analysis.

Asymmetrically eroded glenoids were found to have denser bone ($p<0.001$) and fewer voids ($p<0.05$) in the posteroinferior quadrant, while symmetrically eroded glenoids were found to have a uniform density distribution. Asymmetric glenoid erosion was found to be oriented $28 \pm 11°$ from the superoinferior axis toward the posterior region, which resulted in increased bone removal when placing various augmented glenoid component designs. No correlation was found between the bone strain field and bone density under joint loading of augmented glenoid components using finite element analysis.

Keywords

Glenoid morphology; type B2; osteoarthritis; glenoid implant fixation; posterior glenoid erosion; biconcavity; finite element analysis; bone density

Co-Authorship Statement

Chapter 1: Nikolas Knowles – sole author

Chapter 2: Nikolas Knowles – study design, data collection, statistical analysis, wrote manuscript

Louis Ferreira – study design, reviewed manuscript

George Athwal – study design, patient selection, reviewed manuscript

Jay Keener – patient selection, reviewed manuscript

Chapter 3: Nikolas Knowles – study design, data collection, statistical analysis, wrote manuscript

Louis Ferreira – study design, reviewed manuscript

George Athwal – study design, patient selection, reviewed manuscript

Jay Keener – patient selection, reviewed manuscript

Chapter 4: Nikolas Knowles – study design, data collection, statistical analysis, wrote manuscript

Louis Ferreira – study design, reviewed manuscript

George Athwal – study design, patient selection, reviewed manuscript

Chapter 5: Nikolas Knowles – study design, data collection, statistical analysis, wrote manuscript

Daniel Langohr – study design

Louis Ferreira – study design, reviewed manuscript

Chapter 6: Nikolas Knowles – sole author

Acknowledgements

I would first like to thank my supervisor, Dr. Louis Ferreira. If not for your insight and guidance throughout my research and training, this thesis would not be possible. From your patience to my numerous questions (even on weekends), and the technical expertise you possess, it is with your guidance that these studies have been successful. I look forward to continuing my research and training with you at the Doctorate level, and am honored to be your first Doctoral student. Dr. George Athwal, your clinical expertise and your passion for research has been inspiring. Your attention to detail and ensuring each aspect of every study has direct clinical relevance has had a tremendous impact on the success these studies. Two years ago, I knew little of shoulder research required to improve clinical practice, and component designs. It is truly an area of research with a small, but dedicated community that I am proud to be part of.

To the students and volunteers of the HULC labs, it has been a pleasure to work with all of you and this thesis would not have been possible if not for the hard (and often repetitive) work of our co-op students. I am truly grateful for your time and commitment to my research. To Dan, I am truly grateful for your guidance and knowledge of the finite element method and your assistance with this chapter. Your assistance improved my knowledge of this method more quickly than I could have imagined. Your ambition to study details and increasing knowledge of the shoulder is inspiring.

To my parents, if not for your love, support and guidance throughout the years, none of this would have been possible. Your positive attitudes and guidance, while allowing me to make my own decisions has allowed me to realize my potential and ability. To Kris and Monika (and the little guys) – you have always been a constant pillar of support in my life. If not for the two of you being Engineers, it is probably a career path that I would have never considered. For everything, I thank you.

Finally, to my wonderful wife, Melanie. Your love and support throughout this process has been the most important factor in my success. If not for our summer living together, I would have never worked in this lab or considered graduate studies. Your dedication to quality research and knowledge (especially statistically) helped me grow as a researcher tremendously. Your patience and guidance throughout this process made it all possible. I love you.

Table of Contents

List of Tables

List of Figures

List of Equations

List of Appendices

CHAPTER 1 - INTRODUCTION

OVERVIEW: *Deficiency of the shoulder joint as a result of osteoarthritis often results in altered joint morphology. This may include bone density changes or bony erosions that compromise the stability of components used in joint replacement surgeries. This chapter will briefly describe the anatomy of the shoulder, as well as relevant effects from disease, and current surgical treatments involving joint replacement with implant components. In addition, current methods of quantifying bone mineral density in-vivo will be introduced in the context of bone strength and mechanical stability, as related to this thesis. Medical terminology for the unfamiliar reader is provided in Appendix A.*

1.1 BONE AND ARTICULAR CARTILAGE

Bone is a connective tissue made up of a heterogeneous and complex system of marrow, blood vessels and nerves that supply blood and store nutrients in the body.[18] Aside from its role in providing homeostasis to the body's vascular system, bone also provides structure and support, while protecting the body's internal organs. At the cellular level, bone adaptively reacts to mechanical stimuli in a process known as bone remodeling.[76] This relationship was first introduced by Julius Wolff in 1892,[74] and has since been termed Wolff's law. Wolff observed that bone's structure is a function of the applied load, such that bone is formed to resist mechanical stimuli, thereby increasing in density and strength in areas of high mechanical stresses and strain, and lower density in areas of low stresses and strain. As such, bone resorption can also occur in areas that experience drastic decreases in mechanical stimuli. Bone adaptation to applied load is analogous to the common engineering practice of component design, known as 'shape factor.'[2] Similar to creating components that resist the applied loads or moments, bone adaptively remodels to the most efficient shape (shape factor) in order to effectively distribute load.

Bone remodeling is not only important to allow bones to naturally respond to varying mechanical stimuli, but is also essential to allow bone to heal and self-repair following injury or disease. Unfortunately, in many skeletal diseases bone remodeling occurs at an undesired rate or in an unnatural manner, resulting in uncontrolled bone formation that may cause pain and loss of joint function. One aim of this thesis is to study adaptive changes in bone as the result of injury or disease in order to address clinically relevant joint morphological changes that may compromise the mechanical stability of joint replacements. The structural properties of bone are provided in section 1.1.3.

Bones are interconnected and move through an extensive combination of muscles, tendons, and ligaments, which act together with the body's nervous system to provide motion. At joints formed by the connection of two bones, articular (hyaline) cartilage forms a low-friction load-bearing surface. Cartilage is a dense connective tissue found in synovial joints, and aside from providing low-friction contact between bones, also provides shock absorption. The large water content of the dense matrix is responsible for most of the shock absorption properties; however, this dense matrix is avascular (lacking blood supply), limiting its ability to self-repair, which leads to pain and loss of joint function in pathological joints. Pain ensues as cartilage (and eventually bone) begins to wear. This wear can be caused by unknown biological factors, or altered kinematics and joint loads following deficiency or injury to the bones, muscles, ligaments or tendons.

1.1.1 Articular Cartilage Composition and Structure

The dense matrix of articular cartilage is composed of approximately 1-5% chondrocytes, 65-80% water, 10-20% collagen and 4-7% proteoglycans. Chondrocytes are the functional cells within cartilage, while proteoglycans are structural proteins.[60]

Loosely arranged collagen fibers restrain proteoglycan movement within the matrix and provide resistance to tensile and shear forces.[60] Collagen fiber orientation differs by region within the cartilage matrix to provide support with varying stress distributions. On the superficial surface, the fibers are aligned parallel to the surface, randomly oriented in the middle zone, and perpendicular to the superficial surface in the deep zone where fibers are adjacent to the calcified or subchondral bone surface.

1.1.2 Cortical and Cancellous Bone

Bone can be broken down into two main structural organizations: cortical and cancellous bone (Figure 1.1). The outer 'shell' of cortical bone (or compact bone) acts to provide structure and protection to the vast network within the bone. Cancellous bone (also known as trabecular or spongy bone) lies adjacent to the cortical shell and has a porous structure which acts to absorb shock during loading.[10] The internal structure of “plates and columns” known as trabeculae, form the porous network with varying porosity and apparent density (mass of mineralized tissue per total volume).[10,22] Characterization of the two types of bone is based on the porosity of the mineralized structure. Cortical bone has approximately 5 to 30 percent porosity and cancellous bone has 30 to 90 percent porosity;[10] however, the specific amount of mineralization to classify each type of bone is unclear. More information on bone density measurements used in this thesis is provided in section 1.1.4.

1.1.3 Bone Biomechanical Properties

The biomechanical properties of bone are dictated by its micro-architecture. For cortical bone, this internal structure results in anisotropic material properties, with generally greater strength and stiffness in the longitudinal direction of long bone.[18] This structural organization, along with its viscoelastic behaviour makes bone stronger in compression than in tension. Similar to engineering materials, cortical bone exhibits a

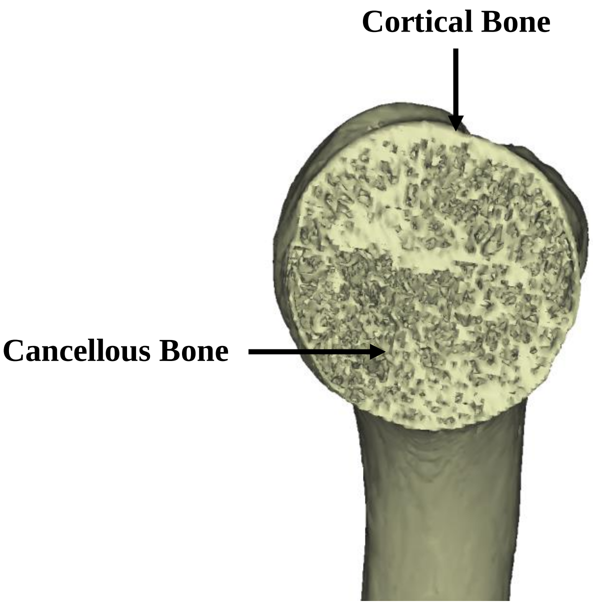

Figure 1.1: Cortical and cancellous structural organization within an excised humeral head

near linear stress-strain curve, aside from a slight toe-region at low strain. This yields an assumed uniform and unique Young's modulus in each loading direction (Figure 1.2).[49]

Similarly, cancellous bone exhibits anisotropic and viscoelastic behavior, but the apparent mechanical properties are highly variable, a function of apparent density, and consequently change with anatomic location.[18] Additionally, cancellous stress-strain relationships show a varying profile, in which the bone first exhibits a linear response, followed by plastic collapse, in which the stress remains relatively constant for increasing strain, before exhibiting a second linear response and fracture (Figure 1.2). This region of constant stress occurs due to the porous trabeculae (internal porous structure of the bone) failing before compromising the entire structure. It is this varying density distribution that undergoes constant remodeling allowing bone to adaptively react to variations in loading that may result from changes in muscle strength, injury, or disease.

Bone structure is also a function of diet, age, lifestyle and activity level. Therefore, cross-population material property characteristics are difficult to obtain.

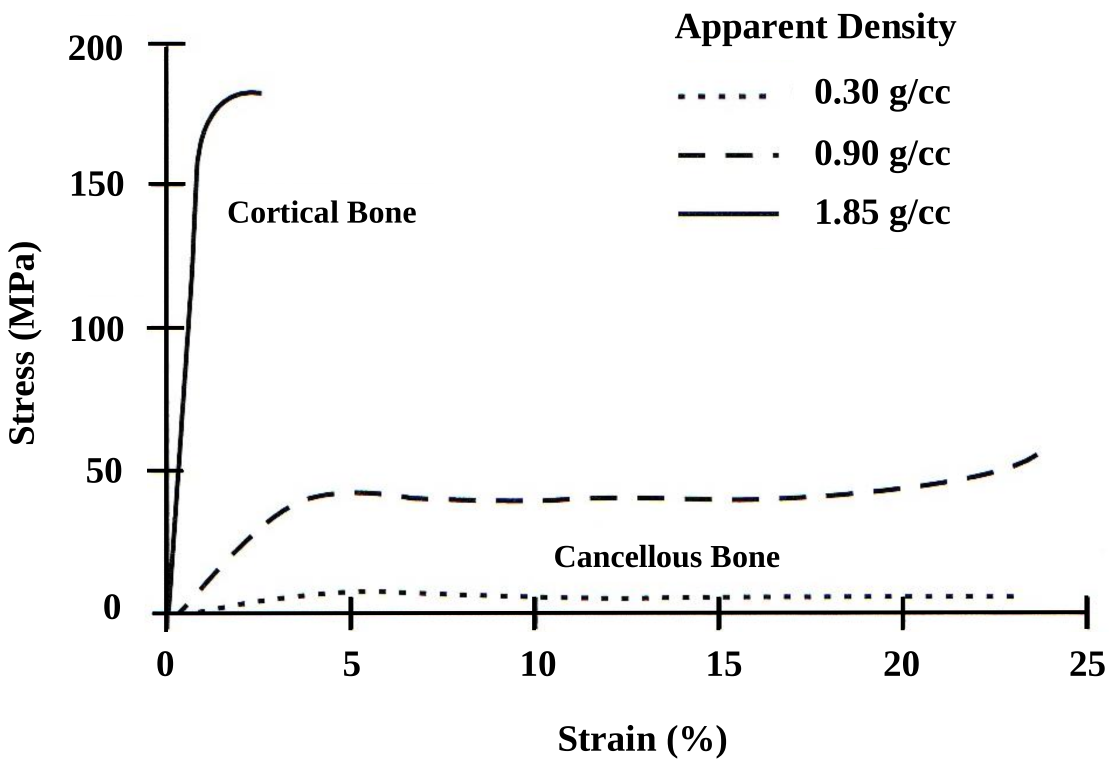

Figure 1.2: Stress-strain curves for bone as a function of apparent density.[49]

Additionally, as previously discussed, cancellous bone properties are a function of anatomic location and loading, resulting in difficulty in the development of equations that accurately represent material properties. Carter and Hayes[10] first suggested a commonly accepted relationship between the apparent density of cancellous bone and Young's modulus that was strain rate dependent; however, it has since been suggested that strain rate dependency is negligible, and therefore, the modulus can be assumed independent of strain rate.[73]

Current finite element studies of the shoulder make use of a wide range of strain rate independent modulus equations.[8,13,26,27,34,65,75] A validated modulus equation for the shoulder does not exist, and as a result, these equations may not accurately represent the narrow range of bone densities found in the glenoid or variations due to osteoarthritis. As part of this thesis the modulus equation developed by Carter and Hayes[10] (Equation 1.1), which is sensitive to slight changes in cancellous apparent density in the low density range,[4] was chosen. Cortical bone exhibits a near linear modulus, with an average apparent density $\geq$1.85g/cc, allowing for an assumed homogeneous modulus (E= 20 000 MPa).[4]

$$\boldsymbol{E = 2875 \cdot \rho_{app}{}^{3} \quad [\mathrm{MPa}]} \qquad \text{Equation 1.1}$$

1.1.4 *In-Vivo* Bone Density Measurements

Measurement of bone mineral density (BMD) in living patients is important in order to determine fracture risk or assess the quality of bone, especially following fracture, injury or disease. Advancements in medical imaging technologies have increased the accuracy in quantifying bone density in a variety of anatomical locations and have allowed for these assessments to be performed *in-vivo,* with little to no patient risk. Specific technologies are discussed below.

1.1.4.1 Dual energy x-ray absorptiometry (DEXA)

Dual energy x-ray absorptiometry (DEXA) is the most common quantitative method to measure BMD and diagnose osteoporosis. This technology uses low dose x-ray radiation to measure an 'areal' or area density in g/cm^2.[45] This method allows for the determination of fracture risk in many patients; however, the areal measurement is a sum of both the cancellous and cortical bone in a region, which present some difficulty in analysis.[25,45] Due to this reality, it is possible that large patients with low BMD and small patients with high BMD have similar results when scanned with a DEXA scanner, due to the contribution of soft tissues in the areal density measurements. This method must be done at the discretion of an experienced clinician/technician, and the results interpreted subjectively.

In many research applications, a higher resolution, with greater distinction between cortical and cancellous bone is necessary. In these cases, DEXA fails to provide the required quantitative results and is best used as a clinical tool or in studies assessing fracture risk that are not sensitive to variations that may occur due to the areal BMD measurements.

1.1.4.2 Computed Tomography Hounsfield Units

Computed tomography scanners are used as a diagnostic and increasingly common research tool to assess the internal structure of patients or subjects. The process works by collecting a stack of x-ray projections around a patient/subject and calculating the attenuation of internal tissues. Computer algorithms are used to align the images and assign intensity values based on the x-ray attenuation, saving the images in a common DICOM (digital imaging and communications in medicine) format. Modern multi-slice CT scanners are calibrated using the Hounsfield scale, which averages the x-ray attenuation using the known linear attenuations of water and air (Equation 1.2). This radiodensity is then mapped as grayscale intensities (Hounsfield Units – HU) to each pixel in a series of two-dimensional images (typical clinical resolution is 512x512 pixels), in the anatomical sagittal, coronal, and axial planes. The resultant intensity values represent different tissues and are scaled based on the supplied cathode energy. The range of HU values are from -1024 to +3071 with approximate values of water and air of 0 and -1000 HU, respectively.

$$HU = \frac{\mu - \mu_{water}}{\mu_{water} - \mu_{air}} \, x \, 1000 \qquad \text{Equation 1.2}$$

Since the slice increment and thickness of each image is known, software algorithms can determine voxel intensities (three-dimensional pixels). By thresholding the intensity value of each voxel, using manual segmentation methods and spatial information provided, materials can be separated from the CT scan data. This information allows for the reconstruction of bone into three-dimensional computer models with accuracy as good as a patient's physical bone.[7] The resolution of clinical CT scanners is limited in order to balance radiation dose with requirements for accurate diagnosis. In many modern research applications, micro-CT scanners capable of increases in resolution of 10-100 times greater than clinical CT scanners, are required. As part of this thesis, clinical CT scans were found to be sufficient, and were used to be consistent with the diagnostic tools currently available to clinicians in a modern hospital setting.

1.2 THE GLENOHUMERAL JOINT

1.2.1 Osseous Anatomy

The glenohumeral joint (GHJ) is comprised of two bones: the humerus, and scapula (Figure 1.3). The humerus allows for three-axis rotations of the arm about the GHJ, with the proximal humeral head articulating within the glenoid fossa, or glenoid. The native glenoid has a shallow depth and curvature that differs from the curvature of the humeral head, producing a non-constrained joint.[37] Both articular surfaces are covered in articular cartilage, which decreases friction and increases load distribution,

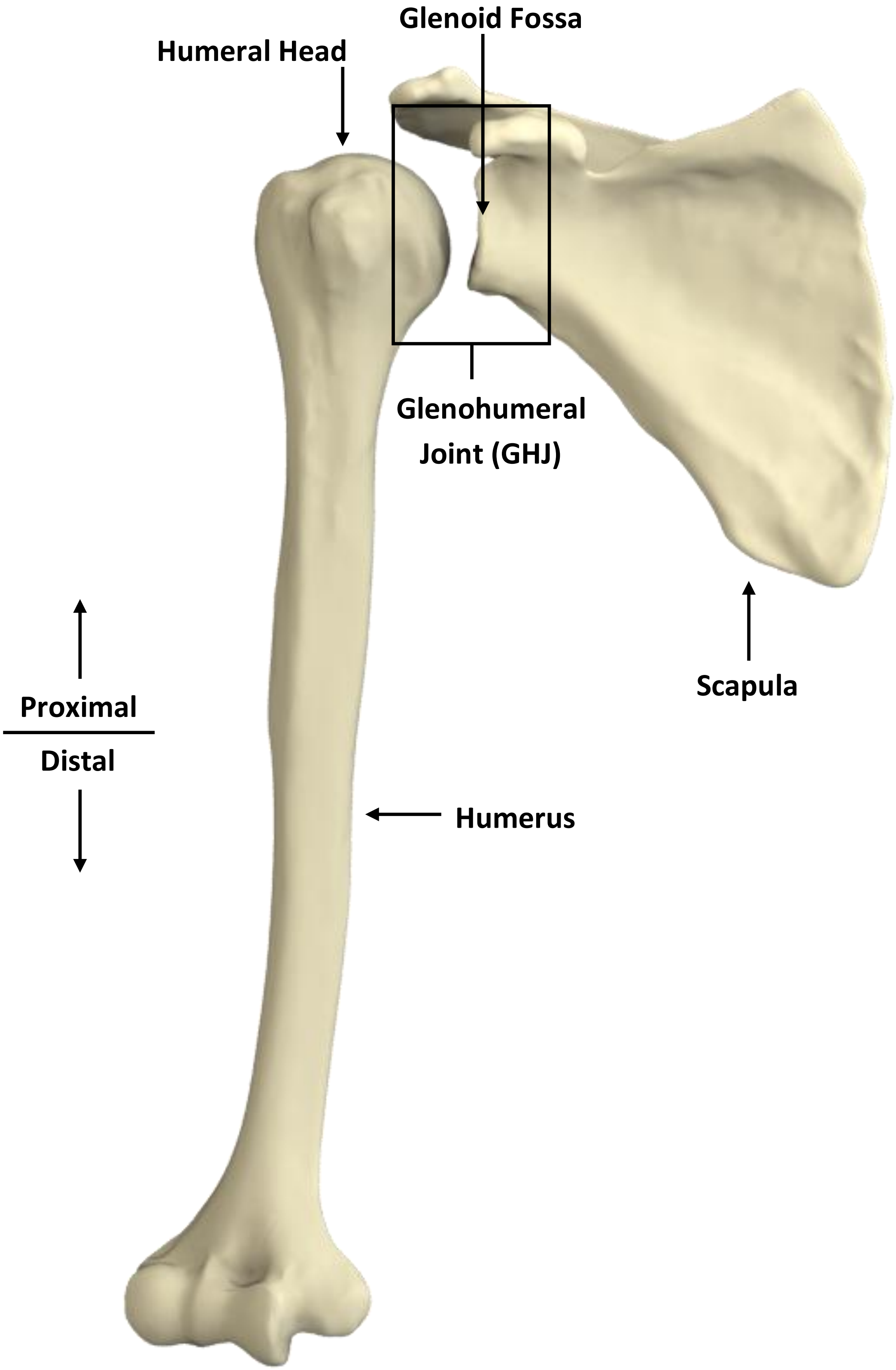

Figure 1.3: Three-dimensional reconstructions of the humerus and scapula

due to its lower modulus than the underlying bone. This difference in curvature results in a localized contact area of the humeral head on the glenoid, and allows for the large and nearly impingement free range of motion of the GHJ. Theoretically, this may also allow relative translation of the humeral head across the glenoid, which could compromise joint stability.[5,6,40] With sufficient soft tissue balance across the GHJ, it has been shown that stability is maintained and relative humeral translations are minimized.[28,35,51,66] However, pathologic soft tissue deficiency in the GHJ may result in increased translation, or subluxation of the humeral head, leading to cartilage degradation and bony erosion.[23,67,68] Furthermore, this subluxation may alter the joint contact area, with resultant loading changes and possible bone remodeling. Pathologic joint deficiency will be further discussed in section 1.3.

1.2.2 Glenoid Anatomic Parameters

Anatomic parameters on the scapular articulation of the glenohumeral joint, the glenoid, allow for characterization of the articulation. These parameters assist in the assessment of joint pathology, morphology and may assist in the selection of devices required for joint replacement surgeries. Additionally, these parameters are essential in the design of glenoid components that act to restore and mimic native joint anatomy. The three parameters discussed here include the glenoid height, the glenoid width, and the glenoid version (Figure 1.4).

Glenoid height is measured as the most superior to inferior points on the glenoid surface in a plane sagittal to the glenoid articular surface (Figure 1.4-A).[37] Due to the inherent ‘pear shape’ of the glenoid, two width measurements are typically reported – a superior width and an inferior width. These two measurements are measured as a perpendicular bisector of the superior-inferior axis of the glenoid, from the most anterior to posterior edges of the glenoid surface (Figure 1.4-B). Finally, glenoid version, which is arguably one of the most important factors related to glenoid stability, is measured as the angle of a perpendicular line/plane to the axis of the scapula (or scapular coronal axis)

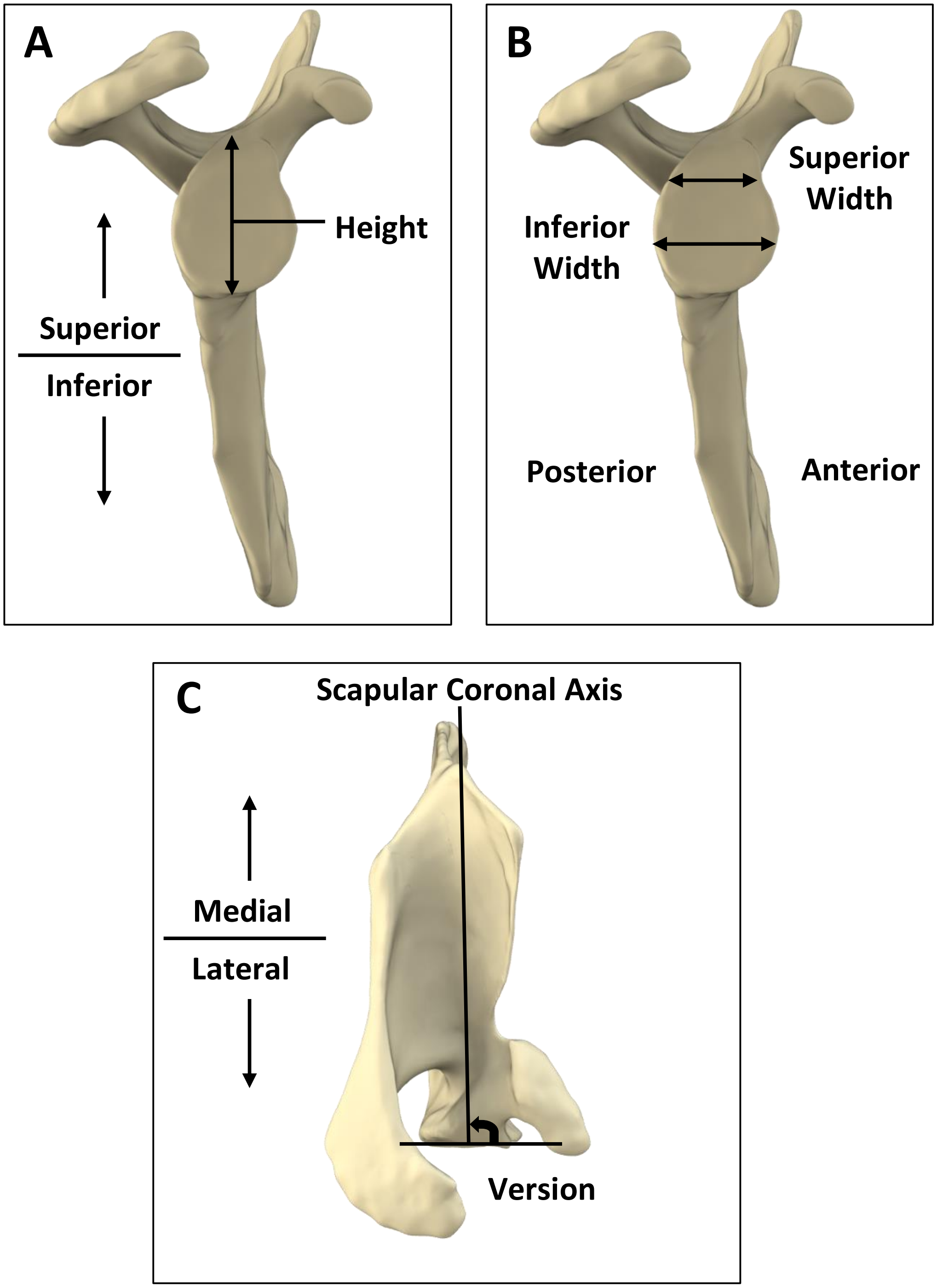

Figure 1.4: Anatomic Parameters of the Glenoid

The glenoid height is measured as the most superior to inferior points on the glenoid surface **(A)**. The glenoid width is measured as the most anterior to posterior points, superiorly and inferiorly **(B)**. The glenoid version is the angle of the glenoid relative to the line/plane perpendicular to the scapular coronal axis **(C)**, and is positive in a counter-clockwise direction.

(Figure 1.4-C).[21,38] This measurement is referred to as anteversion if the angle is positive in the counter-clockwise direction, and retroversion if negative. Recent studies have suggested that within the population, the glenoid in natively retroverted 1 ± 3°, which increases the difficulty in restoring native anatomy in shoulder replacement procedures, by contributing to joint instability.[44]

1.3 Glenohumeral Joint Deficiency/Pathology

Glenohumeral joint (GHJ) deficiency as related to this thesis focuses primarily on glenohumeral osteoarthritis (OA). Primary OA is idiopathic, while secondary OA may be caused by injury, disease, genetics or many other factors. Osteoarthritis is non-systemic and is characterized by joint inflammation with associated pain. As OA progresses, bony growth occurs, known as osteophytes, which limit joint motion and result in pain. Similarly, the loss of motion of the joint often results in the calcification of associated ligaments and tendons due to lack of use. Bony growths and calcification occurs due to uncontrolled bone remodeling brought on by altered loading patterns, as well as unknown biological factors.

Typically uncharacteristic of OA, bony erosions occur on the glenoid as articular cartilage degrades. This erosion can occur uniformly across the glenoid surface, producing a symmetric erosion pattern, or may occur asymmetrically, due to subluxation of the humeral head.[23,67,68] It is unknown as to whether subluxation leads to the progression of OA or if OA leads to subluxation; however, in either case the stability of the joint is often severely compromised. Walch et al.[68] classified glenoid bony erosion into three main classifications (Figure 1.5). Symmetrical glenoid erosion is classified as type A, and sub-classified as A1 – minor and A2 – major. Asymmetric erosion is classified as type B, and sub-classified as B1– narrowed posterior joint space with no signs of glenoid posterior erosion and B2 – posterior glenoid erosion with a visible articular biconcavity. Type C classifies a dysplastic (genetic disorder) glenoid with retroversion >25°. These classifications form the basis for clinicians to determine the

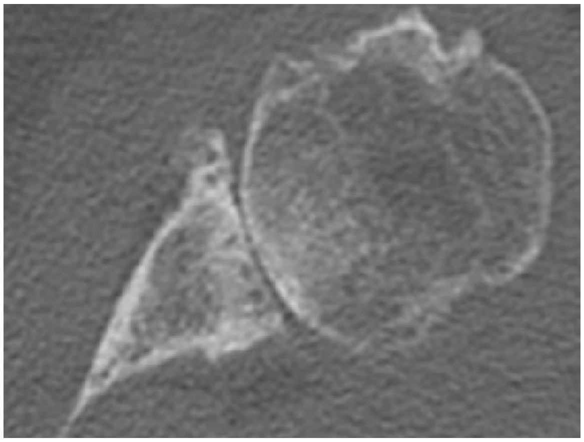

Type A1

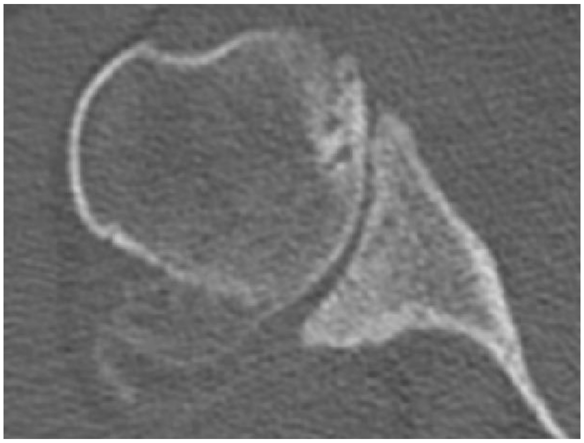

Type A2

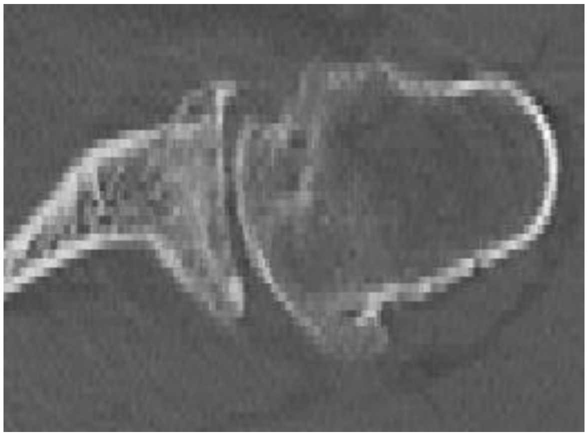

Type B1

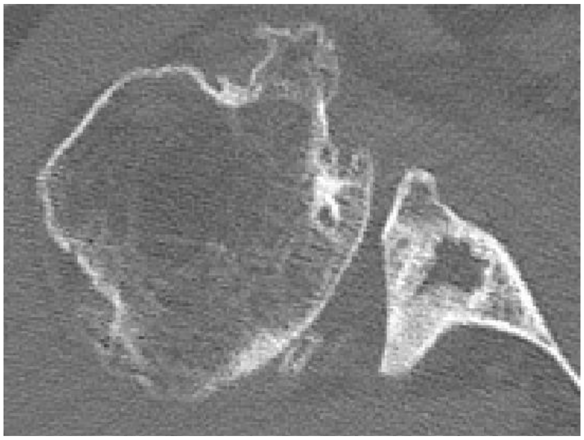

Type B2

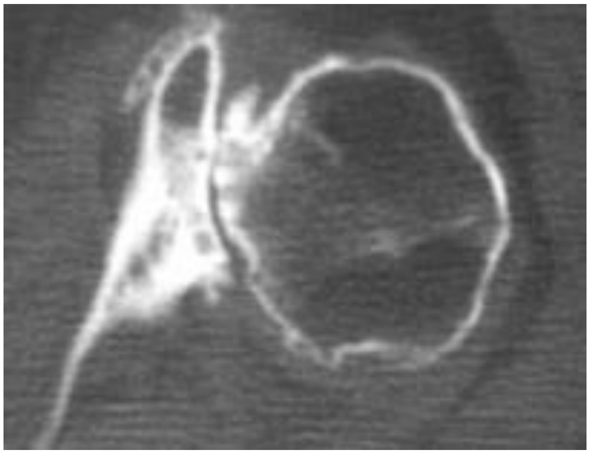

Type C

Figure 1.5: Axial radiographs of five glenoid erosion morphologies classified by Walch et al.[68]

progression of OA and allow for the selection of joint replacements that act to restore native joint anatomy.

1.3.1 Surgical Interventions for GHJ Deficiency

Joint replacement surgeries are performed when joint pain and loss of function has reached a level that cannot be improved with non-surgical treatments. Specific to each individual patient, a variety of surgical options exist to improve joint function and reduce pain. Depending on the condition of soft tissues, progression of OA, age, health, etc., surgical outcomes are highly variable.[16,20,36,57] In all surgical cases, preservation of bone stock is essential for implant fixation and stability and to ensure that sufficient bone remains in case of future need for revision surgeries.[69,71]

1.3.1.1 Anatomic total shoulder arthroplasty

Anatomic total shoulder arthroplasty (TSA) replaces both the proximal humerus and the glenoid with artificial components that act to mimic native anatomy. In preparation for the glenoid component, the glenoid is reamed to a uniform curvature that matches that of a standard glenoid component, fixation holes are drilled, and the glenoid component is cemented in place (Figure 1.6). In preparation for the humeral component, the humeral head is excised (Figure 1.7), the central bone canal reamed and a humeral component is pressed or cemented in place. The humeral component is typically manufactured of high-strength bio-compatible cobalt-chromium (CoCr), while glenoid components are typically manufactured of ultra-high molecular weight polyethylene (UHMWPE). Glenoid components may also consist of a metal backing with a polyethylene insert to promote bone in-growth, provide a stiffer bearing surface, and allow for screw fixation in cases of post-traumatic reconstruction.

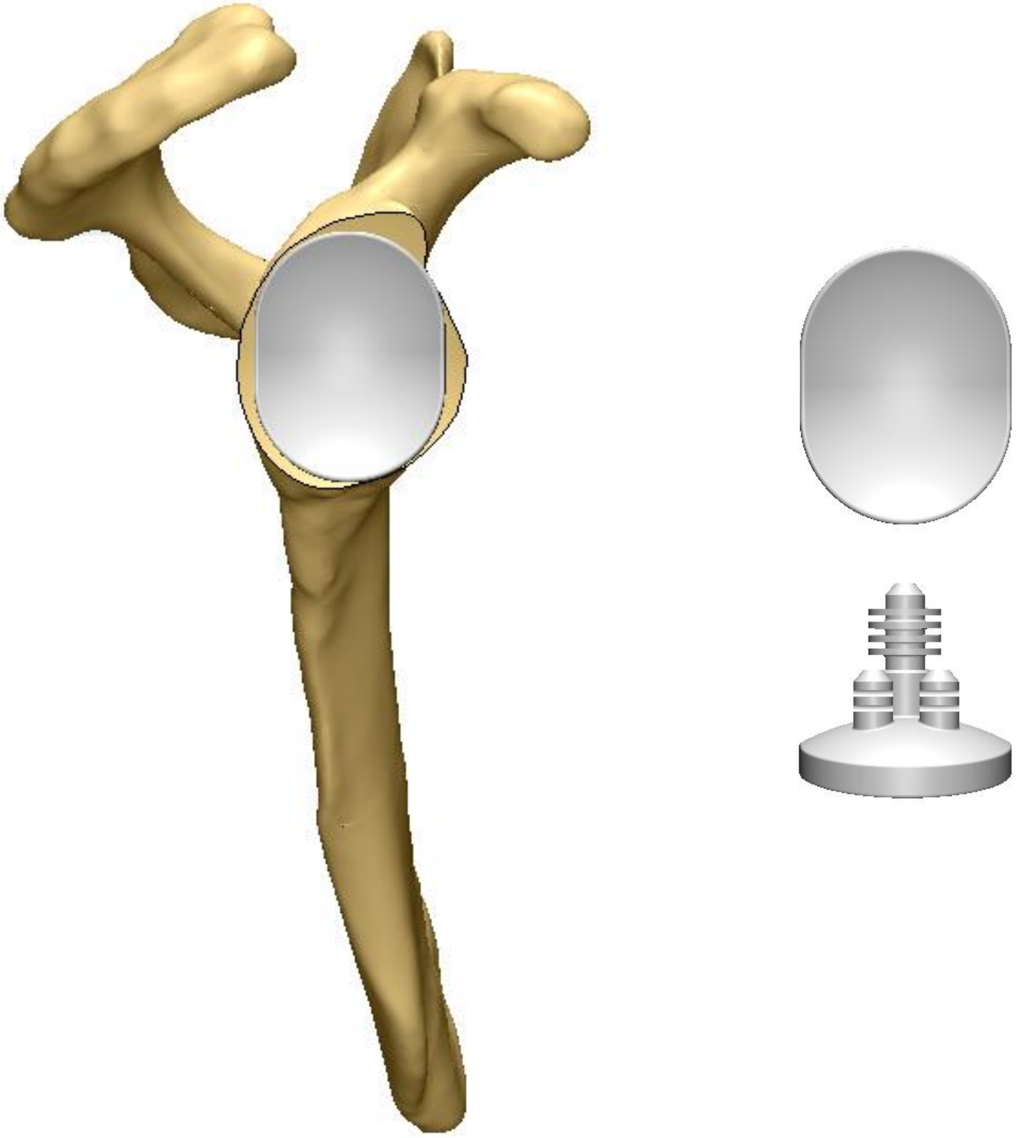

Figure1.6: Depuy® Global® APG+ standard glenoid component

An implanted standard glenoid component (left) and articular surface and posterior view of the Depuy® Global® APG+ standard glenoid component (right). Note the articular and backside surfaces have a uniform curvature.

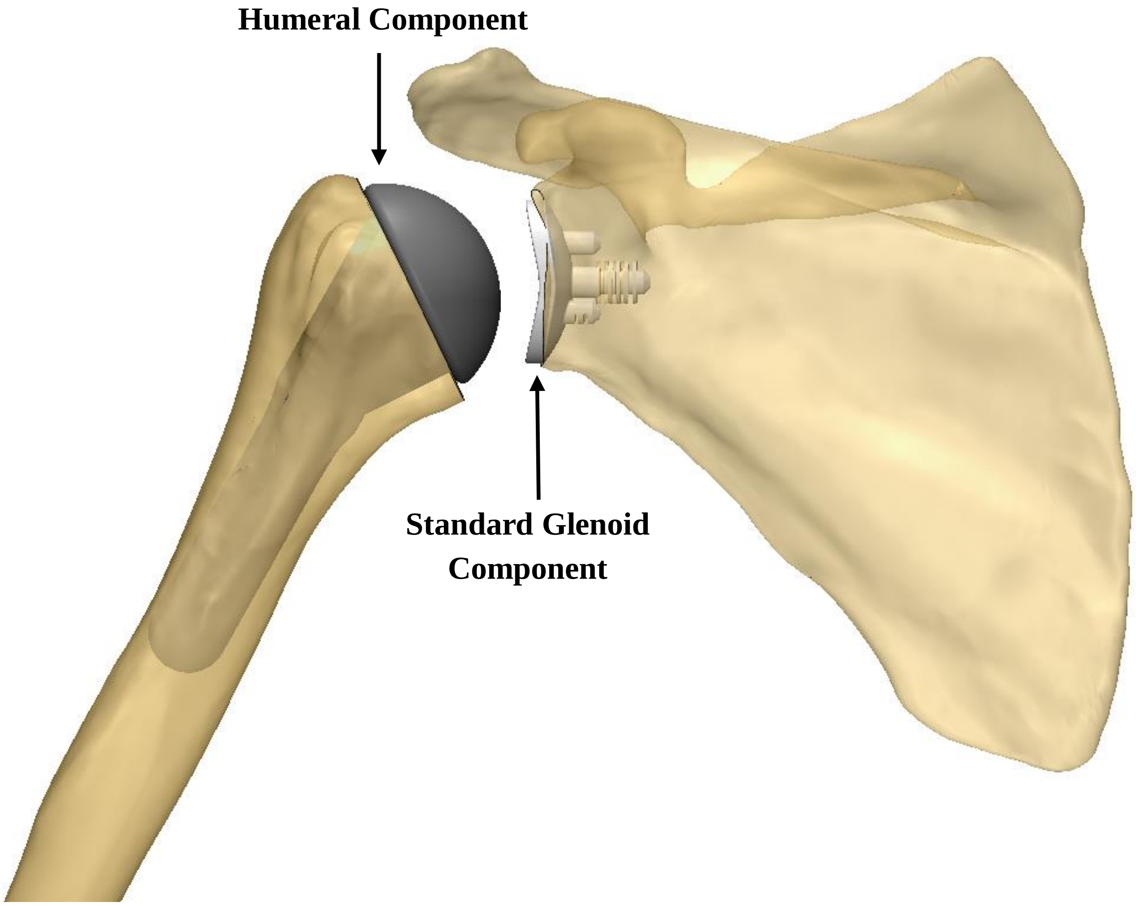

Figure1.7: Implanted components in anatomic total shoulder arthroplasty

The humeral component and glenoid components are sized to patient anatomy and cemented or press fit in the reamed bone surfaces.

In more advanced cases of osteoarthritis, such as those with posterior bone loss, the surgical intervention may require a bone graft to be placed between the implant and eroded glenoid to reconstruct the native joints articular geometry. Similar to this method, augmented glenoid components are commercially available that use a step or wedge on the medial surface of the implant to "fill" the region of eroded bone. These methods are typically used when acquired retroversion of the glenoid is greater than 15°, as this morphology cannot be corrected with asymmetric reaming alone.[12]

1.3.1.1.1 Augmented glenoid components

Augmented glenoid components are a modified version of anatomic total shoulder arthroplasty glenoid components, designed specifically to minimize bone removal in shoulders with posterior glenoid erosion. The term ‘augmented’ refers to an extension or thickening of the posterior aspect of the implant back. This thickening is designed to build up the asymmetrically eroded posterior region in order to restore the native orientation of the articulation. These implants correct to the desired version angle without the requirement for asymmetric or eccentric 'high-side' reaming of the deficient glenoid.

There are currently two implant manufacturers producing augmented glenoid components for clinical use, and one manufacturer marketing an augmented component for imminent availability. All three implants orient the augment about the central axis of the implant. This design assumes posterior bone loss occurs with a maximum directed toward the 9 o’clock position in a right shoulder. If bone loss does not occur in this manner, there may be additional bone removal required in the superior aspect of the glenoid in order to facilitate implantation (Figure 1.8). Furthermore, if bone loss progresses anterior past the superoinferior axis in the inferior aspect of the glenoid, there may not be bone remaining for proper implant support. This may result in malrotated implant placement or additional bone reaming in order to accommodate the implant design.

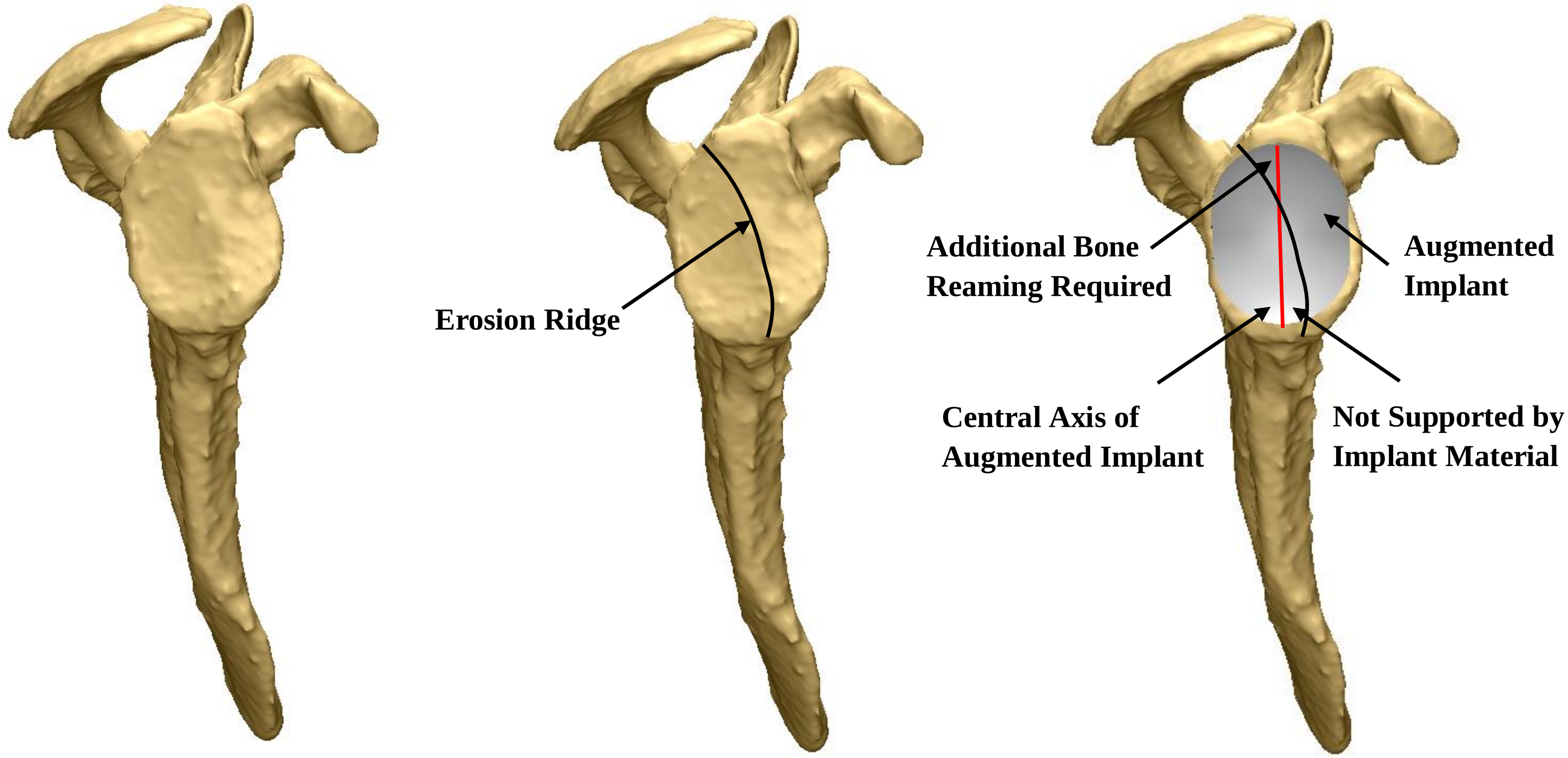

Figure 1.8: Three-dimensional reconstructions of a patient scapula with posterior glenoid erosion

Intact scapula (left). Depiction of the erosion ridge (middle). Implanted augmented glenoid component illustrating regions requiring additional bone removal and unsupported by implant material (right).

1.3.3.1.1.1 DePuy® Global® Steptech® APG

The Global® Steptech® Anchor Peg Glenoid (APG) is a variation of the standard Global® APG+ Implant System (Figure 1.5). The Steptech® uses a 3, 5 or 7 mm step from the implants backside encompassing the entire posterior hemisphere (Figure 1.9). For each step height, the implants are available in five sizes according to bearing diameters of 40, 44, 48, 52 and 56 mm. These implants are sized according to the glenoid size and humeral component required for each individual patient. This implant reduces joint medialization by minimizing eccentric 'high-side,' anterior reaming. The stepped design mimics the articular backside geometry of commonly used all-polyethylene non-augmented implants, reducing the contribution of shear forces experienced by the cemented fixation pegs. According to Depuy, the Global® Steptech® APG reduces the need for bone grafts, asymmetric (eccentric) reaming, thereby reducing joint medialization and removal of healthy bone.[17]

1.3.3.1.1.2 Exactech® Equinoxe® Posterior Augment Glenoid

The Equinoxe® Posterior Augment Glenoid acts to reduce anterior cortical bone removal for posterior eroded glenoids with retroversion greater than six degrees.[19] The implant is anatomically 'pear' shaped with a smaller superior diameter and larger inferior diameter (Figure 1.9). This implant uses a full-wedge design with an 8° wedge angle from posterior to anterior. Although not currently marketed, the company has also recently tested models with 12° and 16° wedge angles.[54] The implants are available in small, medium, large, and extra-large sizes that act to maximize glenoid surface area, while reducing the risk of implant overhang. Exactech also markets metal-backed augmented implants (10° superior augment, and 8° posterior augment) for use in specific morphological cases.

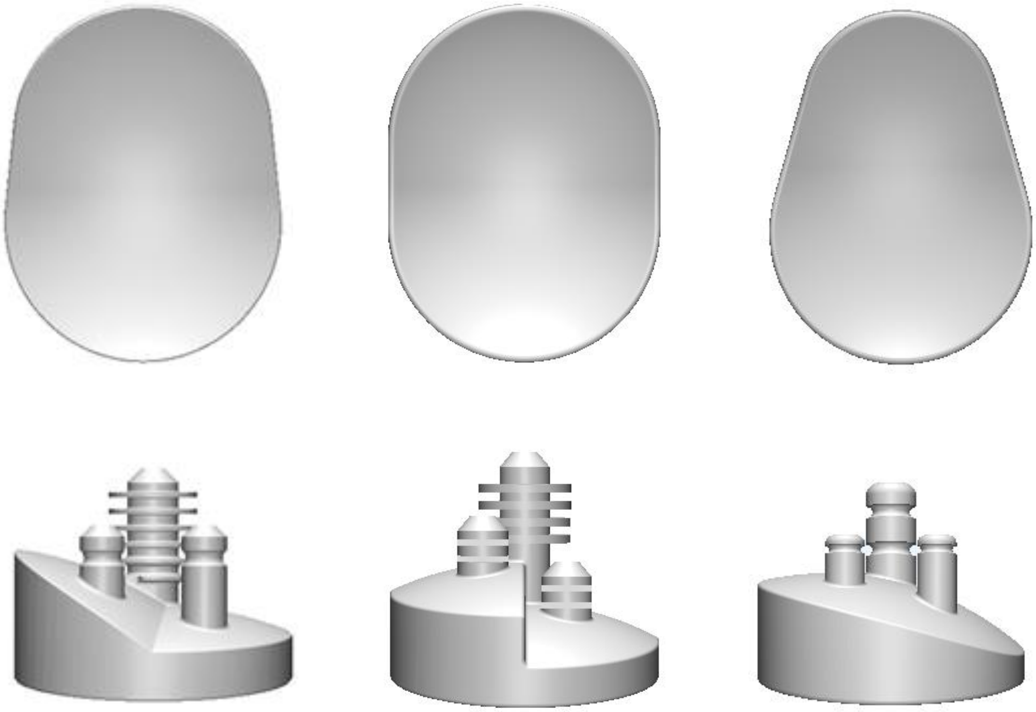

Figure 1.9: Three commercially available augmented glenoid component designs

The Tornier® Posterior Augment Glenoid (left), DePuy® Global® Steptech® APG (middle) and Exactech® Equinoxe® Posterior Augment Glenoid (right). Bottom figures are posterior views and top figures are articular surface views.

1.3.3.1.1.3 Tornier® Posterior Augment Glenoid

The Posterior Augment Glenoid (PAG) is the newest augmented glenoid implant and is expected to be commercially available in 2015. The PAG can be thought of as a hybrid of the Steptech® and Equinoxe® PAG as it uses a wedge symmetric about the implants central axis that encompasses the entire posterior hemisphere (Figure 1.9). This implant has wedge angles of 15°, 25° and 35° and is available in small, medium, large and extra-large sizes. The design acts to minimize reaming by better mimicking the degree of retroversion exhibited in asymmetric glenoid erosion.

1.3.1.2 Reverse Total Shoulder Arthroplasty

Reverse total shoulder arthroplasty (RTSA) is an effective treatment for rotator cuff arthropathy or in cases that cannot be effectively managed with anatomic total shoulder arthroplasty.[59] The alteration of the native muscle balance across the glenohumeral joint (GHJ), as seen in many pathologic GHJ diseases, contributes to the inherent instability of glenoid posterior erosion. [59] As a result RTSA is an attractive treatment option in many of these multifactor cases. Similarly, RTSA is most commonly used in revision surgery due to the lack of sufficient glenoid bone stock remaining for effective implant fixation and support. It may also be used in cases of trauma when significant disruption to soft tissues or bone support has occurred.

In the RTSA procedure, the native anatomy of the joint is altered by implanting a glenosphere on the scapular articulation and a humeral component with a polyethylene insert on the humeral articulation (Figure 1.10). This effectively swaps the ball and socket of the GHJ, thereby lateralizing the joint centre and increasing the moment arm, which alters the contribution of muscle loads required for arm motion. Additionally, the constrained nature of the RTSA components may assist in resisting the effect of the proximally directed resultant joint load vector, thereby increasing the stability of the joint.[59]

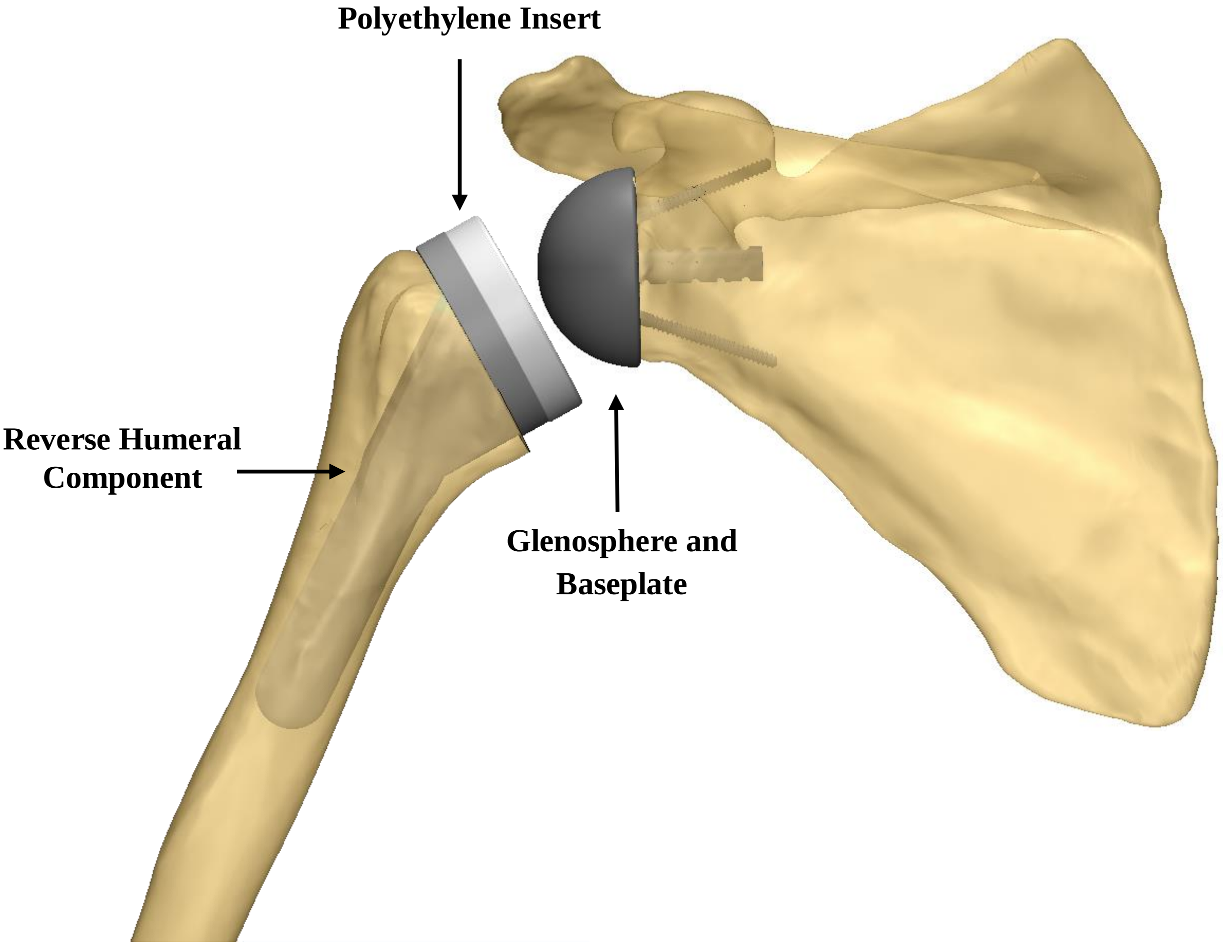

Figure 1.10: Implanted components in reverse total shoulder arthroplasty

The humeral component and glenoid components are sized to patient anatomy and cemented or press fit in the reamed bone surfaces. The reverse design alters the native anatomy by placing the ‘ball’ on the scapular articulation and the ‘socket’ on the humeral articulation. This implant system lateralizes the joint centre, thereby altering the contribution of muscle forces required for arm motion.

1.3.1.3 Hemi-Arthroplasty

Hemi-arthroplasty, also known as the ‘ream and run procedure,’ acts to minimize bone surface removal for patients requiring joint replacement. In this procedure a standard humeral head component it utilized as in the TSA procedure previously described (Section 1.3.1.1). However, on the glenoid surface only minimal reaming is performed to achieve a concentric glenoid surface.[41,42] The procedure has been shown to be effective in the treatment of glenohumeral osteoarthritis,[24,43,47] and because it does not implant a glenoid component or bone graft, it may be a more effective procedure for younger patients who may have a future need for revision surgeries.

Resurfacing hemi-arthroplasty is an even more conservative bone preservation procedure that retains the humeral head and uses a humeral component that encompasses only the articular surface of the humeral head. Again, the glenoid is minimally reamed to match the articular curvature of the humeral component, preserving the most bone.

1.4 FINITE ELEMENT MODELLING OF THE SHOULDER

In orthopaedics, advancements in imaging technologies and medical imaging software now allow for accurate reconstruction of bone geometry (primarily from computed tomography data). In computational biomechanical modeling, three-dimensional models of bone can be created, bone specific heterogeneous material properties can be defined and physiological loads can be simulated. Furthermore, using these three-dimensional models, modifications can be made to allow for the virtual implantation of medical devices. This allows us to critically evaluate the loading scenario imposed by joint replacements prior to implantation *in-vivo.*

The finite element (FE) method refines a complex continuum into discretized geometrical shapes, known as finite elements. These finite elements are related and move through connections known as nodes (Figure 1.11). Contrary to traditional continuum

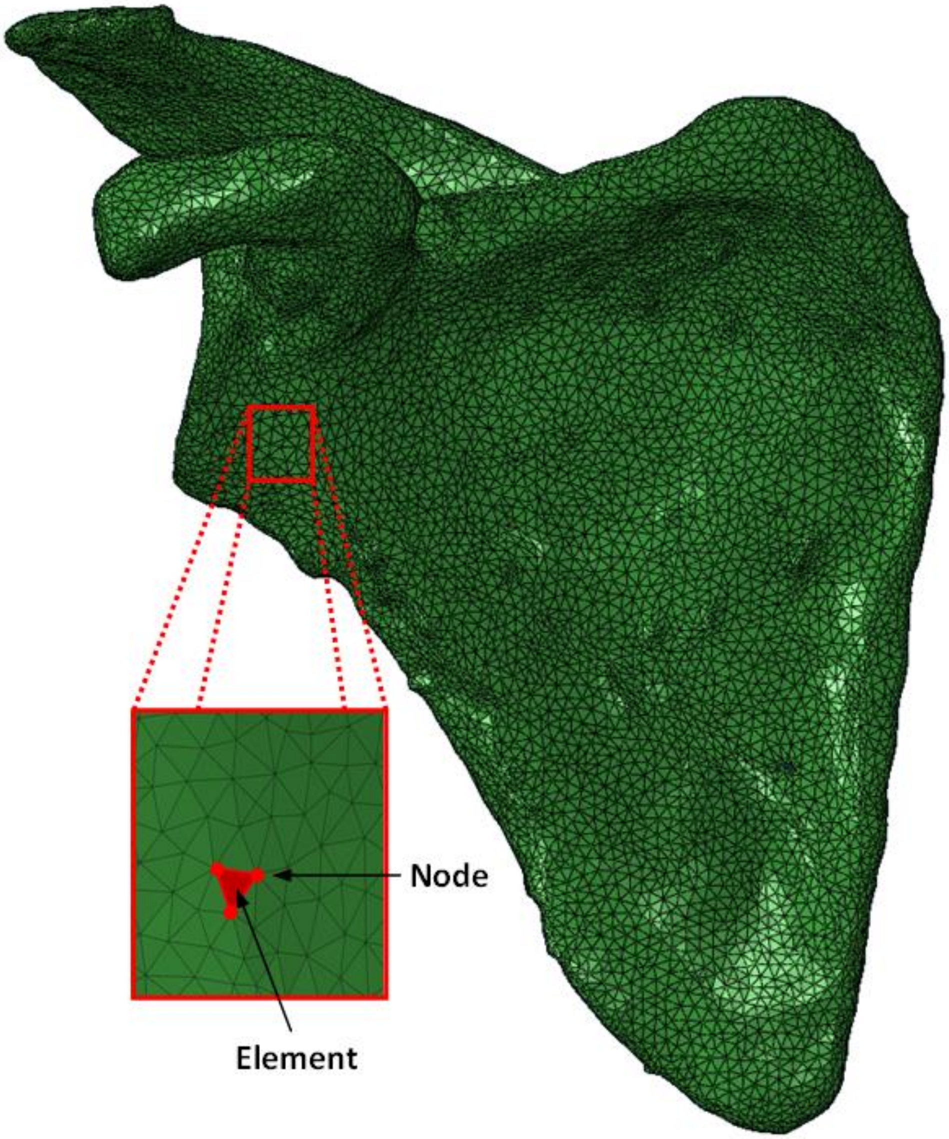

Figure 1.11: Discretized scapular model for finite element analysis

The complex geometry is broken down into a series of elements and nodes (inset) and the governing equations are applied across these regions.

mechanics that only allow for the application of material and governing equations over the geometry as a whole, the finite element method allows for individual material properties to be defined to specific elements and the governing equations to be applied in an element by element or node by node basis. This application of forces and constraints provides the user with a site specific analysis of the internal loading scenario of the discretized model.

A large number of studies have explored shoulder biomechanics using the finite element method. These range from comparatively simple studies discussing model generation,[11] stress and strain analysis [8,13,27,39,61] implant thickness,[63] humeral and glenoid component conformity,[65,75] and micromotion,[72] to seemingly complex studies that assess implant bone remodeling and in-growth,[1,9,58,62] and cement mantle stresses.[32,33,50,64] An inherent discontinuity in all previous FE models of the shoulder is that accurate and validated equations for site specific material properties do not exist. The apparent density of bone and CT intensity have been correlated[10,52,53,55] and these relationships used to develop equations that relate to mechanical properties.[3,4,29,48] However, it has been suggested that these relationships, and therefore the equations that are experimentally developed, are site-specific.[48] It has also been suggested that accurate assessment of bone density increases the accuracy of subject-specific FE models.[56] It follows that all previous shoulder FE studies have used a variation of equations developed for alternative anatomic locations, which could have a dramatic affect on the validity of FE analysis.

Although studies have begun to assess augmented glenoid components using FE methods,[31] the distribution of bone densities in osteoarthritic joints may vary greatly from the non-pathologic joint, increasing the error in using non-site-specific material mapping. A handful of studies have decreased the material properties in their simulated osteoarthritic (OA) groups by a given factor.[31,50] However, it is likely that these models do not accurately model the actual bone density in the OA joint - in particular the non-native distribution that may occur in pathologic joints. It is therefore essential to create models based on OA joints in order to critically evaluate the loading scenario imposed in a clinically relevant manner.

1.5 RATIONALE

Total shoulder arthroplasty (TSA) has been shown to be effective in pain relief for up to 93% of patients.[46] The number of TSA procedures performed in the U.S. is expected to increase by almost 40% from 2005 to 2015[14] (with similar predictions in Canada). Improving the long-term outcomes of TSA may significantly reduce future health care costs. Positive outcomes rely on surgical technique to ensure implant placement matches implant design. Pre-operative planning software and patient-specific guides now exist to assist surgeons in the optimal placement of the glenoid component, showing early success compared to traditional techniques.[30,70] Although these guides may improve implant placement, currently marketed glenoid implants show concerning long-term outcomes, primarily from implant loosening.[15] Furthermore, the complex scenario presented in asymmetrically eroded glenoids increase the risk of implant failure by compromising underlying bone support, fixation and stability. Augmented glenoid components exist to account for these complexities; however current design may not match the morphology of the joint. This may result in malaligned component placement or compromise desired component fixation.

Although first classified by Walch et al.[68] fifteen years ago, little is known about asymmetric glenoid erosion or its affect on glenoid component stability. With current advancements in medical imaging and associated software, our understanding of this joint morphology has dramatically improved in recent years. Pre-operative computed tomography scans have become a common pre-operative tool to allow surgeons to improve and optimize their surgical plan. These scans provide a vast amount of data that can be utilized to assess and classify previously unknown characteristics of pathologic joint deformity.

Computational methods now exist for us to critically evaluate the internal and external loading imposed on bone under varying parameters. This has the potential to significantly improve the long-term outcomes of joint replacement components by improving component design, fixation and positioning. With these advancements, models can be created that closely mimic the loading scenario imposed by joint replacement surgeries.

1.6 PROJECT OBJECTIVES AND HYPOTHESES

The overall goal of this thesis was to quantify the morphology of the osteoarthritic glenohumeral joint (GHJ) in order to better understand the mechanisms that compromise joint replacement fixation, stability and support. Current implant designs rely heavily on previously marketed component designs that have successfully passed regulatory approval. However, the extent to which current designs are based on research that accounts for joint deficiency and acts to reproduce native joint anatomy is unknown. These inherent flaws may compromise current joint replacements, leading to premature failure. In the pursuit of better understanding the mechanisms of GHJ replacement failure, four specific objectives were explored as part of this research. The corresponding hypotheses follow each objective.

Objective 1: To characterize the subarticular glenoid bone density in three-dimensionally reconstructed scapulae of patients with symmetric and asymmetric glenoid erosion.

In order to measure glenoid bone density a quadrant coordinate system must first be developed to ensure consistent measurement regions between patients. This will allow for regional bone density variations to be determined on the basis of Hounsfield Units (HU) in four quadrants and two depths from the articular surface. The porosity of the regions can also be compared using a volume subtraction method in the same regions. Additionally, the density and porosity in anterior and posterior regions separated by the erosion in asymmetrically eroded glenoids can be compared using the same method as the quadrants.

Hypothesis 1: It is hypothesized that due to the altered joint kinematics observed in patients with asymmetric glenoid erosion, bone density will be greater and porosity lower in the posterior aspects and specifically, the posteroinferior quadrant of asymmetrically eroded glenoids as compared to symmetrically eroded glenoids.

Objective 2: To determine the orientation, position and surface area of bone loss in patients with asymmetric glenoid erosion.

Glenoid posterior erosion results in a clearly visible ridge of eroded bone when three-dimensionally reconstructed or *in-vivo*. In order to quantify the symmetry of this erosion, a clinically relevant two-dimensional sagittal plane analysis can be utilized; making use of points collected on three-dimensional scapulae reconstructions. The collected points must be validated between observers to ensure consistency in results.

Hypothesis 2: It is hypothesized that contrary to current commercially available augmented glenoid components, erosion in asymmetrically eroded glenoids is not symmetric about the superoinferior axis of the glenoid.

Objective 3: To quantify and compare the volume of bone removed and the quality of underlying bone with three augmented glenoid component designs.

Virtual models constructed using computer aided design (CAD) software to the exact dimensions of three currently marketed glenoid components (posterior-wedge, posterior-step and full-wedge) will be virtually implanted in three-dimensional scapulae of patients with asymmetric glenoid erosion by an experienced shoulder surgeon. The quality of bone in anterior and posterior aspects 2.5 mm below each implant will be assessed on the basis of bone density in HU and porosity using a similar method to Objective 1.

Hypothesis 3: It is hypothesized that the posterior wedge implant more accurately represents posterior erosion and will therefore result in the least bone removal for optimal component placement. It is expected that significant differences in the bone density and porosity will exist between anterior and posterior regions with all three augmented component designs.

Objective 4: To biomechanically compare three currently marketed (posterior-wedge, posterior-step and full-wedge) and two modified augmented glenoid component designs using finite element analysis.

This investigation will expand on the results from objective 3 by providing node based strain data that will be used to assess the strain field experienced in the bone underlying each glenoid component. This strain field will be used to determine if strain is correlated to bone density in different regions.

Hypothesis 4: It is hypothesized that the implants that remove the least bone adjacent to the erosion will exhibit less strain and therefore provide a greater underlying surface for early implant support and fixation.

1.7 THESIS OVERVIEW

Following this introduction, Chapter 2 describes regional bone density and porosity in subarticular glenoid bone in patients with glenohumeral osteoarthritis and symmetric or asymmetric glenoid erosion. Chapter 3 expands on patients with asymmetric glenoid erosion and quantifies the morphology of erosion. Chapter 4 describes a virtual implantation method of augmented glenoid components in three-dimensional reconstructions of patient scapulae and evaluates the degree of bone removal and quality of underlying bone in optimally placed components. Chapter 5 expands on the first four chapters by assessing the biomechanical aspects of augmented glenoid component designs, using finite element analysis. This chapter also describes two modified glenoid components that orient the augment (step/wedge) with the erosion - as determined in Chapter 3. Finally, Chapter 6 provides general discussion and places this work within the context of currently available literature while describing the significance, and limitations of this work, as well as recommendations for future work.

1.8 REFERENCES

1. Andreykiv A, Prendergast PJ, van Keulen F, Swieszkowski W, Rozing PM. Bone ingrowth simulation for a concept glenoid component design. J Biomech 2005;38(5):1023–33. doi:10.1016/j.jbiomech.2004.05.044

2. Ashby MF. Materials Selection in Mechanical Design. Burlington, MA: Elsevier Ltd; 2011.

3. Austman RL, Milner JS, Holdsworth DW, Dunning CE. The effect of the density-modulus relationship selected to apply material properties in a finite element model of long bone. J Biomech 2008;41(15):3171–6. doi:10.1016/j.jbiomech.2008.08.017

4. Austman RL, Milner JS, Holdsworth DW, Dunning CE. Development of a customized density–modulus relationship for use in subject-specific finite element models of the ulna. Proc Inst Mech Eng Part H J Eng Med 2009;223(6):787–794. doi:10.1243/09544119JEIM553

5. Bey MJ, Kline SK, Zauel R, Kolowich P a, Lock TR. In Vivo Measurement of Glenohumeral Joint Contact Patterns. EURASIP J Adv Signal Process;2010:2–7. doi:10.1155/2010/162136

6. Boyer PJ, Massimini DF, Gill TJ, Papannagari R, Stewart SL, Warner JP, et al. In vivo articular cartilage contact at the glenohumeral joint: preliminary report. J Orthop Sci 2008;13(4):359–65. doi:10.1007/s00776-008-1237-3

7. Bryce CD, Pennypacker JL, Kulkarni N, Paul EM, Hollenbeak CS, Mosher TJ, et al. Validation of three-dimensional models of in situ scapulae. J Shoulder Elbow Surg 2008;17(5):825–32. doi:10.1016/j.jse.2008.01.141

8. Büchler P, Ramaniraka NA, Rakotomanana LR, Iannotti JP, Farron A. A finite element model of the shoulder: application to the comparison of normal and osteoarthritic joints. Clin Biomech 2002;17(9-10):630–639. doi:10.1016/S0268-0033(02)00106-7

9. Campoli G, Weinans H, van der Helm F, Zadpoor AA. Subject-specific modeling of the scapula bone tissue adaptation. J Biomech 2013;46(14):2434–41. doi:10.1016/j.jbiomech.2013.07.024

10. Carter D, Hayes W. The compressive behavior of bone as a two-phase porous structure. J Bone Jt Surg 1977;59(7):954-962

11. Cattaneo PM, Dalstra M, Frich LH. A three-dimensional finite element model from computed tomography data: A semi-automated method. Proc Inst Mech.Eng Part H J Eng Med;215(2):203–212. doi:10.1243/0954411011533760

12. Clavert P, Millett PJ, Warner JJP. Glenoid resurfacing: what are the limits to asymmetric reaming for posterior erosion? J. Shoulder Elbow Surg 2007;16(6):843–8. doi:10.1016/j.jse.2007.03.015

13. Couteau B, Mansat P, Estivalèzes É, Darmana R, Mansat M, Egan J. Finite element analysis of the mechanical behavior of a scapula implanted with a glenoid prosthesis. Clin Biomech 2001;16(7):566–575. doi:10.1016/S0268-0033(01)00029-8

14. Day JS, Lau E, Ong KL, Williams GR, Ramsey ML, Kurtz SM. Prevalence and projections of total shoulder and elbow arthroplasty in the United States to 2015. J Shoulder Elbow Surg 2010;19(8):1115–20. doi:10.1016/j.jse.2010.02.009

15. Denard PJ, Raiss P, Sowa B, Walch G. Mid- to long-term follow-up of total shoulder arthroplasty using a keeled glenoid in young adults with primary glenohumeral arthritis. J Shoulder Elbow Surg 2013;22(7):894–900. doi:10.1016/j.jse.2012.09.016

16. Denard PJ, Walch G. Current concepts in the surgical management of primary glenohumeral arthritis with a biconcave glenoid. J Shoulder Elbow Surg 2013;22(11):1589–98. doi:10.1016/j.jse.2013.06.017

17. Global Steptech Design Rationale and Surgical Technique. Depuy Orthopaedics. 2011.

18. Ethier CR, Simmons CA. Introductory Biomechanics: From Cells to Organisms. Cambridge University Press; 2007

19. Equinoxe Operative Technique Addedum Exactech Inc. 2011.

20. Farron A, Terrier A, Büchler P. Risks of loosening of a prosthetic glenoid implanted in retroversion. J Shoulder Elbow Surg 2006;15(4):521-526

21. Friedman RJ, Hawthorne KB, Genez BM. The use of computerized tomography in the measurement of glenoid version. J Bone Joint Surg Am 1992;74(7):1032–7.

22. Galante J, Rostoker W, Ray RD. Physical properties of trabecular bone. Calcif Tissue Res 1970;5(1):236–246. doi:10.1007/BF02017552

23. Gerber C, Costouros J. Static posterior humeral head subluxation and total shoulder arthroplasty. J Shoulder Elbow Surg 2009;18(4):505-510

24. Gilmer BB, Comstock BA, Jette JL, Warme WJ, Jackins SE, Matsen FA. The prognosis for improvement in comfort and function after the ream-and-run arthroplasty for glenohumeral arthritis: an analysis of 176 consecutive cases. J Bone Joint Surg Am 2012;94(14):e102. doi:10.2106/JBJS.K.00486

25. Guglielmi G. Osteoporosis and Bone Densitometry Measurements. Berlin, Heidelberg: Springer Berlin Heidelberg; 2013 doi:10.1007/978-3-642-27884-6

26. Gunther SB, Lynch TL, O'Farrell D, Calyore C, Rodenhouse A. Finite element analysis and physiologic testing of a novel, inset glenoid fixation technique. J Shoulder Elbow Surg 2012;21(6):795–803. doi:10.1016/j.jse.2011.08.073

27. Gupta S, Helm F Van der, Keulen F Van. Stress analysis of cemented glenoid prostheses in total shoulder arthroplasty. J Biomech 2004

28. Harryman D, Sidles J, Clark J. Translation of the humeral head on the glenoid with passive glenohumeral motion. J Bone Joint Surg 1990;72(9):1334-1343

29. Helgason B, Perilli E, Schileo E. Mathematical relationships between bone density and mechanical properties: a literature review. Clin Biomech 2008;23(2):135-146

30. Hendel M, Bryan J. Comparison of Patient-Specific Instruments with Standard Surgical Instruments in Determining Glenoid Component Position: A Randomized Prospective Clinical Trial. J Bone Joint Surg 2012;94(23):2167-2175

31. Hermida J. Augmented wedge-shaped glenoid component for the correction of glenoid retroversion: a finite element analysis. J Shoulder Elbow Surg 2014;23(3):347-354

32. Hopkins, Andrew R., et al. Wear in the prosthetic shoulder: association with design parameters. J Biomech Eng 2007; 129(2): 223-230.

33. Hopkins, Andrew R., et al. Wear in the prosthetic shoulder: association with design parameters. J Biomech Eng 2007; 129(2): 223-230.

34. Hopkins AR, Hansen UN, Amis A. Finite element models of total shoulder replacement: Application of boundary conditions. Comput Methods Biomech Biomed Engin;8(1):39–44. doi:10.1080/10255840500075205

35. Howell S, Galinat B, Renzi A, Marone P. Normal and abnormal mechanics of the glenohumeral joint in the horizontal plane. J Bone Jt Surg 1988;70(2):227-232

36. Hsu JE, Ricchetti ET, Huffman GR, Iannotti JP, Glaser DL. Addressing glenoid bone deficiency and asymmetric posterior erosion in shoulder arthroplasty. J Shoulder Elbow Surg 2013;22(9):1298–308. doi:10.1016/j.jse.2013.04.014

37. Iannotti JP, Gabriel JP, Schneck SL, Evans BG, Misra S. The normal glenohumeral relationships. An anatomical study of one hundred and forty shoulders. J Bone Joint Surg Am 1992;74(4):491–500.

38. Kwon Y, Powell K, Yum J. Use of three-dimensional computed tomography for the analysis of the glenoid anatomy. J Shoulder Elbow Surg 2005; 14(1):85-90

39. Mansat P, Briot J, Mansat M, Swider P. Evaluation of the glenoid implant survival using a biomechanical finite element analysis: influence of the implant design, bone properties, and loading location. J. Shoulder Elbow Surg 2007;16(3):S79-S83

40. Massimini DF, Li G, Warner JP. Glenohumeral contact kinematics in patients after total shoulder arthroplasty. J Bone Joint Surg Am 2010;92:916–926. doi:10.2106/JBJS.H.01610

41. Matsen F, Warme WJ, Jackins SE. Can the Ream and Run Procedure Improve Glenohumeral Relationships and Function for Shoulders With the Arthritic Triad? Clin Orthop Rela. Res 2014;2–9. doi:10.1007/s11999-014-4095-7

42. Matsen F, Lippitt S. Current Technique for the Ream-and-Run Arthroplasty for Glenohumeral Osteoarthritis. J Bone Jt Surg 2012;e20-21

43. Matsen F, Warme WJ, Jackins SE. Can the Ream and Run Procedure Improve Glenohumeral Relationships and Function for Shoulders With the Arthritic Triad? Clin Orthop Rela. Res 2014;2–9. doi:10.1007/s11999-014-4095-7

44. Matsumura N, Ogawa K, Kobayashi S, Oki S, Watanabe A, Ikegami H, et al. Morphologic features of humeral head and glenoid version in the normal glenohumeral joint. J Shoulder Elbow Surg 2014;23(11):1724–30. doi:10.1016/j.jse.2014.02.020

45. Mazess R, Barden H. Dual-energy x-ray absorptiometry for total-body and regional bone-mineral and soft-tissue composition. Am J Clin Nutr 1990;51(6):1106-1112

46. McCoy S, Warren R, III HB. Total shoulder arthroplasty in rheumatoid arthritis. J Arthoplasty;4(2):105-113

47. Mercer D, Gilmer B. A quantitative method for determining medial migration of the humeral head after shoulder arthroplasty: preliminary results in assessing glenoid wear at a minimum of. J Shoulder Elbow Surg 2011; 20(2):301-307

48. Morgan E, Bayraktar H, Keaveny T. Trabecular bone modulus–density relationships depend on anatomic site. J Biomech 2003;36(7):897-904

49. Nordin M, Frankel V. Basic biomechanics of the musculoskeletal system. 2001. Lippincott Williams & Wilkins

50. Patel R, Wright T, Gao Y. Load transfer after cemented total shoulder arthroplasty. J Shoulder Elbow Surg 2014; In-Press

51. Poppen N, Walker P. Normal and abnormal motion of the shoulder. J Bone Jt Surg 1976;58(2):195-201

52. Rho J, Hobatho M, Ashman R. Relations of mechanical properties to density and CT numbers in human bone. Med Eng Phys 1995;17(5):347-355

53. Rice J, Cowin S, Bowman J. On the dependence of the elasticity and strength of cancellous bone on apparent density. J Biomech 1988; 21(2):155-168

54. Roche C, Diep P. Biomechanical Impact of Posterior Glenoid Wear on Anatomic Total Shoulder Arthroplasty. Bull Hosp Joint Disease 2013;71:S5-11

55. Schaffler M, Burr D. Stiffness of compact bone: effects of porosity and density. J Biomech 1988;21(1):13-16

56. Schileo E, Dall'Ara E, Taddei F. An accurate estimation of bone density improves the accuracy of subject-specific finite element models. J Biomech 2008;41(11):2483-2491

57. Sears BW, Johnston PS, Ramsey ML, Williams GR. Glenoid Bone Loss in Primary Total Shoulder Arthroplasty. J Am Acad Orth Surg 2012;20(9):604-613

58. Sharma GB, Debski RE, McMahon PJ, Robertson DD. Adaptive glenoid bone remodeling simulation. J Biomech 2009;42(10):1460–8. doi:10.1016/j.jbiomech.2009.04.002

59. Smithers C, Young A, Walch G. Reverse shoulder arthroplasty. Curr Rev Musculoskelet Med 2011;4(4):183-190

60. Sophia Fox AJ, Bedi A, Rodeo SA. The basic science of articular cartilage: structure, composition, and function. Sports Health 2009;1(6):461–8. doi:10.1177/1941738109350438

61. Stone K, Grabowski J, Cofield R. Stress analyses of glenoid components in total shoulder arthroplasty. J Shoulder Elbow Surg 1999; 8(2):151-158

62. Suárez D, Weinans H, Keulen F van. Bone remodelling around a cementless glenoid component. Biomech Model 2012; 11(6):903-913

63. Terrier A, Brighenti V, Pioletti D, Farron A. Importance of polyethylene thickness in total shoulder arthroplasty: A finite element analysis. Clin Biomech 2012;27(5):443-448

64. Terrier A, Büchler P, Farron A. Bone–cement interface of the glenoid component: stress analysis for varying cement thickness. Clin Biomech 2005;20(7):710-717

65. Terrier A, Büchler P, Farron A. Influence of glenohumeral conformity on glenoid stresses after total shoulder arthroplasty. J Shoulder Elbow Surg 2006;15(4):515-520

66. Veeger H. The position of the rotation center of the glenohumeral joint. J Biomech 2000; 33(12):1711-1715

67. Walch G, Ascani C. Static posterior subluxation of the humeral head: an unrecognized entity responsible for glenohumeral osteoarthritis in the young adult. J Shoulder Elbow Surg 2002; 11(4):309-314

68. Walch G, Badet R, Boulahia A, Khoury A. Morphologic study of the Glenoid in primary glenohumeral osteoarthritis. J Arthroplasty 1999;14(6):756–760. doi:10.1016/S0883-5403(99)90232-2

69. Walch G, Moraga C. Results of anatomic nonconstrained prosthesis in primary osteoarthritis with biconcave glenoid. J Shoulder Elbow Surg 2012;21(11):1526-1533

70. Walch G, Vezeridis P, Boileau P. Three-dimensional planning and use of patient-specific guides improve glenoid component position: an in vitro study. J Shoulder Elbow Surg 2014; In-Press

71. Walch G, Young A, Boileau P. Patterns of loosening of polyethylene keeled glenoid components after shoulder arthroplasty for primary osteoarthritis. J Bone Joint Surg 2012;94(2):145-150

72. Wang V, Krishnan R. Biomechanical evaluation of a novel glenoid design in total shoulder arthroplasty. J Shoulder Elbow Surg 2005; 14(1):S129-S140

73. Weinans H, Huiskes R, Grootenboer HJ. Effects of material properties of femoral hip components on bone remodeling. J Orthop Res 1992;10(6):845–53 doi:10.1002/jor.1100100614

74. Wolff J. The law of bone remodeling. Verlag von August Hirchwald. Berlin. 1892

75. Zhang J, Yongpravat C, Kim H. Glenoid articular conformity affects stress distributions in total shoulder arthroplasty. J Shoulder Elbow Surg 2013;22(3):350-356

76. Basic Biomechanics of the Musculoskeletal System. Lippincott Williams & Wilkins; 2001

CHAPTER 2 - REGIONAL BONE DENSITY VARIATIONS IN OSTEOARTHRTIC GLENOIDS: A COMPARISON OF SYMMETRIC AND ASYMMETRIC (TYPE B2) EROSION PATTERNS

OVERVIEW: *Subchondral bone density variations are known to occur as the result of cartilage degeneration in osteoarthritic joints. In the shoulder, glenoid bone erosion uncharacteristic of osteoarthritis is often observed. In cases where erosion occurs symmetrically, the resulting bone density is thought to be uniform across the surface of the glenoid. However, in cases with asymmetric erosion, we hypothesized that bone density is not uniform across the glenoid surface, due to the altered kinematics of the joint and the resultant altered stress distribution. This chapter evaluated patients with glenohumeral osteoarthritis with symmetric erosion (n=25) and asymmetric erosion (n=25) in order to characterize regional bone density variations. Porosity of the bone was also quantified using a void ratio method.*[1]

1) A version of this work has been published: Knowles NK, Athwal GS, Keener JD, Ferreira LM, Regional Bone Density Variations in Osteoarthritic Glenoids: A Comparison of Symmetric to Asymmetric (Type B2) Erosion Patterns. *Journal of Shoulder and Elbow Surgery* 2015; 24(3):425-432

2.1 INTRODUCTION:

In patients with osteoarthritis undergoing total shoulder arthroplasty, the long-term survivability of cemented polyethylene glenoid components have been concerning.[5,7,12,31] Typically, failures are described as multi-factorial;[1,13] however, aseptic loosening of glenoid components remains a leading cause of revision surgery.[2,9,23,32] Initial glenoid fixation is theorized to be an important factor in improving implant survivability. Additionally, it has been reported that preservation of the dense sclerotic remaining bone of the arthritic glenoid may be an important factor in decreasing implant migration and failure.[29]

Walch et. al. recommend minimal glenoid reaming to preserve the dense sclerotic "subchondral" bone to provide uniform underlying support of the implant.[29,30] Many other studies have often referred to the glenoid bone as subchondral;"[16,18,20,24,25,34] however, in osteoarthritis the chondral layer is often partially or completely absent. As such, we propose this glenoid bone be referred to as "subarticular" rather than "subchondral".

In patients with symmetric glenoid wear (Figure 2.1A), the dense sclerotic bone is theorized to be uniformly distributed over the glenoid articular surface to allow support of the implant to limit medial or tilting migration. However, there is little data specific to the arthritic glenoids structure to determine if the bone density is evenly distributed or if there are regional variations. Additionally, in cases classified by Walch et al.[28] as type B2, the effect of asymmetric wear with a resultant biconcave glenoid (Figure 2.1B) on the regional bone density characteristics is unknown. Preservation of the dense sclerotic bone is technically easier when the glenoid is symmetrically eroded. However, when an asymmetrically posteriorly eroded glenoid requires asymmetric reaming, or an augmented implant to correct retroversion, the regional bone quality characteristics of the glenoid are unknown

Accurate characterization of regional variations in bone density in symmetric and asymmetric glenoid erosion patterns can assist with surgical planning, intra-operative glenoid preparation, and direct strategies for addressing bone loss. In addition,

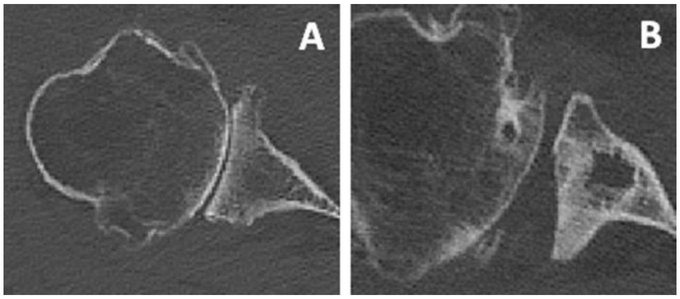

Figure 2.1: Representative axial CT images of glenoid erosion associated with osteoarthritis.

A: A right shoulder axial image of a symmetric erosion pattern. **B:** A right shoulder axial image of an asymmetric biconcave erosion pattern.

understanding the location of the highest quality dense glenoid bone may potentially guide the design of augmented glenoid components that utilize preparation techniques that minimize quality bone removal to maximize glenoid component support and fixation. Minimizing structural bone removal has the potential to increase the long-term survivability of glenoid implants.

The purpose of this study was to characterize regional bone density and porosity variations in osteoarthritic glenoids. Our first objective was to determine if bone density and porosity in a symmetrically eroded glenoid is uniformly distributed. Our second objective was to determine if glenoids with asymmetric posterior biconcavity have regional variations in bone density. We hypothesized, based on clinical experience that altered glenohumeral contact kinematics in biconcave glenoids leads to increased bone density in the posterior eroded region compared to the anterior region.

2.2 MATERIALS AND METHODS:

Clinical computed tomography (CT) scans were acquired from 50 patients with osteoarthritis who had previously undergone total shoulder arthroplasty at one of two institutions. CT scans are routinely obtained for templating purposes for patients scheduled for anatomic total shoulder arthroplasty. Two cohorts were created: cohort #1 consisted of 25 patients with osteoarthritis and symmetric glenoid wear without biconcavity (mean age: 68 ± 10 years, 11 male); cohort #2 consisted of 25 patients with osteoarthritis and asymmetric biconcave (B2) posterior wear (mean age: 65 ± 11 years, 17 male). All CT scans were classified by two experienced shoulder surgeons (G.S.A, J.D.K) utilizing a method which has been shown to be clinically acceptable.[22] All scans were completed using multi-slice scanners with standard clinical settings (120 to 140 kVp, 512x512 resolution).

The CT images were uploaded in digital imaging in communications and medicine (DICOM) format to medical imaging software (Mimics® V. 15.01, Materialize, Leuven, BE). Thresholding was set to a minimum value of 200 Hounsfield Units (HU) to include both cancellous and cortical bone and to preserve glenoid anatomy during segmentation.[3,16] The humerus was separated from the glenoid using manual segmentation techniques and three-dimensional reconstructions of each patient's scapula were generated as stereolithography (STL) files.

An orthogonal coordinate system was created in all 50 patients to separate the glenoid articular surface into quadrants (Figure 2.2A). A central superoinferior axis, defined by superior and inferior points, was created and a perpendicular bisector at the axis midpoint separated the glenoid into quadrants, similar to the method described by De Wilde et al.[10] The quadrants were named: anterosuperior, anteroinferior, posterosuperior and posteroinferior. In the asymmetric (B2) cohort, in addition to the aforementioned coordinate system, the glenoid was divided based on the erosion line. As seen in figure 2.2B, the biconcave glenoid has a predictable erosion pattern with posteroinferior bone loss. This biconcavity produces 2 articular facets; the anterior facet, which no longer articulates with the humeral head and is termed the paleoglenoid, and the posterior facet, which now articulates with the humeral head and is referred to as the neoglenoid.[8,29] The obliquely oriented ridge of bone between these two facets is termed the erosion line, and is clearly visible in axial CT images (Figure 2.1B). The erosion line was marked with a

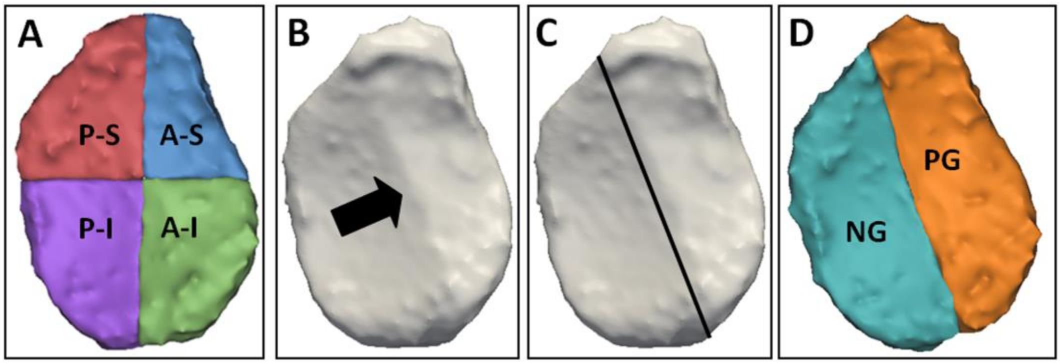

Figure 2.2: Three-dimensional reconstructions of a representative osteoarthritic glenoid exhibiting an asymmetric biconcave (B2) erosion pattern.

A: An orthogonal quadrant coordinate system defined by the most superior and inferior points on the glenoid rim, and a perpendicular bi-sector at the vertical axis midpoint. The glenoid was separated into anterosuperior (A-S), posterosuperior (P-S), anteroinferior (A-I), and posteroinferior (P-I) quadrants. **B:** The black arrow indicates the line of erosion, which is the ridge of bone separating the glenoid articular surface into anterior (paleoglenoid) and posterior (neoglenoid) facets. **C:** The asymmetric erosion coordinate system defined by the best fit line along the line of erosion, separating the glenoid into anterior (paleoglenoid) and posterior (neoglenoid) facets. **D:** The paleoglenoid (PG) and neoglenoid (NG) measurement regions.

linear best-fit line that was used to separate the asymmetric glenoids in to the neoglenoid and paleoglenoid (Figure 2.2C).

Computed tomography images of the arthritic glenoids were re-sliced sagittal to the articulation separately in anterior and posterior regions to allow for accurate depth measurements. This was most important in the asymmetric (B2) cohort to account for the altered version angle created by the posterior erosion. This method was also used for the symmetric erosion cohort for completeness. The subarticular bone structure of the glenoid vault was further divided into volumes at depths of 0 to 2.5 mm and 2.5 to 5 mm from the most medial point on the glenoid articular surface (Figure 2.3).

Average density was measured in Hounsfield Units (HU) in each of the four glenoid quadrants and in the neoglenoid and paleoglenoid of the asymmetric (B2) glenoids using Mimics®. Volumes of material within the glenoid vault that were below the 200 HU threshold limit corresponded to cysts and/or very low density cancellous bone. These very low density cystic areas were considered to be voids. These void volumes were included to quantify bone quality as the fraction of void volume to total volume (i.e. void fraction) in each region. Average density within these regions, including voids, was also measured using Mimics® built-in functions.

Statistical analysis (SigmaPlot V. 11.0, Systat Software Inc., Germany) was performed to determine density variations in each quadrant using a one-way analysis of variance (ANOVA) and void fraction by quadrant using a Kruskall-Wallis one-way analysis of variance (ANOVA) on ranks. A Tukey Post-Hoc test was used for pairwise comparisons separately for each cohort and depth (0-2.5 and 2.5-5 mm). Density and void fraction variations between the neoglenoid and paleoglenoid in asymmetric (B2) glenoids were determined using paired t-tests at each depth. Comparisons between the symmetric and asymmetric cohorts were completed separately by depth and density or void fraction using two-way analysis of variance (ANOVA) with Tukey Post-Hoc tests for pairwise comparisons. Significance was set at $p<0.05$.

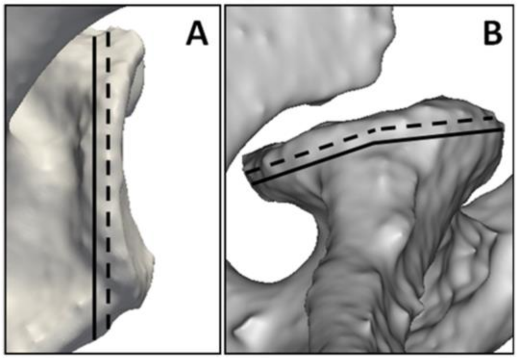

Figure 2.3: A three-dimensional reconstruction of a scapula showing measured depth regions

A: A coronal image depicting the depth regions 0 – 2.5 mm (dashed line) and 2.5 – 5 mm (solid line) from center of glenoid articulation. Planes were drawn separately in anterior and posterior regions to ensure consistent depths were maintained regardless of version angle caused by biconcavity. The 0 – 2.5 mm depth region includes all bone lateral to the dashed line, while the 2.5 – 5 mm depth regions included the bone between the dashed and solid lines. **B:** An axial 3D view illustrating the slight variation in angled depth regions to account for the altered version angle caused by biconcavity. Note the dense cortical bone of the scapular neck is avoided by the re-sliced sagittal regions.

2.3 RESULTS

The mean glenoid density for all 50 patients was 579 ± 104 HU. The mean density for patients with symmetric glenoid erosion was 583 ± 101 HU, which was not significantly different than the mean density for patients with asymmetric (B2) posterior erosion 576 ± 107 HU ($p = 0.479$). Overall, the lowest mean density measurement was obtained from the anteroinferior quadrant in the asymmetric cohort at a 2.5 to 5 mm depth (334 HU). Conversely, the highest mean density per quadrant was found in the posteroinferior quadrant of the symmetric cohort at a depth of 2.5 - 5mm (900 HU).

In the symmetric cohort, there were no significant differences in bone density between quadrants at either depth ($p = 0.759$ at 0 to 2.5 mm; $p = 0.089$ at 2.5 to 5 mm) (Figure 2.4). In the asymmetric (B2) cohort, however, significant differences in density as a function of location were identified. Specifically, at the 0 to 2.5 mm depth, the posteroinferior quadrant was a mean of 112 HU denser than the anterosuperior quadrant ($p < 0.001$) and 79 HU denser than the anteroinferior quadrant ($p = 0.007$). At the same depth, the posterosuperior quadrant was a mean of 66 HU denser than the anterosuperior quadrant ($p = 0.033$). At the 2.5 to 5 mm depth, the posteroinferior quadrant was on average, 188 HU denser than the anterosuperior quadrant ($p < 0.001$), 150 HU denser than the anteroinferior quadrant ($p < 0.001$), and 139 HU denser than the posterosuperior quadrant ($p < 0.001$).

When voids were included in the density measurements for the symmetric cohort, overall density was reduced an average of 68 HU; however there was only a significant difference in density at the 2.5 to 5 mm depth ($p < 0.05$). Including the voids in the density measurements for the asymmetric cohort resulted in an average density reduction of 71 HU. This was considered a significant reduction at both the 0 to 2.5 mm ($p < 0.001$) and 2.5 to 5 mm depths ($p < 0.001$).

The void fraction, which is the proportion of volume within the glenoid vault occupied by cysts and/or very low density cancellous bone, for the symmetric cohort (Figure 2.5) was significantly different between quadrants at both the 0 to 2.5 mm

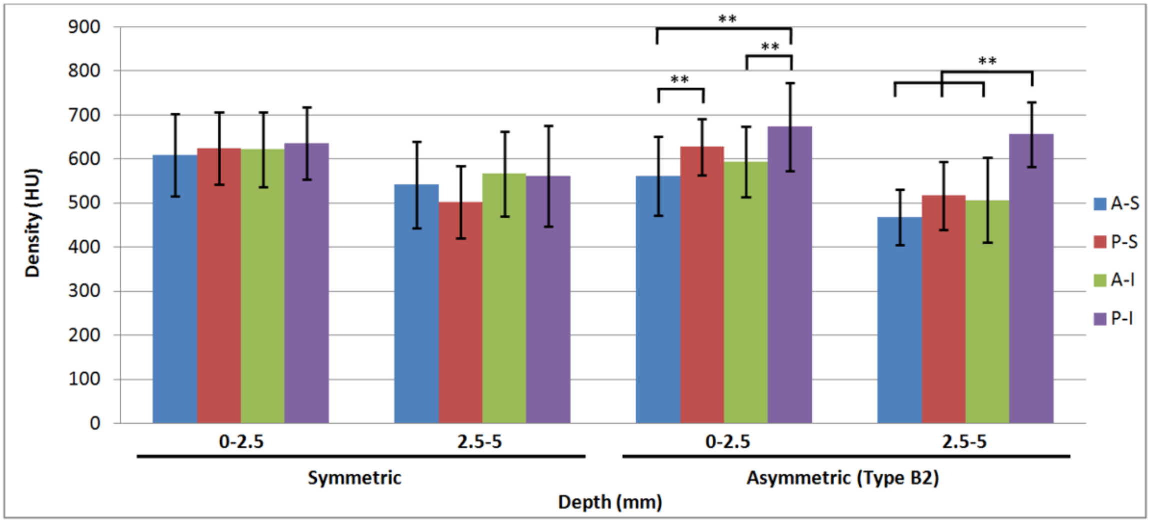

Figure 2.4: Symmetric and asymmetric eroded glenoid bone density

Mean bone density, in Hounsfield Units (HU), by glenoid quadrant in patients with and without posterior erosion of the glenoid at depths of 0 to 2.5 mm and 2.5 to 5 mm from the glenoid surface. Anterosuperior (A-S), posterosuperior (P-S), anteroinferior (A-I) and posteroinferior (P-I). There were no significant differences in density for patients with a symmetric wear pattern (n=25) (0 to 2.5 mm: $p = 0.759$; 2.5 to 5 mm: $p = 0.089$). There was a significant difference in glenoid bone density for patients with asymmetric posterior erosion (B2) at both depths (n=25). Significant differences are denoted by **, $p < 0.01$.

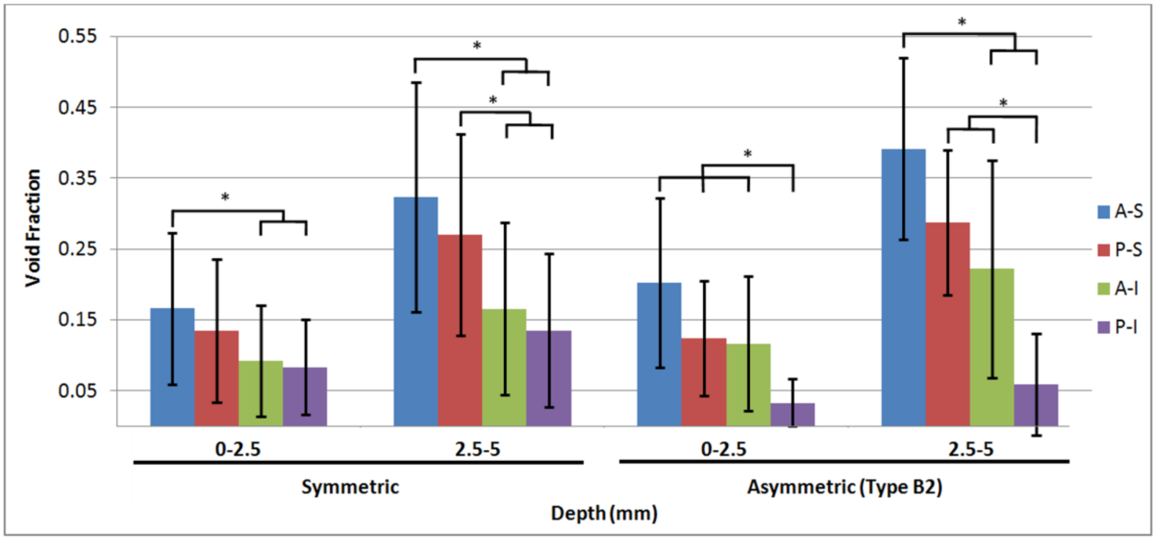

Figure 2.5: Symmetric and asymmetric eroded glenoid void fraction

Mean fraction of void volume (i.e. cysts, voids or cancellous bone below 200 HU threshold) to total volume by glenoid quadrant at depths 0 to 2.5 mm and 2.5 to 5 mm from the glenoid surface. Anterosuperior (A-S), posterosuperior (P-S), anteroinferior (A-I) and posteroinferior (P-I). There was a significant difference for patients with symmetric erosion at both depths (n=25) and for patients with asymmetric posterior erosion (B2) at both depths (n=25). Significant differences are denoted by *, $p < 0.05$.

($p = 0.004$) and 2.5 to 5 mm depths ($p < 0.001$). The superior quadrants (anterosuperior and posterosuperior) contained significantly more cysts ($p < 0.05$) than the inferior quadrants. In the asymmetric cohort, the void fraction was significantly different at both the 0 to 2.5 mm ($p < 0.001$) and 2.5 to 5 mm depths ($p < 0.001$) (Figure 2.5). At the 0 to 2.5 mm depth, the posteroinferior quadrant had a significantly lower void fraction than all other quadrants ($p < 0.05$). At the 2.5 to 5 mm depth, once again the posteroinferior quadrant had a significantly lower void fraction, indicating a very low volume of cysts or voids, meaning more dense homogenous bone ($p < 0.05$ for all comparisons).

When the paleoglenoid was compared to the neoglenoid in the asymmetric cohort, the neoglenoid bone was significantly ($p < 0.001$) denser (Figure 2.6A). At the 0 to 2.5 mm depth, the neoglenoid was, on average, 94 HU denser than the paleoglenoid ($p < 0.001$) and 156 HU more dense at the 2.5 to 5 mm depth ($p < 0.001$). When examining the void fraction, the neoglenoid bone volume had a significantly lower incidence of glenoid cysts or voids ($p < 0.001$) (Figure 2.6B).

When directly comparing quadrants between the symmetric and asymmetric cohorts, at the 0-2.5 mm depth, the anterosuperior quadrant of the symmetric cohort was a mean 48 HU denser than the asymmetric cohort ($p < 0.05$), with no significant difference between the other three quadrants. At the 2.5 – 5 mm depth, the anterosuperior and anteroinferior quadrants of the symmetric cohort were a mean of 74 HU and 60 HU denser than the corresponding quadrants in the asymmetric cohort, respectively ($p < 0.05$). At the same depth, the posteroinferior quadrant of the asymmetric cohort was a mean 94 HU denser than the symmetric cohort ($p < 0.05$). There was no significant difference in void fraction of the quadrants between cohorts at either measured depth.

2.4 DISCUSSION

Hounsfield Units (HU) have been found to be effective in the estimation of subarticular bone mineral density and have also been used to assist in the early

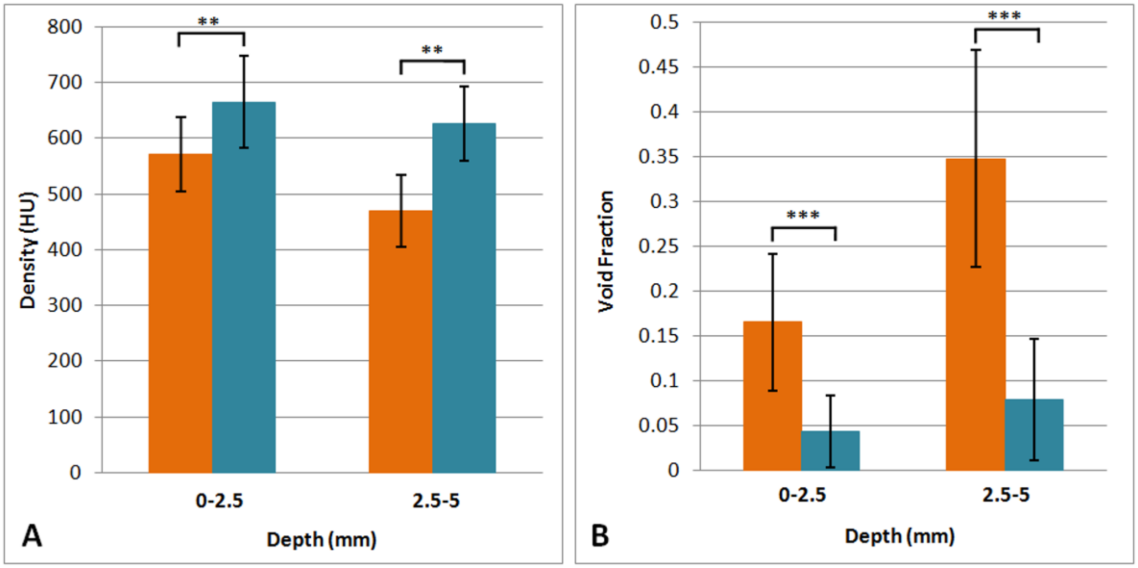

Figure 2.6: Asymmetric eroded bone density and void fraction

A: The mean bone density of asymmetric B2 glenoids, in Hounsfield Units (HU), anterior (orange) and posterior (teal) to the line of erosion at depths of 0 to 2.5 mm and 2.5 to 5 mm from the glenoid surface (n = 25). Anterior regions were significantly less dense than posterior regions at both depths. **B:** Mean fraction of void volume (i.e. cysts, voids or cancellous bone below 200 HU threshold) to total volume, anterior (orange) and posterior (teal) to the line of erosion at depths of 0 to 2.5 mm and 2.5 to 5 mm from the glenoid surface (n= 25). Regions anterior to the erosion line showed significantly more voids than posterior regions at both depths. Significant differences are denoted by **, $p < 0.01$; ***, $p < 0.001$.

diagnosis of osteoporosis.[24] Previous studies have assessed bone density on the basis of HU in normal glenoids[18,20,25,34] and preliminarily in arthritic glenoids.[6] However, a comprehensive evaluation of regional density variations in osteoarthritic glenoids, including more complex B2 erosion patterns, has not been reported. This knowledge is valuable to direct glenoid preparation and bone preservation strategies during total shoulder arthroplasty.

In our study, the results indicate that patients with osteoarthritis and a symmetric glenoid wear pattern have relatively uniform glenoid bone density. Therefore, when symmetrically reaming the glenoid in preparation for an all-polyethylene cemented implant, the density of the post-reaming glenoid surface should be relatively uniform to provide balanced support of the implant, as recommended by Walch et al.[30] Conversely, in patients with asymmetric posterior erosion with a B2 glenoid, substantial regional variations in bone density have been found. Bone density was found to be substantially higher in the posteroinferior quadrant of the glenoid and in the neoglenoid region. This variation in bone density is likely due to the altered kinematics and joint alignment that is associated with biconcavity. Typically, the humeral head subluxates posteriorly, and articulates with the neoglenoid, which has a smaller surface area than the native glenoid. This neo-articulation over a smaller surface area likely leads to a concentration of joint load with resultant adaptive bone changes to the posterior glenoid. Following Wolff's law, the bone in the neoglenoid adapts to the increased stresses by becoming stronger, thicker and denser. Similarly, because the humeral head is no longer articulating with the anterior facet, or the paleoglenoid, it undergoes adaptive changes to become significantly less dense and relatively osteopenic.

In asymmetric wear patterns, as in symmetric, it is also important to preserve high quality bone to provide support for the glenoid implant. Unfortunately, in asymmetric (B2) glenoids implant survivability is confounded by potentially increased component retroversion and posterior humeral head subluxation.[11,14,15,27] It has been recommended that in cases of mild or moderate glenoid retroversion, asymmetric reaming of the anterior facet to correct retroversion malalignment is preferable.[4,8,17,26] Our bone density results would indicate that asymmetric reaming of the anterior facet would typically remove more poor quality anterior bone and relatively preserve the better quality posterior bone. The end result of asymmetric reaming would leave a reamed glenoid surface with drastic regional differences in bone quality, with the anterior half being reamed in to the cancellous bone with substantially lower bone density and the posterior half containing better quality dense bone. The leveling of the glenoid to correct retroversion leads to better articular alignment; however, the non-uniform support of the glenoid implant may lead to implant migration and possibly subsidence in the longer term.

In cases of higher retroversion, greater than 15-18 degrees, that cannot be corrected by asymmetric reaming,[4,21] other treatment strategies may be preferable. Options for greater degrees of posterior bone loss include structural bonegrafting, augmented implants and reverse shoulder arthroplasty. Augmented glenoid implants typically replace the volume of bone loss with metal or polyethylene. Some commercially available systems require partial removal of the posterior bone to allow insertion of the augmented implant. This strategy requires sacrifice of some of the highest quality and most dense posterior quadrant bone to accommodate the shape of the implant. Our results indicate that subarticular bone density in the region posterior to the erosion line was significantly denser and essentially free of voids, compared to the other regions tested, which had significantly higher void fractions. Perhaps another strategy would be to modify the shape of augmented glenoid implant to allow for preservation of the highest quality bone while simultaneously allowing corrective augmentation and a biomechanically favorable environment to promote implant stability and survivability. Preservation of this high quality bone may optimize component fixation and support, theoretically, decreasing the potential for component loosening over time. Additionally, implant designs that could also correct retroversion and recreate the glenohumeral joint line with minimal reaming of the anterior paleoglenoid may be beneficial.

The analysis of the void fraction in our cohorts was also interesting in that regional variations in glenoid cysts and porosity were observed. In both cohorts, the void fraction was greatest in the anterosuperior quadrant and least in the posteroinferior quadrant (Figure 2.5). The void fraction in all quadrants increased as depth increased, indicating not surprisingly, that porosity is greater with increased depth from the articular surface. Increased porosity suggests targeted bone remodeling as a response to low internal stresses and was observed in the mean density results for the asymmetric cohort, but not in the symmetric cohort. It is possible that this is due to the fact that the mean density measurements included only bone above the 200 HU threshold, ignoring voids, a practice that is consistent with the literature.[3,16] When void values were manually included in the mean density measurements, the mean density decreased as expected. However, the decrease in density did not show the same pattern as the void fraction results. It is logical that, in the presence of voids within bone, the density of the remaining bone likely increases in order to maintain the overall strength of the subarticular structure. This is likely the reason that the mean density, with or without voids, did not correlate to the void fraction.

A strength of this study was that porosity of the glenoid vault structure was quantified by its void fraction. This method is commonly used to measure porosity in multiple engineering fields, including tissue engineering.[33] It is a fitting metric given the structural nature of the subarticular regions, and the concept of bone presence is integral when considering implant fixation. In comparison to our void fraction results, Mimar et al.[19] studied bone volume (BV) as a function of total volume (TV) in 19 normal cadaveric glenoids. Porosity was quantified in cancellous bone after digital removal of the cortical shell of the glenoid following micro-CT scanning in small cylindrical regions. The porosity results of Mimar et al.[19] indicate less porous posterior regions and more porous anteroinferior regions, with the lowest quality bone in the inferior regions of the glenoid. It is difficult to quantify these differences between the normal specimens used in their study and the osteoarthritic patients used in the present study due to differences in methodology and pathology. However, in our study of osteoarthritic glenoids we demonstrated increased porosity in the superior quadrants, with increased bone density posterior and specifically in the posteroinferior quadrant in biconcave patients. These differences identified between normal and osteoarthritic glenoids may be an affect of Wolff’s law or of another process that is as of yet unknown.

A potential limitation of our study was the manual segmentation method required in the Mimics® software. Due to the difficulty in manually removing calcified and osteophyte regions from two-dimensional CT images of the glenoid, these regions were included in the HU density measurements. This may have affected density measurements in patients with these conditions, however due to the prevalence of osteophyte formations, the values were likely affected evenly among patients and quadrants.

2.5 REFERENCES

1. Bohsali KI, Wirth MA, Rockwood Jr CA. Complications of total shoulder arthroplasty. J Bone Joint Surg 2006; 88: 2279-2292. doi: 10.2106/JBJS.F.00125

2. Bonnevialle N, Melis B, Neyton L, Favard L, Mole D, Walch G, et al. Aseptic glenoid loosening or failure in total shoulder arthroplasty: revision with glenoid reimplantation. J Shoulder Elbow Surg 2013;22:745-51. doi: 10.1016/j.jse.2012.08.009

3. Bryce CD, Pennypacker JL, Kulkami N, Paul EM, Hollenbeak, Masher TJ, et al. Validation of three-dimensional models of in situ scapulae. J Shoulder Elbow Surg 2008; 17:825-832. doi: 10.1016/j.jse.2008.01.141

4. Clavert P, Millett PJ, Warner JJ. Glenoid resurfacing: What are the limits to asymmetric reaming for posterior erosion? J Shoulder Elbow Surg 2007; 16: 843-848. doi: 10.1016/j.jse.2007.03.015

5. Collin P, Tay AK, Melis B, Boileau P, Walch G. A ten-year radiologic comparison of two-all polyethylene glenoid component designs: a prospective trial. J Shoulder Elbow Surg 2011; 20; 1217-1223. doi: 10.1016/j.jse.2011.06.012

6. Couteau B, Mansat P, Mansat M, Darmana R, Egan J. In vivo characterization of glenoid with use of computed tomography. J Shoulder Elbow Surg 2001; 10:116-122.

7. Denard PJ, Raiss P, Sowa B, Walch G. Mid-to long-term follow-up of total shoulder arthroplasty using a keeled glenoid in young adults with primary glenohumeral arthritis. J Shoulder Elbow Surg 2013; 22:894-900. doi: 10.1016/j.jse.2012.09.016

8. Denard PJ, Walch G. Current concepts in the surgical management of primary glenohumeral arthritis with a biconcave glenoid. J Shoulder Elbow Surg 2013; 22:1589-1598. doi: 10.1016/j.jse.2013.06.017

9. Deutsch A, Abboud JA, Kelly J, Mody M, Norris T, RamseyM L, et al. Clinical results of revision shoulder arthroplasty for glenoid component loosening. J Shoulder Elbow Surg 2007; 16: 706-716. doi: 10.1016/j.jse.2007.01.007

10. De Wilde LF, Berghs BM, Audenaert, Sys G, Van Maele GO, Barbaix. About the variability of the shape of the glenoid cavity. Surg Radiol Anat 2004; 26:54-59. doi: 10.1007/s00276-003-0167-1

11. Farron A, Terrier A, Büchler P. Risks of loosening of a prosthetic glenoid implanted in retroversion. J Shoulder Elbow Surg 2006; 15: 521-526. doi: 10.1016/j.jse.2005.10.003

12. Fox TJ, Cil A, Sperling JW, Sanchez-Sotelo J, Schleck CD, Cofield RH. Survival of the glenoid component in shoulder arthroplasty. J Shoulder Elbow Surg 2009;18:859-63. doi: 10.1016/j.jse.2008.11.020

13. Franta AK, Lenters TR, Mounce D, Neradilek B, Matsen III FA.The complex characteristics of 282 unsatisfactory shoulder arthroplasties. J Shoulder Elbow Surg 2007;16: 555-562. doi: 10.1016/j.jse.2006.11.004

14. Friedman RJ, Hawthorn KB, Genez BM. The use of computerized tomography in the measurement of glenoid version. J Shoulder Elbow Surg 1992;74:1032-1037.

15. Ganapathi A, McCarron JA, Chen X, Iannotti JP. Predicting normal glenoid version from the pathologic scapula: a comparison of 4 methods in 2-and 3-dimensional models. J Shoulder Elbow Surg 2011; 20: 234-244. doi: 10.1016/j.jse.2010.05.024

16. Haverstock JP, Katchky RN, Lalone EA, Faber KJ, King GJW, Athwal GS. Regional variations in radial head bone volume and density: implications for fracture patterns and fixation. J Shoulder Elbow Surg 2012; 21:1669-1673. doi: 10.1016/j.jse.2012.07.002

17. Hsu JE, Ricchetti ET, Huffman GR, Iannotti JP, Glaser DL. Addressing glenoid bone deficiency and asymmetric posterior erosion in shoulder arthroplasty. J Shoulder Elbow Surg 2013; 22:1298-1308. doi: 10.1016/j.jse.2013.04.014

18. Kraljević M, Zumstein V, Wirz D, Hügli R, Müller-Gerbl M. Mineralization and mechanical strength of the glenoid cavity subchondral bone plate. Int Orthop 2011; 35: 1813-1819. doi: 10.1007/s00264-011-1308-5

19. Mimar R, Limb D, Hall RM. Evaluation of the mechanical and architectural properties of glenoid bone. J Shoulder Elbow Surg 2008; 17: 336-341. doi: 10.1016/j.jse.2007.07.024

20. Mochizuki Y, Natsu K, Kashiwagi K, Yasunaga Y, Ochi M. Changes of the mineralization pattern in the subchondral bone plate of the glenoid cavity in the shoulder joints of the throwing athletes. J Shoulder Elbow Surg 2005;14: 616-619.

21. Nowak DD, Bahu MJ, Gardner TR, Dryszka MD, Levine WN, Bigliani LU, Ahmad CS. Simulation of surgical glenoid resurfacing using three-dimensional computed tomography of the arthritic glenohumeral joint: The amount of glenoid retroversion that can be corrected. J Shoulder Elbow Surg 2009; 18:680-688. doi: 10.1016/j.jse.2009.03.019

22. Nowak DD, Gardner TR, Bigliani LU, Levine WN, Ahmad CS. Interobserver and intraobserver reliability of the Walch classification in primary glenohumeral arthritis. J Shoulder Elbow Surg 2010; 19: 180-183. doi: 10.1016/j.jse.2009.08.003

23. Raphael BS, Dines JS, Warren RF, Figgie M, Craig EV, Fealy S, et al. Symptomatic glenoid loosening complicating total shoulder arthroplasty. HSS J 2010; 61: 52-56. doi: 10.1007/s11420-009-9148-1

24. Schreiber JJ, Anderson PA, Rosas HG, Buchholz AL, Au AG. Hounsfield units for assessing bone mineral density and strength: a tool for osteoporosis management. J Bone Joint Surg 2011;93: 1057-1063. doi: 10.2106/JBJS.J.00160

25. Schulz CU, Pfahler M, Anetzberger HM, Becker CR, Müller-Gerbl M, Refior HJ. The mineralization patterns at the subchondral bone plate of the glenoid cavity in healthy shoulders. J Shoulder Elbow Surg 2002;11: 174-181.

26. Sears BW, Johnston PS, Ramsey ML, Williams GR. Glenoid bone loss in primary total shoulder arthroplasty: evaluation and management." J Am Acad Orthop Surg 2012;20: 604-613. doi: 10.5435/JAAOS-20-09-604

27. Spencer EE Jr, Valdevit A, Kambic H, Brems JJ, Iannotti JP. The effect of humeral component anteversion on shoulder stability with glenoid component retroversion. J Bone Joint Surg 2005;87: 808-814. doi: 10.2106/JBJS.C.00770

28. Walch G, Badet R, Boulahia A, Khoury A. Morphologic study of glenoid glenohumeral osteoarthritis. J Arthroplasty 1999;14:756-760.

29. Walch G, Moraga C, Young A, Castellanos-Rosas J. Results of anatomic nonconstrained prosthesis in primary osteoarthritis with biconcave glenoid. J Shoulder Elbow Surg 2012; 21(11):1526-1533. doi: 10.1016/j.jse.2011.11.030.

30. Walch G, Young AA, Boileau P, Loew M, Gazielly D, Mole D. Patterns of loosening of polyethylene keeled glenoid components after shoulder arthroplasty for primary osteoarthritis: results of a multicenter study with more than five years of follow-up. J Bone Joint Surg AM 2012; 94(2):145-150. doi: 10.2106/JBJS.J.00699

31. Young AA, Walch G, Boileau P, Favard L, Gohlke, F, Loew M, et al. A multicentre study of the long-term results of using a flat-back polyethylene glenoid component in shoulder replacement for primary osteoarthritis. J Bone Joint Surg Br 2011; 93: 210-216. doi: 10.1302/0301-620X.93B2.25086.

32. Young AA, Walch G, Pape G, Gohlke F, Favard L. Secondary rotator cuff dysfunction following total shoulder arthroplasty for primary glenohumeral

osteoarthritis: results of a multicenter study with more than five years of follow-up. J Bone Joint Surg 2012; 94: 685-693. doi: 10.2106/JBJS.J.00727

33. Zeltinger J, Sherwood JK, Graham DA, Mueller R, Griffith LG. Effect of pore size and void fraction on cellular adhesion, proliferation and matrix deposition. Tissue Eng 2001; 7:557-572. doi:10.1089/107632701753213183

34. Zumstein V, Kraljević M, Müller-Gerbl M. Glenohumeral relationships: Subchondral mineralization patterns, thickness of cartilage, and radii of curvature. J Orthop Res 2013;31:1704-1707. doi: 10.1002/jor.22425

CHAPTER 3 – QUANTIFICATION OF THE POSITION, ORIENTATION, AND SURFACE AREA OF BONE LOSS IN TYPE B2 GLENOIDS

OVERVIEW: *Posterior glenoid bone loss is thought to occur due to extended subluxation of the humeral head due to muscle injury or deficiency. Current augmented glenoid components used in the management of this deficiency use a step or wedge symmetric about the superoinferior axis of the implant to account for the bone loss. For proper component positioning, bone loss must also be directed in this orientation. This chapter evaluated patients with posterior glenoid erosion (n=55) and quantified the orientation, position and surface area of bone loss. Curvature of the arthritic glenoid and humeral head were also compared.*[1]

---

1) A version of this work has been published: Knowles NK, Keener JD, Ferreira LM, Athwal GS. Quantification of the Position, Orientation and Surface Area of Bone Loss in Type B2 Glenoids. *Journal of Shoulder and Elbow Surgery* 2015; 24(4):503-510

3.1 INTRODUCTION:

Asymmetric posterior glenoid erosion in osteoarthritis with resultant retroversion presents a challenge for surgical reconstruction and the long-term survivability of standard polyethylene glenoid components.[5,7,9,10,11,22] It is theorized that the posterior erosions occur due to extended subluxation of the humeral head.[24] However, it is unknown whether osteoarthritis leads to altered kinematics and subluxation, or altered kinematics with subluxation leads to osteoarthritis. Walch et al. have classified 3 types (A, B and C) of glenohumeral alignment and bone loss associated with arthritis. Type A refers to symmetric glenoid bone loss and is sub-classified as A1 – minor or A2 – major. Type B refers to humeral head subluxation with asymmetric loading and is sub-classified as B1 – narrowed posterior joint space without glenoid erosion and B2 – posterior glenoid bony erosion with biconcavity. Type C is a dysplastic glenoid with retroversion greater than 25°.[24] The posterior erosion of type B2 glenoids is often visualized on axillary radiographs or on two-dimensional axial computed tomography (CT) images (Figure 3.1). The biconcavity, due to erosion, results in two articular facets. The posterior facet, which is created by erosion from the posteriorly subluxated humeral head, is referred to as the neoglenoid. The anterior facet, which is the remaining articular surface of the native glenoid, is referred to as the paleoglenoid.

For patients with B2 glenoids, the acquired retroversion may be managed with asymmetric “high-side” reaming, bone grafting, augmented implants or reverse shoulder arthroplasty.[4,20] Current commercially available augmented polyethylene glenoid implants consist of a step or wedge symmetric about the implants superoinferior axis that typically encompasses the entire posterior hemisphere (Figure 3.2). The goal of these implants is to minimize asymmetric “high side” reaming and therefore preserve glenoid bone stock. The orientation of the step/wedge on the augmented implants assumes that B2 glenoid bone loss is directed towards the 9 o'clock position (right shoulder). However, it has been suggested that the maximum direction of bone loss in osteoarthritic glenoids is posteroinferior, rather than directly posterior.[1] To best appreciate the complex morphology of glenoid erosions, three-dimensional (3D) computed tomography (CT)

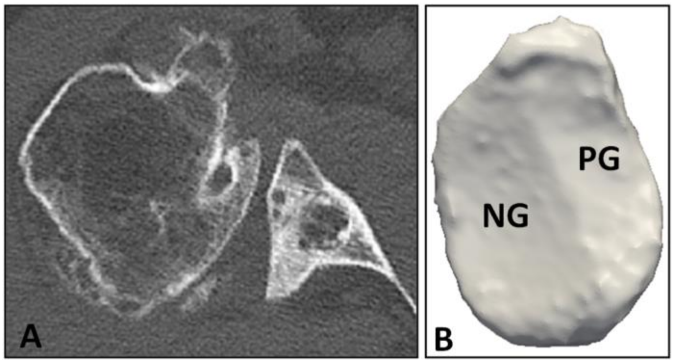

Figure 3.1: An asymmetric type B2 glenoid

A: Two-dimensional axial view CT scans of a right shoulder. **B:** A sagittal plane view of a 3D CT reconstruction with posteroinferior glenoid erosion. The neoglenoid (NG) and the paleoglenoid (PG) are depicted.

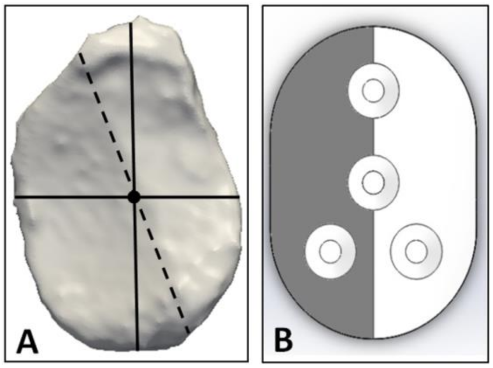

Figure 3.2: Three-dimensional sagittal plane view of a type B2 glenoid and a commercially available augmented glenoid component

A: An orthogonal coordinate system (black solid lines) was created and the center of the glenoid marked (black dot). The line-of-erosion (dashed black line) is the bony ridge that separates the neoglenoid (left side) from the paleoglenoid (right side). **B:** An illustration of a commercially available polyethylene augmented glenoid component for management of posterior erosion with a wedge or step. The augmented region (grey) is oriented with the superoinferior axis of the implant and typically encompasses the entire posterior hemisphere.

reconstructions are recommended. The literature has demonstrated that 2D CT images are inaccurate at representing the orientation and version of glenoid bone loss.[1,10,16]

The purpose of this CT-based imaging study was to evaluate the orientation and the position of posterior erosions in B2 glenoids with respect to the superoinferior axis and glenoid center. Additionally, a secondary objective was to determine if the orientation of B2 glenoid bone loss varied as a function of erosion severity, or by gender. Finally, the curvature of the B2 articular surfaces of the neoglenoid and paleoglenoid were compared to determine their associations with the curvature of the arthritic humeral head. We hypothesized that contrary to current commercially available augmented glenoid components, the line of erosion in type B2 biconcave glenoids is not symmetric about the superoinferior axis.

3.2 MATERIALS AND METHODS:

3.2.1 Patients

Seventy-four patients from two institutions who had undergone or were awaiting shoulder replacement surgery between 2007 and 2014 for osteoarthritis with a type B2 glenoid were evaluated by one of two experienced shoulder surgeons (G.S.A & J.D.K) using a clinically validated method.[19] Inclusion criteria were: primary glenohumeral osteoarthritis. Exclusion criteria were: inflammatory arthritis, post-capsulorraphy arthritis, post-traumatic arthritis, rotator cuff tear arthropathy, revision arthroplasty scenarios. Nineteen patients were excluded for incomplete or unsegmentable CT scans leaving 55 cases for analysis. The mean age of the cohort was 63±10 years (range, 38-84 years) and there were 39 male patients (71%). Computed tomography scans in digital imaging and communications in medicine (DICOM) format, scanned using multi-slice scanners with standard clinical settings (120 to 140 kVp, 512x512 resolution) were obtained for each patient.

3.2.2 Model Creation and Measurements

The DICOM files from each CT scan were uploaded to a medical imaging software program (Mimics® V. 16.0, Materialize, Leuven, BE). Standard segmentation techniques were used to separate the humerus from the glenoid. Following segmentation, three-dimensional (3D) reconstructions of each patient’s scapula and proximal humerus were created as stereolithography (STL) files. Bryce et al.[2] previously validated the accuracy of this software for anatomic measurements of the scapula, by comparing independent observers’ measurements made on cadaveric specimens to the same measurements made on their 3D reconstructions.

Three-dimensional point coordinates were extracted from each patient's 3D reconstructed glenoid using the built-in medCAD module. Using a method similar to De Wilde et al.[6], an orthogonal coordinate system was defined on the glenoid face by the most superior and inferior points on the glenoid rim. A perpendicular bi-sector at the midpoint of this axis was used to determine the center of the glenoid (Figure 3.2).

The original DICOM images were re-sliced in Mimics® sagittal to the glenoid to ensure accurate measurements, unaffected by retroversion angle or patient positioning. Custom code was developed in Matlab (Mathworks, Natick, MA, USA) to transform the 3D point coordinates to the new 2D sagittal plane, which represents the intra-operative visual perspective referred to as the clock face. Ten points were extracted along the ridge of bone that separates the paleoglenoid (anterior facet) from the neoglenoid (posterior facet) on the glenoid articular surface. This ridge of bone was termed the line-of-erosion. The ten points on the line-of-erosion were used to determine a linear best fit line, which was used to define the position and orientation of bone loss measurements (Figure 3.2). The angle between the line-of-erosion and the superoinferior axis of the glenoid defined the orientation angle of the posterior bone loss. The shortest perpendicular distance between the center of the glenoid and the linear best fit line that represented the line-of-erosion determined the relative position of the bone loss on the glenoid face.

To further characterize the line-of-erosion in terms of its curvature, a circle was fit to the ten points selected along the line-of-erosion. A new set of ten points were calculated on the arc of the circle fit between the most superior and inferior edges of the glenoid face (Figure 3.3). This circle fit arc represented the curvature of the line-of-erosion and was used to classify the erosions as curved or non-curved (straight). For all patients, the chord length (c) was calculated from the most superior and inferior circle fit erosion points. The perpendicular distance from the bisector of the chord to the center of the circle was calculated. This value was subtracted from the radius of the circle (r), to determine the sagitta (s) from the chord midpoint to the circle perimeter. The aspect ratio (s/c) of the resulting minor segment was used to quantify patients as having a curved or non-curved (straight) line-of-erosion. Glenoids with an aspect ratio greater than 0.1 (i.e., greater than 10%) were classified as curved. This was confirmed visually.

3.2.3 Surface Area and Sphere Fitting

Each 3D reconstructed scapula was exported from Mimics® into 3-Matic® (V. 8.0, Materialize, Leuven, BE) along with the ten points defining the line-of-erosion. Each scapula was cropped to isolate only the glenoid articular surface. The neoglenoid and the paleoglenoid articular surfaces were highlighted using the built-in surface marking tools. This surface marking allowed calculation of the surface area of each selected region and the entire glenoid. For each patient, the surface area of the neoglenoid articular facet was determined as a percentage of the entire glenoid surface area (neoglenoid + paleoglenoid). Unfortunately, there is no literature available to classify the magnitude of posterior erosion in a type B2 glenoid. As such, to determine if the magnitude of posterior bone loss had an effect on the angular orientation, we arbitrarily divided the entire cohort in to three sub-groups based on the surface area occupied by the neoglenoid as compared to the entire glenoid. The subgroups were defined as: mild erosion: 0 - 33%; moderate erosion: 34 - 66%; and severe erosion: > 66%.

In addition to glenoid data, three-dimensional point coordinates were also collected on the neo-articulation of the humeral head. The neo-articulation was assumed

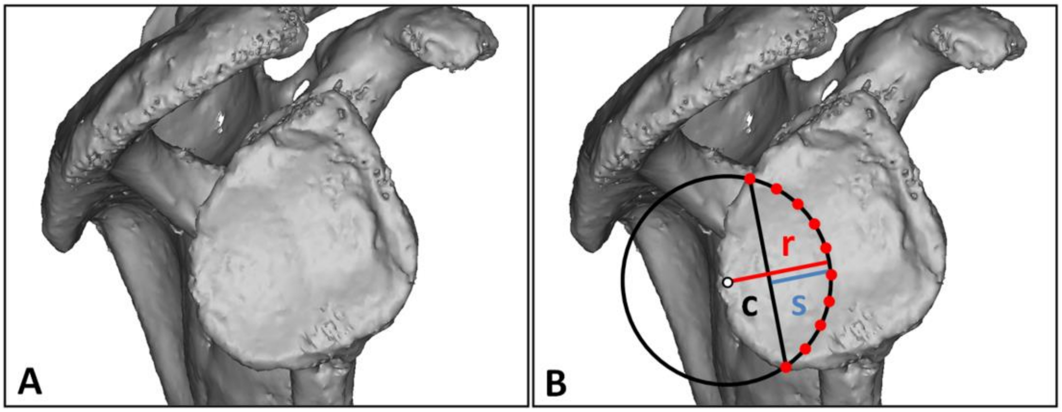

Figure 3.3: A 3D sagittal plane view of a B2 glenoid erosion pattern exhibiting a curved line of erosion

A: The line-of-erosion, separating the neoglenoid from the paleoglenoid, was curved in 19 of the 55 glenoids. **B:** To quantify curved erosions, a circle was fit to points along the erosion. A chord length (c) was determined from the most superior and inferior circle fit points. The distance saggita (s) was calculated from the circle radius (r) and the chord midpoint. Glenoids with an aspect ratio > 0.1 (i.e., greater than 10%) were classified as curved.

to be the visible smooth articular surface of the humeral head free from osteophyte formation (Figure 3.4 A&B). A least-squares sphere fit to the 3D points was calculated with custom code in Matlab®[13] to determine humeral head articular surface radius. Points were also collected on the surface of the neoglenoid and paleoglenoid, and a least-squares sphere fit was calculated for each set of points (Figure 3.4 C&D) to determine their radii. During articular data point acquisition, areas of calcified labrum and osteophytes were excluded.

3.2.4 Statistical Analysis

Statistical analysis (SigmaPlot V. 11.0, Systat Software Inc., Germany) was performed to determine the difference between orientation and position with respect to the supero-inferior axis and the center point of the glenoid, respectively, using a Mann-Whitney Rank Sum Test for all patients and separately by sub-group. Differences between males and females of the percentage of glenoid surface area occupied by the neoglenoid, and differences in orientation and position of the line-of-erosion, were determined using t-tests. Differences between the neo-articulation of the humeral head and the neoglenoid and paleoglenoid were determined separately using Paired t-tests or Wilcoxon Signed Rank Tests for all patients and within each sub-group.

Inter-observer reliability was performed for orientation and position measurements with respect to the orthogonal coordinate system by two independent observers (N.K.K and G.S.A.). Inter-observer reliability was also performed to validate the orthogonal coordinate system by calculating the Euclidean distance from the origin to the superior and inferior points on the glenoid surface. Measurements were repeated by one observer (N.K.K) approximately one month apart to assess intra-observer reliability for orientation, position and orthogonal coordinate system measurements. Intraclass correlation coefficients (ICC) with a two-way random effects model and absolute agreement was used.[21] Classifications for ICC results were interpreted according to Fleiss

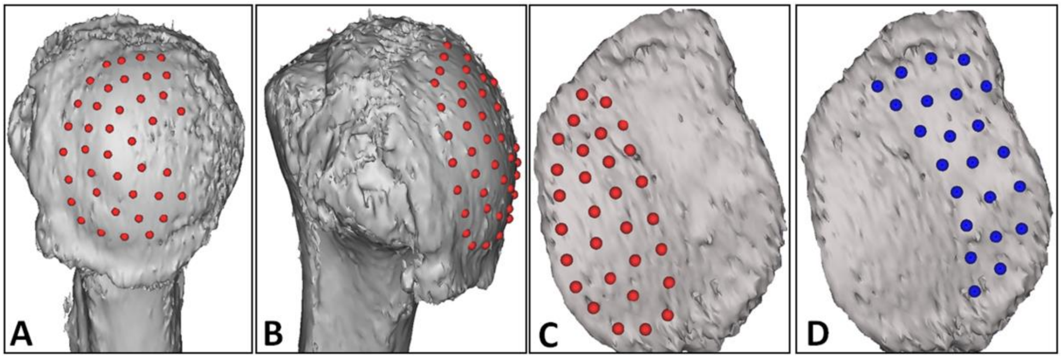

Figure 3.4: Three-dimensional point coordinates (red and blue dots) on the humerus andglenoid

A 3D model of the proximal humerus from the **A:** sagittal and **B:** coronal plane views with the neo-articulation marked with points. Note that the osteophytes along the periphery of the articulation have not been selected. **C:** A sagittal view of a type B glenoid with the neoglenoid and **D:** paleoglenoid selected.

(1981)[8] and Cicchetti and Sparrow (1981)[3] as poor (ICC < 0.40), fair (ICC = 0.40 – 0.59), good (ICC = 0.60 – 0.74), and excellent (ICC > 0.74).[3,8]

3.3 RESULTS

3.3.1 Orientation and Position of the Line-of-Erosion

There was a significant difference between the mean orientation angle (28 ± 11°) of the posterior glenoid bone loss line-of-erosion and the superoinferior axis ($p < 0.001$); which resulted in the average erosion for the entire cohort being directed towards the 8 o'clock position in a right shoulder (Figure 3.5). There were also significant differences in orientation angles between each sub-group compared to the superoinferior axis: mild (30 ± 14°) ($p < 0.001$); moderate (27 ± 10°) ($p < 0.001$); and severe (33 ± 14°) ($p = 0.029$) (Figure 3.6).

There was a significant difference between the position of the line-of-erosion and the center of the glenoid ($p < 0.001$), with the line-of-erosion starting a mean of 1.6 ± 3.4 mm posterior to the glenoid center point (Figure 3.5). There were also significant differences in the position of the line-of-erosion between each sub-group: mild (5.6 ± 3.0 mm posterior) ($p < 0.001$); moderate (0.9 ± 2.2 mm posterior) ($p = 0.012$); and severe (3.5 ± 1.5 mm anterior) ($p = 0.029$) (Figure 3.6). Complete measurements of the orientation and position of the line-of-erosion for each sub-group are presented in Table 3.1.

There was no difference between the orientation angle of the line-of-erosion in male (28 ± 10°) compared to female patients (27 ± 14°) ($p = 0.772$). There was also no significant difference in the position of the line-of-erosion in male patients (1.4 ± 3.3 mm posterior) compared to female patients (2.2 ± 3.5 mm posterior) ($p = 0.447$). Complete measurements by gender are presented in Table 3.2.

Inter-observer reliability was excellent for both the superior (ICC = 0.997, 95% CI = 0.990-0.999) and inferior points (ICC = 0.996, 95% CI = 0.986-0.999). Intra-

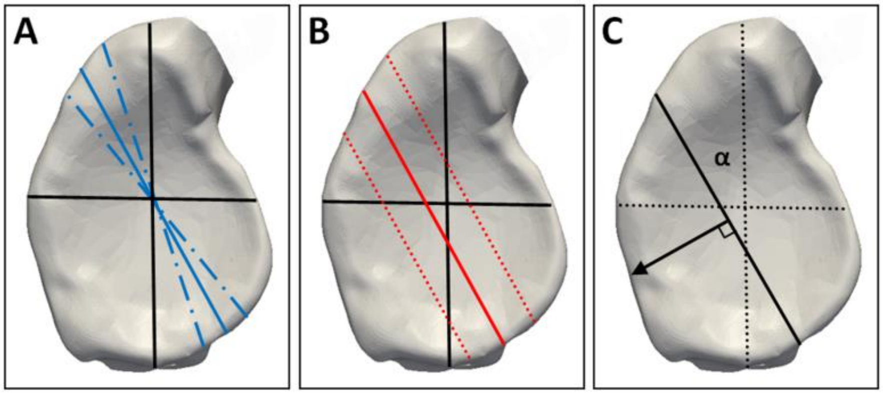

Figure 3.5: Posterior erosion patterns for 55 patients with asymmetric (B2) glenoids (right shoulder shown)

A: Mean orientation angle (solid blue line) and one standard deviation (dashed blue line). **B**: Mean position (solid red line) and one standard deviation (dotted red line). **C:** The mean erosion line (black solid line) is directed 28° ± 11° (α) from the superoinferior axis of the glenoid, with posterior erosion being directed perpendicular towards the 8 o'clock position (black arrow).

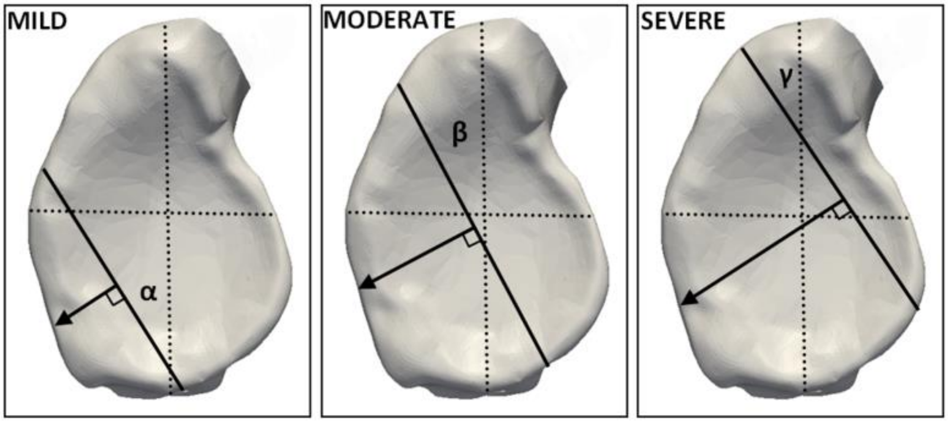

Figure 3.6: Orientation and position of posterior erosion in mild (n=12), moderate (n = 39), and severe (n = 4) asymmetric (B2) glenoids

Angles with respect to the superoinferior axis are: α = 30 ± 14 °; β = 27 ± 10°; γ = 33 ± 14°, with maximum erosion directed towards the 8 o'clock position.

Table 3.1: Demographic and anatomic features of mild, moderate and severe type B2 glenoids with posterior erosion

Measurement	All (n=55)	Mild Erosion (n=12)	Moderate Erosion (n=39)	Severe Erosion (n=4)
Position w.r.t Glenoid Center (mm)	-1.6 ± 3.4 (-11.8 – 5.0)	-5.6 ± 3.0 (-11.8 – -2.5)	-0.92 ± 2.2 (-6.7 – 3.0)	3.5 ± 1.5 (1.4 – 5.0)
Orientation Angle w.r.t Superoinferior Axis (°)	28 ± 11 (2 – 54)	30 ± 14 (2 – 54)	27 ± 10 (2 – 52)	33 ± 14 (20 – 53)
Age (years)	63 ± 10 (38 – 84)	61 ± 11 (38 – 75)	63 ± 10 (42 – 84)	66 ± 6 (59 – 73)
Humeral Head Radius (Neo-Articulation) (mm)	31.9 ± 5.7 (22.8 – 53.2)	32.9 ± 8.9 (22.8 – 53.2)	31.6 ± 4.2 (24.7 – 43.1)	32.1 ± 8.2 (23.5 – 43.3)
Neoglenoid Radius (mm)	36.8 ± 7.7 (12.9 – 53.2)	35.4 ± 11.6 (12.9 – 52.9)	37.5 ± 6.5 (27.3 – 53.2)	34.3 ± 5.4 (27.5 – 39.9)
Paleoglenoid Radius (mm)	34.2 ± 6.6 (15.0 – 49.8)	33.1 ± 4.9 (21.8 – 39.7)	34.8 ± 6.1 (20.8 – 49.8)	31.1 ± 14.4 (15.0 – 44.72)
Total Glenoid Surface Area (mm^2)	1720 ± 367 (1110 – 2840)	1667 ± 357 (1193 – 2240)	1717 ± 326 (1130 – 2410)	1943 ± 745 (1110 – 2840)
Neoglenoid Surface Area (mm^2)	763 ± 296 (234 – 1876)	461 ± 137 (234 – 668)	799 ± 195 (490 – 1390)	1335 ± 452 (822 – 1876)
Paleoglenoid Surface Area (mm^2)	957 ± 276 (288 – 1747)	1205 ± 294 (819 – 1747)	918 ± 209 (576 – 1286)	608 ± 293 (288 – 964)
Values are mean ± SD (range); Positive (+) values are anterior, negative (-) values are posterior; w.r.t - with respect to				

Table 3.2: Demographic and anatomic features of male and female patients with type B2 posterior glenoid erosion

Measurement	Female (n=16)	Male (n=39)	p-value
Position w.r.t Glenoid Center (mm)	-2.2 ± 3.5 (-10.8 – 5.0)	-1.4 ± 3.3 (-11.8 – 4.0)	0.447
Orientation Angle w.r.t Superoinferior Axis (°)	27 ± 14 (2 – 54)	28 ± 10 (2 – 54)	0.772
Age (years)	69 ± 6 (60 – 84)	60 ± 10 (38 – 76)	<0.001
Humeral Head Radius (Neo-Articulation) (mm)	27.6 ± 3.7 (22.8 – 35.1)	33.7 ± 5.5 (24.9 – 53.2)	<0.001
Neoglenoid Radius (mm)	32.2 ±8.7 (12.9 – 53.2)	38.7 ± 6.5 (28.5 – 52.9)	0.004
Paleoglenoid Radius (mm)	30.7 ± 6.4 (15.0 – 42.3)	35.6 ± 6.3 (20.8 – 49.8)	0.011
Curved Erosions (% of patients)	25%	38%	-
Values are mean ± SD (range); Positive (+) values are anterior, negative (-) values are posterior; w.r.t - with respect to			

observer reliability was also excellent for both the superior (ICC = 0.997, 95% CI = 0.992-0.999) and inferior points (ICC = 0.999, 95% CI = 0.998-1.000).

Inter-observer reliability was excellent in position (ICC = 0.878, 95% CI = 0.120 -0.987) and orientation (ICC = 0.819, 95% CI = -0.450 - 0.980) of the line-of-erosion compared to the center of the glenoid and superoinferior axis, respectively. Intra-observer reliability was excellent for position (ICC = 0.795, 95% CI = 0.486-0.926) and good for orientation (ICC = 0.711, 95% CI = 0.333-0.893), respectively.

3.3.2 Surface Area

The mean surface area for the neoglenoid in the entire cohort was 763 ± 296 mm^2, the paleoglenoid was 957 ± 276 mm^2, and the total glenoid surface area for type B2 erosions was 1720 ± 367 mm^2. These values indicate the neoglenoid occupied a mean of 44 ± 12% of the total glenoid area in the complete study cohort. In females, the mean total surface area of the glenoid was 1391 ± 271 mm^2 and in males was 1855 ± 314 mm^2. The mean surface area of the neoglenoid was 584 ± 201 mm^2 for females and 837 ± 299 mm^2 for males and for the paleoglenoid, 807 ± 249 mm^2 for females and 1018 ± 266 mm^2 for males. These values correspond to the neoglenoid occupying 42 ± 14% of the total glenoid in females and 45 ± 12% in males, which were not significantly different ($p=0.479$). Surface area measurements by sub-group are presented in Table 3.1 and 3.2.

3.3.3 Radius Measurements

For the entire cohort, the mean radius of the humeral head neo-articulation was 32 ± 6 mm, for the neoglenoid was 37 ± 8 mm, and for the paleoglenoid was 34 ± 7 mm. For all patients, the radius of the humeral head neo-articulation was significantly less than that of the neoglenoid ($p < 0.001$) and the paleoglenoid ($p = 0.009$). Additionally, the radius of the neoglenoid was significantly greater than the paleoglenoid ($p = 0.012$). The humeral head neo-articulation, neoglenoid and paleoglenoid radii are presented in Table 3.1.

For male patients, there was a significant difference between the radius of the humeral head neo-articulation (34 ± 5 mm) and the neoglenoid (39 ± 6 mm) ($p < 0.001$), but no significant difference between the humeral head and the paleoglenoid (36 ± 6 mm) ($p = 0.126$). Similarly for female patients, there was a significant difference between the radius of the humeral head neo-articulation (28 ± 4 mm) and the neoglenoid (32 ± 9 mm) ($p = 0.028$), but no significant difference between the humeral head and the paleoglenoid (31 ± 6 mm) ($p = 0.063$). In 19 patients (35%), the circle fit method corresponded to a curved erosion line rather than a straight line. For these patients, the mean circle fit radius of the line-of-erosion was 27 ± 7 mm (range: 15 to 38 mm) and the mean aspect ratio (s/c) was 0.16 ± 0.05 (range: 0.10 to 0.28).

3.4 DISCUSSION:

The results of this study indicate that bone loss in type B2 glenoids is not isolated to the posterior hemisphere of the glenoid and is not symmetrically oriented towards 9 o’clock as presently available augmented glenoid implants are designed. On average, the orientation of type B2 erosions was directed towards the 8 o’clock position (right shoulder) in the posteroinferior quadrant of the glenoid. The mean line-of-erosion was directed 28° from the superoinferior axis, which resulted in the line-of-erosion starting at 11 o’clock and directed towards 5 o'clock in a right shoulder (Figure 3.4). Surgeons managing patients with type B2 bone loss should be aware of this orientation, especially if considering bonegrafting or commercially available symmetrically oriented augmented glenoid components. Additionally, the direction of glenoid bone loss in B2 cases varied as a function of magnitude, with the orientation of the line-of-erosion being statistically different from the superoinferior axis for mild (30°), moderate (27°), and severe (33°) erosions. Although these differences were found to be significant, we do not believe they are clinically substantial when using present day manual glenoid orientation and preparation methods.

Terrier et al.[23] reported on 86 patients with type A, B and C arthritic glenoids to determine the glenoid version. They found that the orientation of the maximal version in osteoarthritis cases was usually posterior, but also extended to the posterosuperior quadrant in 35% of cases and to the posteroinferior quadrant in only 6% of cases. The variations in these results as compared to ours, are likely due to the small number of type B2 cases (11 shoulders) examined by Terrier et al. Recently, Beuckelaers et al.[1] evaluated the maximum amount of erosion in type B2 glenoids as related to the greatest perpendicular distance from the native sagittal glenoid plane to the neoglenoid articular surface. They found that the maximum depth of erosion occurred between the 8 and 9 o'clock positions, which are similar to our results. One interesting difference between our cohort and that of Beuckelaers et al, is that we had 39 (71%) male patients, while Beuckelaers et al. had only 16 males (33%).

In our study cohort, we identified 19 of 55 patients (35%) with B2 glenoids that had a curved line-of-erosion, similar to that shown in Figure 3.3. Before analyzing our data, we hypothesized that this may indicate a more constrained glenohumeral relationship. We theorized that the posteriorly subluxated humeral head was eroding the glenoid via rotation rather than translation, articulating only with the neoglenoid. Therefore, we believed the radii of the humeral head and neoglenoid would be closely matched. Although this seemed logical, we were surprised when the data indicated a significant difference between the radius of the humeral head and the neoglenoid. In fact, the radius of the humeral head more closely approximated the paleoglenoid radius than the neoglenoid radius. This certainly indicates that for glenoid erosions, there are multiple and possibly unknown variables that contribute to the morphology or orientation of the bone loss. As more than a third of the patients in this study had a curved line of erosion, it warrants further investigation. In cases where augmented glenoid components are utilized, curved erosions may require additional bone removal from the superior and inferior aspects of the glenoid to facilitate the implantation of the wedge or step augment.

The radii of the corresponding arthritic humeral heads reported in this study were found to be larger than previous studies.[11,26] This result, however, is not surprising as we measured the neo-articulation of the humerus, defined by the smooth articular convexity associated with increased subchondral mineralization. Although osteophytes were visible on the peripheral margins of the native humeral head, they were not selected for radius determination. The results we obtained for the radius of the neoglenoid and paleoglenoid closely matched the glenoid curvature values from similar studies using best-fit spheres.[18,25]

The results of this study are perhaps most important for surgeons managing type B2 posterior erosions with augmented glenoid components. If the orientation of the erosion is incorrectly assumed to be symmetric about the glenoids superoinferior axis, the implant may be malrotated during positioning. Additionally, axisymmetric augmented glenoid components may require additional extra bone removal in the posterosuperior quadrant to correctly align the implant. With axisymmetric posterior hemispheric augments, further anterior high-side reaming may be required as moderate sized B2 erosions typically obliquely progress in to the anteroinferior quadrant of the glenoid. Furthermore, the results indicate that a large proportion of our cohort has a neoglenoid that occupies less than 50% of the total glenoid surface area. In these circumstances, surgical management with an axisymmetric hemispheric augmented implant would require additional bone removal. At present, there is little consensus on the proper glenoid reaming technique and amount in B2 deformities resulting in large surgeon variability.[14] Therefore, reaming and subsequent bone removal should be thoughtfully considered and templated, as excess bone removal may reduce the quality of the remaining glenoid bone, leading to potentially compromised implant stability.

A strength of this study is the method used to create the orthogonal glenoid coordinate system to determine the glenoid center. This coordinate system method can be applied intra-operatively during glenoid implantation during total shoulder arthroplasty. Contrary to previously described methods that use points on the glenoid surface as well as the scapular spine[15-17,27], this method allows for clinically utilizable landmarks. Another strength of this study is the larger cohort size of isolated B2 glenoids, allowing for more robust conclusions.

The limitations of this study are that the results are only applicable to type B2 erosion patterns. Also, once we divide the cohort based on severity, there were only 12 cases in the mild sub-group and 4 in the severe sub-group, potentially weakening the generalizability of our results.

1. Beuckelaers E, Jacxsens M, Van Tongel A, De Wilde LF. Three-dimensional computed tomography scan evaluation of the pattern of erosion in type B glenoids. J Shoulder Elbow Surg 2014; 23:109-116 doi: 10.1016/j.jse.2013.04.009

2. Bryce CD, Pennypacker JL, Kulkami N, Paul EM, Hollenbeak, Masher TJ, et. al. Validation of three-dimensional models of in situ scapulae. J Shoulder Elbow Surg 2008; 17:825-832. doi: 10.1016/j.jse.2008.01.141

3. Cicchetti DV, and Sparrow SS. Developing criteria for establishing the interrater reliability of specific items in a given inventory. Am J Ment Defic 1981; 86:127-137.

4. Clavert P, Millett PJ, Warner JJ. Glenoid resurfacing: What are the limits to asymmetric reaming for posterior erosion? J Shoulder Elbow Surg. 2007; 16: 843-848.doi: 10.1016/j.jse.2007.03.015

5. Denard PJ, Walch G. Current concepts in the surgical management of primary glenohumeral arthritis with a biconcave glenoid. J Shoulder Elbow Surg 2013; 11:1589-1598. doi: 10.1016/j.jse.2013.06.017

6. De Wilde LF, Berghs BM, Audenaert, Sys G, Van Maele GO, Barbaix. About the variability of the shape of the glenoid cavity. Surg Radiol Anat 2004; 26:54-59. doi:10.1007/s00276-003-0167-1

7. Farron A, Terrier A, Büchler P. Risks of loosening of a prosthetic glenoid implanted in retroversion. J Shoulder Elbow Surg 2006; 15: 521-526. doi: 10.1016/j.jse.2005.10.003

8. Fleiss JL. Statistical Methods for Rates and Proportions. 1981; 2nd. Edition. New York:Wiley.

9. Friedman RJ, Hawthorn KB, Genez BM. The use of computerized tomography in the measurement of glenoid version. J Shoulder Elbow Surg 1992;74:1032-1037.

10. Ganapathi A, McCarron JA, Chen X, Iannotti JP. Predicting normal glenoid version from the pathologic scapula: a comparison of 4 methods in 2-and 3-dimensional models. J Shoulder Elbow Surg 2011; 20: 234-244. doi: 10.1016/j.jse.2010.05.024

11. Gebhart JJ, Miniaci A, Fening SD. Predictive anthropometric measurements for humeral head curvature. J Shoulder Elbow Surg 2013; 22(6): 842-847. doi: 10.1016/j.jse.2012.08.020

12. Hsu JE, Ricchetti ET, Huffman GR, Iannotti JP, Glaser DL. Addressing glenoid bone deficiency and asymmetric posterior erosion in shoulder arthroplasty. J Shoulder Elbow Surg 2013; 22(9):1298-1308. doi: 10.1016/j.jse.2013.04.014

13. Jennings A. Sphere Fit (least squared) (software). Retrieved from Matlab Central File Exchange; 2011.

14. Karelse A, Leuridan S, Van Tongel AV, Piepers IM, Debeer P, De Wilde LF. A glenoid reaming study: how accurate are current reaming techniques? J Shoulder Elbow Surg 2014; In-Press. doi: 10.1016/j.jse.2013.11.023

15. Kwon YW, Powell KA, Yum JK, Brems JJ, Iannotti JP. Use of three-dimensional computed tomography for the analysis of the glenoid anatomy. J Shoulder Elbow Surg 2005; 14:85-90. doi: 10.1016/j.jse.2004.04.011

16. Lewis GS, Armstrong AD. Glenoid spherical orientation and version. J Shoulder Elbow Surg; 20:3-11. doi: 10.1016/j.jse.2010.05.012

17. Lewis GS, Bryce CD, Davison AC, Hollenbeak CS, Piazza SJ, Armstrong AD. Location of the optimized centerline of the glenoid vault: a comparison of two operative techniques with use of three-dimensional computer modeling. J Bone Joint Surg Am 2010; 92:1188-1194. doi: 10.2106/JBJS.I.00131

18. Moineau G, Levigne C, Boileau P, Young A, Walch G. Three-dimensional measurement method of arthritic glenoid cavity morphology: Feasibility and reproducibility. Orthop Traumatol Surg Res 2012; 98S:S139-S145. doi: 10.1016/j.otsr.2012.06.007

19. Nowak DD, Gardner TR, Bigliani LU, Levine WN, Ahmad CS. Interobserver and intraobserver reliability of the Walch classification in primary glenohumeral arthritis. J Shoulder Elbow Surg 2010; 19: 180-183. doi:10.1016/j.jse.2009.08.003

20. Sears BW, Johnston PS, Ramsey ML, Williams GR. Glenoid bone loss in primary totalshoulder arthroplasty: evaluation and management. J Am Acad Orthop Surg 2012;20: 604-613. doi: 10.5435/JAAOS-20-09-604

21. Shrout PE, Fleiss JL. Intraclass Correlations: Uses in Assessing Rater Reliability. Pschol Bull 1979; 86:420-428.

22. Spencer EE Jr, Valdevit A, Kambic H, Brems JJ, Iannotti JP. The effect of humeral component anteversion on shoulder stability with glenoid component retroversion. J Bone Joint Surg 2005;87: 808-814. doi: 10.2106/JBJS.C.00770

23. Terrier A, Ston J, Larrea X, Farron A. Measurements of three-dimensional glenoid erosion when planning prosthetic replacement of osteoarthritic shoulders. Bone Joint J 2014; 96-B:513-518. doi: 10.1302/0301-620X.96B4.32641

24. Walch G, Badet R, Boulahia A, Khoury A. Morphologic study of the glenoid in primary glenohumeral osteoarthritis. J Arthroplasty 1999;14:756-60. doi: 10.1016/S0883-5403(99)90232-2

25. Walch G, Mesiha M, Boileau P, Edwards TB, Levigne C, Moineau G, Young A. Three-dimensional assessment of the dimensions of the osteoarthritic glenoid. Bone Joint J 2013; 95-B:1377-1382. doi:10.1302/0301-620X.95B10.

26. Youderian AR, Ricchetti ET, Drews M, Iannotti JP. Determination of humeral head size in anatomic shoulder replacement for glenohumeral osteoarthritis. J Shoulder Elbow Surg 2013; S1058-2746(13)00472-2. doi: 10.1016/j.jse.2013.09.005

27. Verstraeten TRGM, Deschepper E, Jacxsens M, Walravens S, De Coninck B. Pouliart N, De Wilde LF. Operative guidelines for the reconstruction of the native glenoid plane: an anatomic three-dimensional computed tomography-scan reconstruction study. J Shoulder Elbow Surg 2012; 21:1565-1572. doi: 10.1016/j.jse.2011.10.030

CHAPTER 4 –AUGMENTED GLENOID COMPONENT DESIGNS FOR TYPE B2 EROSIONS: A COMPUTATIONAL COMPARISON BY VOLUME OF BONE REMOVAL, AND QUALITY OF REMAINING BONE

OVERVIEW: *This chapter evaluated the bone removal and underlying bone density and porosity required for optimal placement of current augmented glenoid components. Three designs of augmented glenoid components were compared: posterior-wedge, posterior-step, and full-wedge. Each implant was virtually placed on three-dimensional scapula models by an experienced shoulder surgeon in two clinically relevant positions in a cohort of 16 patients (8 male). The implant designs were compared on the total and normalized volume of bone removal and quality of bone in anterior and posterior hemispheres directly below each implant.*[1]

---

1) A version of this work has been published: Knowles NK, Ferreira LM, Athwal GS. Augmented Glenoid Component Designs for Type B2 Erosions: A Computational Comparison by Volume of Bone Removal, and Quality of Remaining Bone. *Journal of Shoulder and Elbow Surgery*, E-Pub Ahead of Print. Available: Jan. 31, 2015

4.1 INTRODUCTION:

Excessive acquired glenoid retroversion, as seen in patients with posterior bone loss due to advanced osteoarthritis, is poorly understood and is challenging to manage with standard glenoid components.[4,8,9,17] This erosive bone loss pattern has been classified as type B2 by Walch et al.[20] Several treatment options exist for the management of type B2 erosions, however, none have demonstrated clinical superiority. The surgical options available to manage B2 glenoids include, hemiarthroplasty, eccentric reaming and hemiarthroplasty, eccentric reaming and standard total shoulder arthroplasty, structural glenoid bone grafting, augmented glenoid components, and reverse total shoulder arthroplasty.

Presently, several implant manufacturers are releasing or have commercially released augmented glenoid components to account for the posterior bone loss. These implants are typically designed with a posteriorly oriented step or wedge, which assumes the maximum glenoid erosion is oriented 90 degrees to the implant's superior-inferior axis. Although these implants are intended to conserve subarticular bone, it has been suggested that B2 bone loss is not oriented purely in the posterior direction. Recent literature has demonstrated that the average B2 glenoid has bone loss in the posteroinferior quadrant is directed towards the 8 o'clock position (right shoulder).[1,19] This pattern of bone loss may not be completely accounted for by the axisymmetric posterior augments of the available implant designs. Consequently, this may result in increased bone removal in the posterosuperior quadrant or possibly malrotation of components in order to facilitate full backside seating. Additionally, the distribution of subarticular bone density in B2 glenoids is characteristically different as compared to symmetrically eroded glenoids.[10,18] Bone density is greatest in the subarticular bone of the posterior eroded glenoid facet, or "neoglenoid" as termed by Walch et al.[5,21] As such, the neoglenoid contains thicker, denser and less porous bone. Unfortunately, this good quality bone in the neoglenoid is found in the subarticular zone only and diminishes with greater depth.[10,18] As such, augmented implant preparation techniques that involve removal of substantial amounts of the neoglenoid bone may leave behind less dense bone with greater porosity to support the implant for its lifespan.

The purpose of this anatomic computational modeling study was to compare the volume of glenoid bone removal required to implant three different designs of posterior augmented components for the management of type B2 erosions. Additionally, we wanted to compare the quality of the remaining glenoid bone directly below the various implants by assessing residual bone density and porosity as indicators of implant stability and fixation.

4.2 MATERIALS AND METHODS:

4.2.1 Augmented Implant Models

Three augmented glenoid component designs - posterior-step, full-wedge, and posterior-wedge, were created as computer models using computer-aided design (CAD) software (Solidworks, Dessaults Systemes, USA) (Figure 4.1). These implant CAD models were created according to the precise dimensions and sizes of augmented implant designs. The posterior-step implant (Steptech, Depuy, Warsaw, IN) consisted of five sizes based on the bearing diameter (40, 44, 48, 52 and 56 mm), and step height (3, 5 and 7 mm), resulting in fifteen right and fifteen left implant models. The full-wedge implants (Equinoxe, Exactech, FL) were created in small, medium, large and extra-large sizes with wedge angles of 8°, 12° and 16°. These implants are anatomically shaped, with left and right models, resulting in a total of twenty-four implants. Finally, the posterior-wedge implant models (Posterior Augmented Glenoid, Tornier, Bloomington, MN) consisted of small, medium, large and extra-large sizes, with wedge angles of 15°, 25°, and 35°. These implants were also anatomical and were produced in left and right models for a total of twenty-four implants. Fixation features (i.e. pegs or keels) were not included in the CAD models, in order to avoid confounding bias in bone removal due to fixation designs.

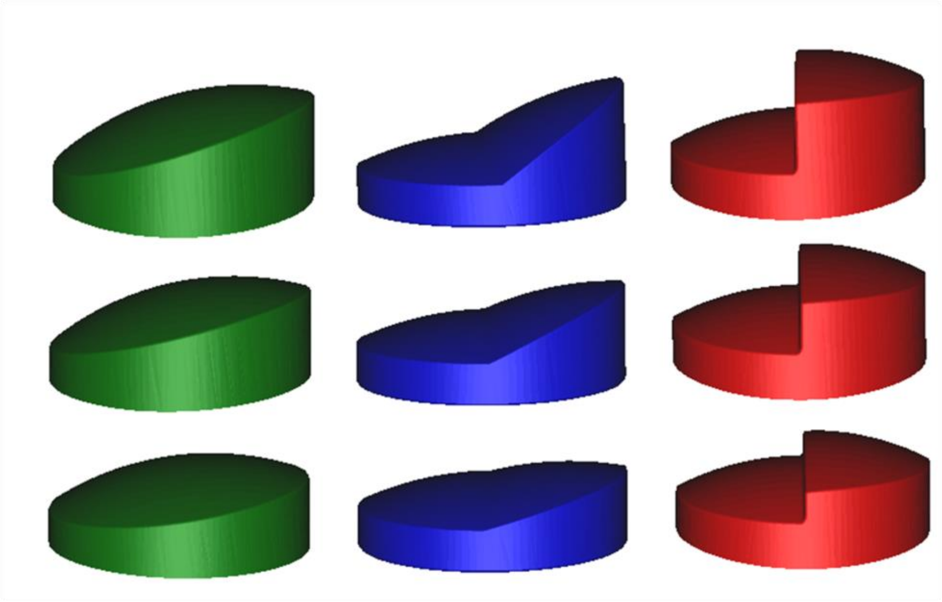

Figure 4.1: CAD models of the three designs of augmented implant compared in this study to reconstruct B2 erosions

The full-wedge implants (green) have wedge angles of 8°, 12° and 16°. The posterior-wedge implants (blue) have wedge angles of 15°, 25°, and 35°. The posterior-step implants (red) have step heights of 3, 5 and 7 mm.

4.2.2 Glenoid Models and Virtual Implantation

In order to test the augmented glenoid component designs in a clinically important manner, the implants were virtually implanted in a study cohort of 16 patients (age: 66 ± 11 years, range: 42-84, 8 male) who were classified as type B2 by a fellowship trained shoulder surgeon (G.S.A) using a clinically validated method.[12] Pre-operative computed tomography (CT) scans in digital imaging and communications in medicine (DICOM) format were acquired using multi-slice CT scanners with standard clinical settings (120 to 140 kVp, 512x512 resolution). A three-dimensional (3D) virtual model of each patient's scapula was created in medical imaging software (Mimics® V. 17.0, Materialize, Leuven, BE) from the DICOM data using standard segmentation techniques. A minimum threshold of 200 Hounsfield Units (HU) was used to preserve both cancellous and cortical bone in the model geometry.[2,10]

Osseous landmarks were used to define the coronal scapular plane and the 0° version plane, as previously described.[6,7,11,14,16] A plane was also created to define the 3D version of the neoglenoid (Figure 4.2), termed the neo-version plane, using a method similar to the intermediate plane[1], and the version plane.[14,16] The neo-version plane was defined by three-points - one point was placed on the inferior aspect of the ridge of bone separating the neoglenoid from the paleoglenoid, a second point was placed on the superior aspect of the ridge of bone separating the neoglenoid from the paleoglenoid, and a third was placed at the most medial point of the posterior rim of the eroded glenoid (Figure 4.2). The neo-version plane allowed for determination of the neoglenoid angle relative to the 0° version plane, which was used to position the implant in two versions (0° and 10°) and assisted with step height and wedge angle determination, as per the individual implant designs (Table 4.1).

Each patient's 3D model and the accompanying planes were separately imported into 3-Matic® (V. 9.0, Materialize, Leuven, BE) as stereolithography (STL) files for implant placement. Implant positioning was performed by a fellowship trained shoulder surgeon (G.S.A) as previously described by Sabesan et al.[14,16] Each individual implant was aligned with the 0° version plane and the implant size was selected to completely

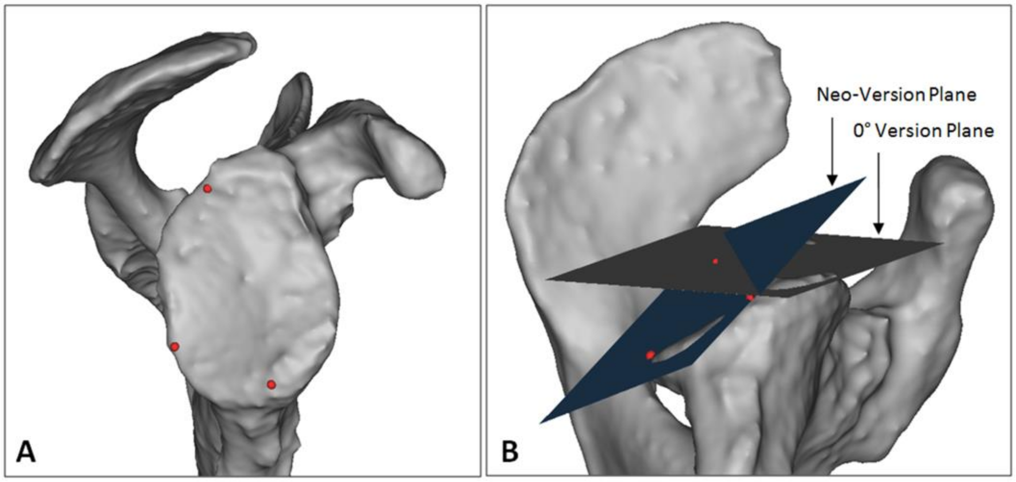

Figure 4.2: A three-dimensional scapular model of a patient with B2 erosion

A: The points (red dots) used to create the 3D version plane of the neoglenoid facet, termed the neo-version. Three points were used to define the neoglenoid version plane. One point was placed on the inferior aspect of the ridge of bone separating the neoglenoid from the paleoglenoid, a second point was placed on the superior aspect of the ridge of bone separating the neoglenoid from the paleoglenoid, and the third point was placed on the most medial point of the posterior rim of the eroded glenoid. **B:** A 3D scapula viewed from the inferior vantage point depicts the neo-glenoid version plane and the 0° version plane.

Table 4.1: Patient data with neo-version angle and the corresponding implant selection

Patient	Gender	Neo-Version Angle (°)	Implant Sizes Used at Each Implanted Version Angle					
			0° Version			10° Retroversion		
			Full-Wedge	Posterior-Wedge	Posterior-Step	Full-Wedge	Posterior-Wedge	Posterior-Step
1	M	24	Large 8°	Medium 15°	48 - 3mm	Large 8°	Medium 15°	48 - 3mm
2	M	34	X-Large 16°	X-Large 35°	56 – 7mm	X-Large 12°	X-Large 25°	56 – 5mm
3	M	38	X-Large 16°	Large 35°	48 – 7mm	X-Large 12°	Large 25°	48 – 5mm
4	F	21	Large 8°	Large 15°	52 – 3mm	Large 8°	Large 15°	48 – 3mm
5	M	18	Large 12°	Large 15°	52 – 3mm	Large 8°	Large 15°	52 – 3mm
6	M	40	X-Large 16°	Large 35°	52 – 7mm	X-Large 12°	Large 25°	52 – 5mm
7	F	26	Medium 12°	Small 25°	44 – 5mm	Medium 8°	Small 15°	44 – 3mm
8	F	35	Large 16°	Medium 35°	48 – 7mm	Large 12°	Medium 25°	48 – 5mm
9	F	30	Medium 8°	Medium 15°	44 – 3mm	Medium 8°	Medium 15°	44 – 3mm
10	M	14	X-Large 12°	X-Large 25°	56 – 5mm	X-Large 8°	X-Large 15°	56 – 3mm
11	M	15	X-Large 8°	Large 15°	52 – 3mm	X-Large 8°	Large 15°	52 – 3mm
12	M	12	X-Large 8°	X-Large 15°	56 – 3mm	X-Large 8°	X-Large 15°	56 – 3mm
13	F	28	Medium 12°	Medium 25°	48 – 3mm	Medium 8°	Medium 15°	48 – 3mm
14	F	30	Large 12°	Large 25°	52 – 5mm	Large 8°	Large 15°	52 – 3mm
15	F	17	Large 12°	Medium 25°	48 – 5mm	Large 8°	Medium 15°	48 – 3mm
16	F	40	Medium 16°	Medium 35°	48 – 7mm	Large 16°	Large 35°	48 – 7mm

cover the glenoid surface without overhang. The implant could be manipulated to rotate (clockwise/counter-clockwise and superoinferior) and translate (anteroposterior and superoinferior) as long as there was no overhang. To obtain full backside seating of the implant, it was incrementally medialized to simulate an absolute minimal amount of paleoglenoid reaming. Then, the step/wedge was selected to adequately correct for posterior bone loss with the smallest augment, while ensuring complete backside contact and 0° version.[14,16] This process was repeated for each implant design in randomized order.

The above process was also repeated for all implant designs with a clinical scenario of version restoration to 10° of retroversion. At this new version angle, the implant size and step/wedge height was re-assessed and altered if required to ensure full backside contact and no implant overhang (Table 4.1).

4.2.3 Volume of Bone Removal

Prior to implant insertion, the volume of each patient's scapular model was recorded. Following implant placement, the intersecting implant was removed from the scapula using a Boolean subtraction in Mimics® (Figure 4.3). This was completed separately for each of the three implant designs, the two version angles (0° and 10°), and for each of the 16 patients, for a total of 96 testing conditions. The volume of the scapular model, after implant subtraction, was re-measured and then differentiated from the index volume. This resulted in the volume of bone removed, in cubic millimeters, to fully seat the backside morphology of each particular implant. To remove bias due to implant surface area and its effect on bone removal, each volume of bone removal was also normalized by the two-dimensional area (i.e. footprint area) of the implant (Table 4.2). This metric, in units of millimeters, represents the ratio of the removed bone volume to the implant's footprint area, which is independent from size, but dependent on the backside morphology (step or wedge) or any other distinguishing backside features.

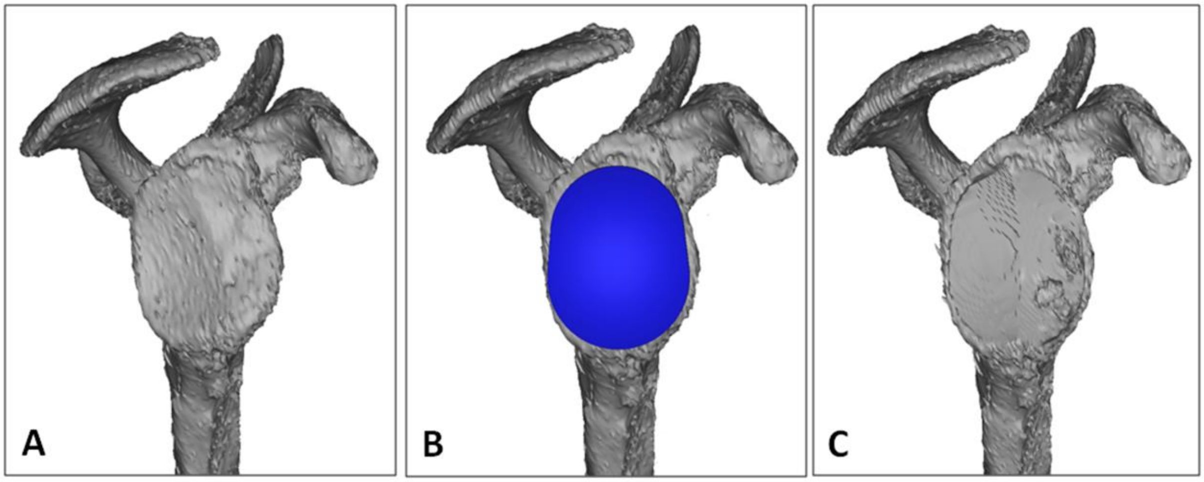

Figure 4.3: Three-dimensional models of a scapula with a posteriorly eroded type B2 glenoid

A: Note the orientation of the bony erosion in the posteroinferior direction. **B:** Virtual glenoid implantation with restoration of version to 0 degrees and 100% seating with a posterior augmented glenoid component. **C:** A Boolean subtraction intersection of the implant from the scapula demonstrating the quality of the remaining glenoid bone. Note the porous cysts on the anterior side of the glenoid.

Table 4.2: Implant footprint area used to normalize bone volume removal.

Implant Type	Size	Footprint Area (mm^2)
Full-Wedge	Small	520
	Medium	660
	Large	860
	Extra-Large	1050
Posterior-Wedge	Small	615
	Medium	770
	Large	940
	Extra-Large	1125
Posterior-Step	40	580
	44	705
	48	825
	52	960
	56	1110

4.2.4 Density and Porosity of Bone Beneath the Implant

To measure the density and porosity of bone immediately beneath the implant, a 2.5 mm thick section of glenoid was studied. To obtain a 2.5 mm thick volume of bone that matched each implants backside characteristics, each implant was further medialized 2.5 mm from its index position. This was performed for both the 0° version and 10° retroversion placements. Again using a Boolean subtraction, a 2.5 mm deep volume of bone under the implant was created (Figure 4.4). A mask of this model was then created in Mimics® to register the geometry of the bone section to the original DICOM images. Using a minimum threshold of 200 Hounsfield Units (HU) to preserve both cancellous and cortical bone,[2,10] bone density and porosity were measured as previously described by Knowles et al.[10] The bone density was measured in HU using the built-in Mimics measurement tools and bone porosity was calculated as the ratio of void volume (cysts and/or low density cancellous bone below the 200 HU threshold) to total volume. This measurement region represents the bone 0-2.5 mm below the implant, on which the implant rests.

4.2.5 Statistical Analysis

The total and normalized volume of bone removed were compared using two-way analysis of variance (ANOVA) and Tukey tests for pairwise comparisons for all patients and by gender and version angle (SigmaPlot V. 11.0, Systat Software Inc., Germany). Density and porosity were compared for all patients using two-way ANOVA and Tukey tests for pairwise comparisons for all patients and three-way ANOVA with Tukey tests for pairwise comparisons by gender.

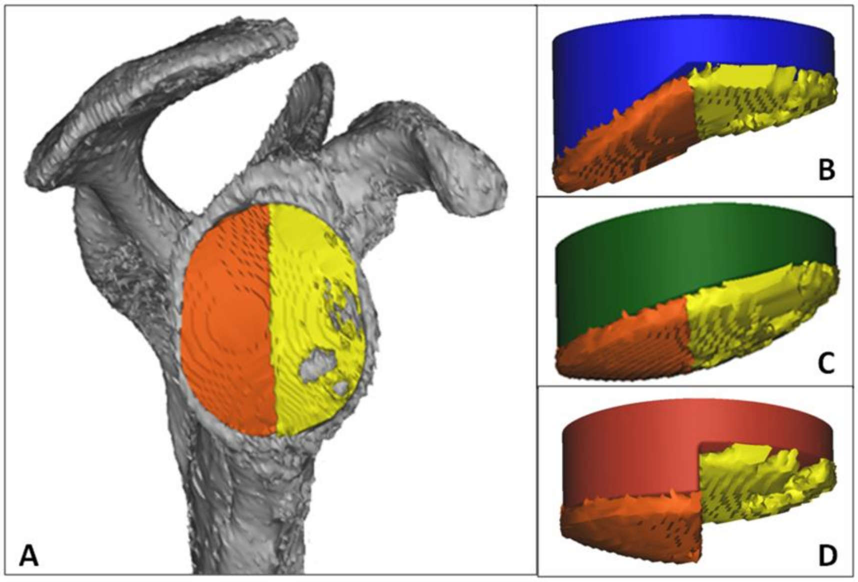

Figure 4.4: Representative images of the underlying bone 0-2.5 mm below virtually implanted augmented glenoid implants

A: The bone density in Hounsfield Units (HU) and porosity was calculated anterior (yellow) and posterior (orange) to the implant's centerline. The underlying bone volume studied for a **B:** posterior-wedge, **C:** full-wedge, **D:** and posterior-step are depicted. The bone porosity is the ratio of void volume (cysts and/or low density cancellous bone below the 200 HU threshold) to total volume.

4.3 RESULTS

4.3.1 Volume of Bone Removal

The choice of implant design had a significant effect on the volume of glenoid bone removal ($p < 0.001$) (Figure 4.5A). When using the augmented implants to correct retroversion to an ideal 0°, the posterior-wedged implant removed a mean of 1347 mm^3 less total bone than the posterior-step implant ($p < 0.001$) and a mean 1010 mm^3 less than the full-wedged implant ($p = 0.004$). There was no significant difference between the total bone removal of the posterior-step and full-wedge implants ($p = 0.509$). When correcting version to 10° of retroversion, the posterior-wedge implant removed significantly less total bone (mean 790 mm^3, $p = 0.029$) than the posterior-step implant. However, there was no significant difference in total bone removed between the posterior-wedge and full-wedge implants ($p = 0.143$) or between the posterior-step and full-wedge implants ($p = 0.766$).

When the volume of bone removed was normalized to the implant's footprint area, implant choice again had a significant effect ($p < 0.001$) (Figure 4.5 B). There was a significant difference between the posterior-wedge and both the posterior-step (0° version: $p < 0.001$, 10° retroversion: $p = 0.003$) and full-wedge (0° version: $p < 0.001$, 10° retroversion: $p = 0.037$), but no difference between the posterior-step and full-wedge ($p \geq 0.335$) at either version angle.

Male patients had significantly more bone removal than female patients at 0° version for the full-wedge ($p = 0.019$), but no significant difference for the posterior-step ($p = 0.053$) or posterior-wedge implants ($p = 0.076$) (Figure 4.6). At 10° retroversion, male patients had significantly more bone removal than female patients for the full-wedge ($p = 0.016$) and the posterior-step ($p = 0.018$), but no significant difference for the posterior-wedge implant ($p = 0.403$). These significant differences were not observed when the bone removal was normalized by the implant's footprint area ($p \geq 0.084$) (Figure 4.6).

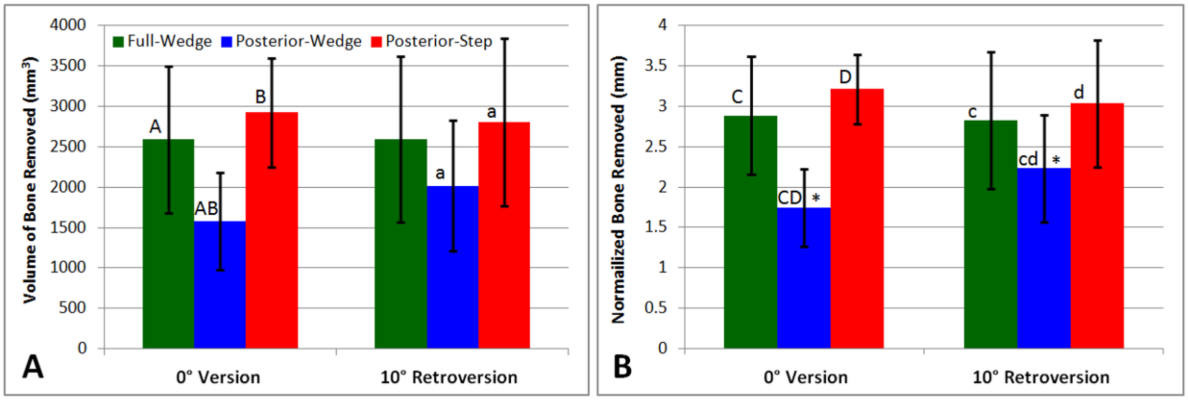

Figure 4.5: Glenoid bone removed by the three augmented glenoid implants

A: The total volume of glenoid bone removed at 0° version and 10° retroversion. **B:** The bone removed normalized by the footprint area of the implant at 0° version and 10° retroversion. Significant difference is indicated by bars sharing a common letter/symbol.

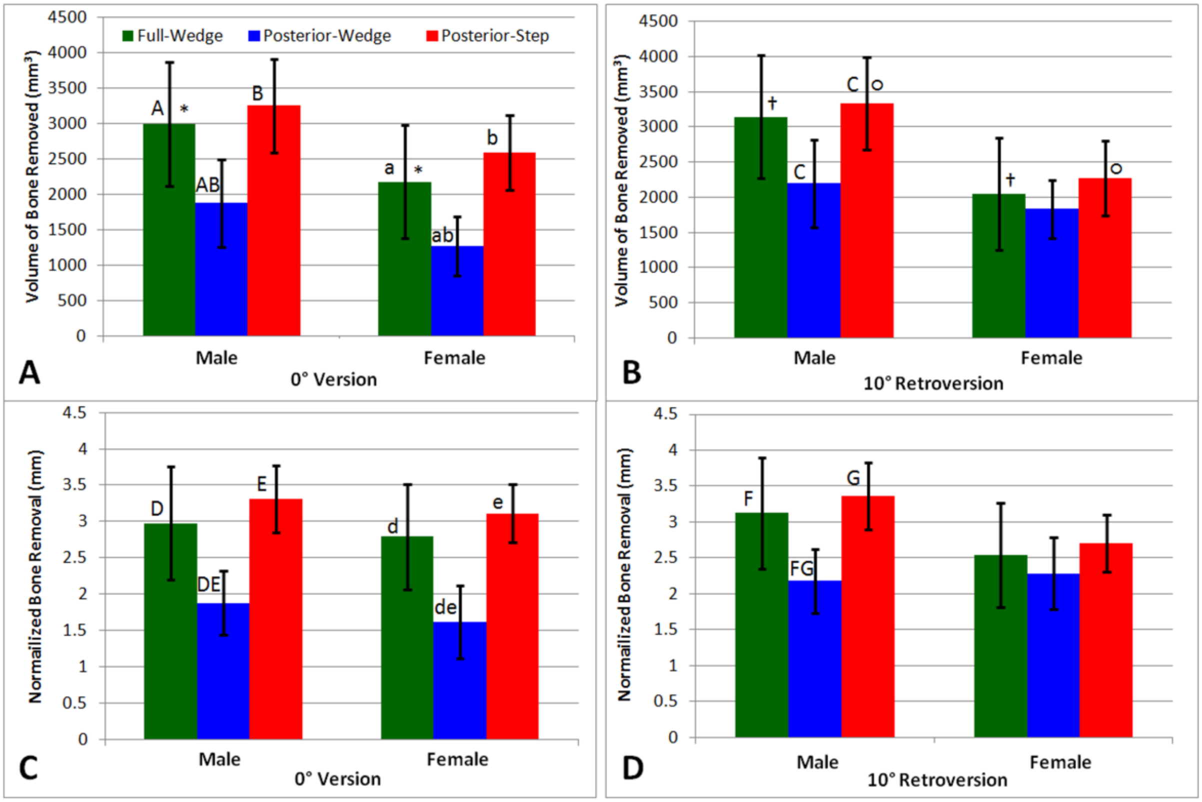

Figure 4.6: Bone removed by three augmented glenoid implants in male (n = 8) and female (n = 8) patients

A: Volume of bone removed at 0° version. **B:** Volume of bone removed at 10° retroversion. **C:** Bone removed normalized by the footprint area of the implant at 0° version. **D:** Bone removed normalized by the footprint area of the implant at 10° retroversion. Significant difference is indicated by bars sharing a common letter/symbol.

4.3.2 Density and Porosity

Within the posterior half of the glenoid, the density of the remaining bone when using the posterior-wedge implant was significantly denser (mean 83 HU greater) than the posterior-step implant ($p = 0.048$) at 0° version. There were no other significant differences in bone density between the other implants within the anterior or posterior regions ($p \geq 0.380$) at this version angle. When comparing bone density in the anterior to the posterior regions of the glenoid by implant type, the full-wedge was a mean 196 HU more dense ($p < 0.001$), the posterior-wedge a mean 177 HU ($p < 0.001$), and the posterior-step a mean 100 HU ($p = 0.005$) more dense in the posterior as compared to the anterior region (Figure 4.7). For the models corrected to 10° retroversion, there was also a significant difference in underlying bone density posterior and anterior ($p < 0.001$), but no significant differences between implants ($p = 0.370$).

When assessing porosity for the 0° version correction cohort, there was a significant difference in the underlying bone porosity comparing anterior to posterior regions ($p < 0.001$), but no significant differences between implants ($p = 0.260$) (Figure 4.7C). For the 10° retroversion cohort, there was also a significant difference in underlying bone porosity comparing anterior to posterior regions ($p < 0.001$), but also no differences between implants ($p = 0.559$).

For male and female patients at 0° version, there were significant differences in underlying bone density in the anterior and posterior regions when allowing for the effects of all other factors ($p \leq 0.001$). There were no significant differences between implant types ($p = 0.050$). At 10° retroversion, there were also significant differences in underlying bone density in the anterior and posterior regions when allowing for the effects all other factors ($p \leq 0.035$). There were no significant differences between implant types ($p = 0.366$) or underlying bone porosity by implant type when allowing for all other factors (0° version: $p = 0.133$, 10° retroversion: $p = 0.508$).

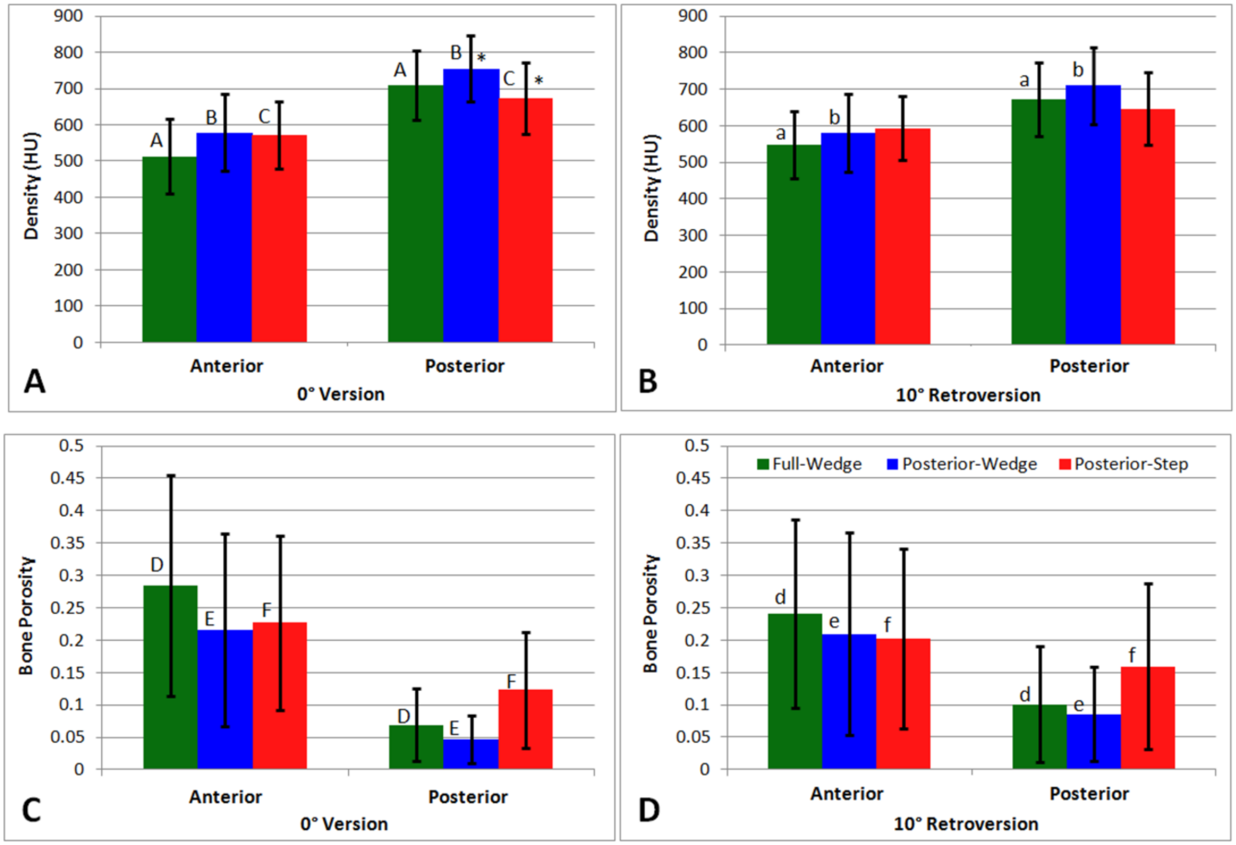

Figure 4.7: Glenoid bone density and porosity 0 - 2.5 mm below the three augmented implant designs for all patients (n = 16)

A: Bone density in the anterior and posterior regions by implant when placed at 0° version. **B:** Bone density by implant when placed at 10° retroversion. **C:** Bone porosity by implant when placed at 0° version. **D:** Bone porosity by implant when placed at 10° retroversion. Significant difference is indicated by columns sharing a common letter/symbol. The bone porosity is the ratio of void volume (cysts and/or low density cancellous bone below the 200 HU threshold) to total volume.

4. 4 DISCUSSION:

The results of this study indicate that there are substantial differences in the amount of glenoid bone removal required to fully seat different designs of posterior augmented implants. Aside from bone removal, it is apparent that the density and porosity of the remaining supporting bone immediately beneath the implant substantially varies among implant designs. Recent literature has demonstrated that preservation of glenoid subarticular bone is important in resisting implant migration and loosening.[21] When inserting an augmented implant, therefore, we can postulate that the same principles may be important and bone removal should be minimized to maximize implant support and decrease the risk of implant subsistence and/or migration.

In this study we chose to correct version to an ideal 0 degrees and to 10 degrees of retroversion, to account for the variation of native retroversion which may exist within the population.[3] It can be inferred that as the severity of posterior erosion increases, the size of the step/wedge must also increase to account for the missing bone. This was confirmed with our results, as generally greater degrees of pathologic neo-version required progressively larger posterior augments (Table 1). Additionally, in assessing the 10 degree retroversion sample, we found that by lessening the degree of correction we were able to downsize the posterior augment. We initially postulated that lessening the degree of correction and downsizing the step/wedge may result in less bone removal. Interestingly, our results did not support this, as we found no significant reduction in the bone removal when downsizing. However, when correcting to 10° retroversion, the bone density and porosity in the anterior and posterior halves of the glenoid were more uniform, which may provide some favourable biomechanical properties for initial implant stability.

When bone removal was normalized by the implant's footprint area - a metric which more accurately represents the variation between implant shape and bone removal, the posterior-wedged implant removed significantly less bone then both the full-wedged and stepped implants. This implant shape preserves the most bone, which may be important when considering the long-term outcomes and future requirements for revision surgeries. However, it should be noted that although less bone is removed, significant differences still exist in the density and porosity of the underlying bone in the anterior and posterior hemispheres of the implant, as with the other two augmented implants. These extreme differences in the density and porosity between the anterior and posterior regions may have implications with implant migration and subsidence. These concerns would be uniform across all B2 erosions.

The final placement of the implant was also dependent on the geometry of each individual glenoid. Due to the variation in implant shapes by manufacturer, certain augmented implants may more accurately reproduce the native glenoid geometry, while reducing bone removal in each specific case. Ideally, to fully realize the best-fit glenoid implant for each specific patient, a computerized pre-operative planning software making use of three-dimensional CT-based models of the glenoid with properly sized implants would be best. For example, patients with gradual posterior erosion that involves most of the glenoid, having a very large neoglenoid with a thin rim of remaining paleoglenoid, may be better suited to a full-wedge implant, as it will likely remove less overall bone than to seat a posterior-wedge. These pre-operative planning tools may allow for optimization of implant positioning and measurements to be taken which are not currently possible with traditional methods.

Although fixation devices were omitted in this study, it has been reported that excessive implant medialization results in peg perforation in standard glenoid implants[7] and also in augmented implants.[15] Joint medialization was not explored in this study, instead we focused on implant placement and underlying bone support, but it is also important to understand that implant medialization may result in peg perforation, compromising fixation. Also, additional bone removal is required in order to facilitate the fixation devices, which further compromises underlying bone support. It is therefore even more essential to ensure the implant backside removes the least amount of bone so enough bone remains to ensure effective fixation and support.

The results of our study are consistent with the total volume of bone removed in surrogate glenoid models previously investigated by Roche et al.[13] Their study presents important aspects as related to augmented glenoid component designs; however, we believe the results of our study may be more clinically relevant, since we chose to examine patients with B2 erosion as compared to surrogate models that simulate B2 erosion. Choosing patients with B2 erosions does however introduce a limitation of our study in that although the patients were classified by a fellowship trained shoulder surgeon, the patient group may not fully represent the full range of B2 erosion patient's that typically require augmented glenoid components within the population.

A further limitation of this study was that we did not evaluate bone removal by fixation devices (i.e. pegs or keels). Due to the variations in size, shape and style of fixation devices, we decided this would introduce a level of bias that could not be accounted for within the small volumes of bone removed. To further evaluate the effect of underlying bone support and the fixation of augmented glenoid components, future directions would be to assess optimally placed implants on the basis of strain induced to the bone under physiologic loading using finite element analysis. Another limitation with our study is that we did not examine the biomechanical effects of these various implant shapes. Iannotti et al[9] studied the lift off resistance of the full-wedge and the posterior-step implants in a glenoid model with homogeneous bone properties and found the posterior-step to be superior. Unfortunately, they tested the implants on a homogenous glenoid model, which does not accurately represent the clinical scenario of variable bone density and porosity in the paleoglenoid and neoglenoid. It is conceivable that implant designs that test favourably on homogenous models may fare differently on clinically relevant models with variable bone quality.

4.5 REFERENCES

1. Beuckelaers E, Jacxsens M, Van Tongel A, De Wilde LF. Three-dimensional computed tomography scan evaluation of the pattern of erosion in type B glenoids. J Shoulder Elbow Surg. 2014;23(1):109-116. doi: 10.1016/j.jse.2013.04.009

2. Bryce CD, Pennypacker JL, Kulkarni N, Paul EM, Hollenbeak CS, Mosher TJ, et al. Validation of three-dimensional models of in situ scapulae. J Shoulder Elbow Surg. 2008;17(5):825-832. doi: 10.1016/j.jse.2008.01.141

3. Churchill RS, Brems JJ, Kotschi H. Glenoid size, inclination, and version: an anatomic study. J Shoulder Elbow Surg. 2001;10(4):327-332. doi: 10.1067/mse.2001.115269

4. Clavert P, Millett PJ, Warner JJ. Glenoid resurfacing: what are the limits to asymmetric reaming for posterior erosion? J Shoulder Elbow Surg. 2007;16(6):843-848. doi: 10.1016/j.jse.2007.03.015

5. Denard PJ, Walch G. Current concepts in the surgical management of primary glenohumeral arthritis with a biconcave glenoid. J Shoulder Elbow Surg. 2013;22(11):1589-1598. doi: 10.1016/j.jse.2013.06.017

6. Ganapathi A, McCarron JA, Chen X, Iannotti JP. Predicting normal glenoid version from the pathologic scapula: a comparison of 4 methods in 2- and 3-dimensional models. J Shoulder Elbow Surg. 2011;20(2):234-244. doi: 10.1016/j.jse.2010.05.024

7. Hoenecke HR, Jr., Hermida JC, Dembitsky N, Patil S, D'Lima DD. Optimizing glenoid component position using three-dimensional computed tomography reconstruction. J Shoulder Elbow Surg. 2008;17(4):637-641. doi: 10.1016/j.jse.2007.11.021

8. Iannotti JP, Greeson C, Downing D, Sabesan V, Bryan JA. Effect of glenoid deformity on glenoid component placement in primary shoulder arthroplasty. J Shoulder Elbow Surg. 2012;21(1):48-55. doi: 10.1016/j.jse.2011.02.011.

9. Iannotti JP, Lappin KE, Klotz CL, Reber EW, Swope SW. Liftoff resistance of augmented glenoid components during cyclic fatigue loading in the posterior-superior direction. J Shoulder Elbow Surg. 2013;22(11):1530-1536. doi: 10.1016/j.jse.2013.01.018

10. Knowles NK, Athwal GS, Keener JD, Ferreira LM. Regional bone density variations in osteoarthritic glenoids: A comparision of symmetric to asymmetric (type B2) erosions. J Shoulder Elbow Surg. 2014 In Press.

11. Kwon YW, Powell KA, Yum JK, Brems JJ, Iannotti JP. Use of three-dimensional computed tomography for the analysis of the glenoid anatomy. J Shoulder Elbow Surg. 2005;14(1):85-90. doi: 10.1016/j.jse.2004.04.011

12. Nowak DD, Gardner TR, Bigliani LU, Levine WN, Ahmad CS. Interobserver and intraobserver reliability of the Walch classification in primary glenohumeral arthritis. J Shoulder Elbow Surg. 2010;19(2):180-183. doi: 10.1016/j.jse.2009.08.003

13. Roche CP, Diep P, Grey SG, Flurin PH. Biomechanical impact of posterior glenoid wear on anatomic total shoulder arthroplasty. Bull Hosp Jt Dis (2013). 2013;71 Suppl 2:S5-11.

14. Sabesan V, Callanan M, Ho J, Iannotti JP. Clinical and radiographic outcomes of total shoulder arthroplasty with bone graft for osteoarthritis with severe glenoid bone loss. J Bone Joint Surg Am. 2013;95(14):1290-1296. doi: 10.2106/JBJS.L.00097.

15. Sabesan V, Callanan M, Sharma V. Guidelines for the selection of optimal glenoid augment size for moderate to severe glenohumeral osteoarthritis. J Shoulder Elbow Surg. 2014;23(7):974-981. doi: 10.1016/j.jse.2013.09.022

16. Sabesan V, Callanan M, Sharma V, Iannotti JP. Correction of acquired glenoid bone loss in osteoarthritis with a standard versus an augmented glenoid component. J Shoulder Elbow Surg. 2014;23(7):964-973. doi: 10.1016/j.jse.2013.09.019

17. Sears BW, Johnston PS, Ramsey ML, Williams GR. Glenoid bone loss in primary total shoulder arthroplasty: evaluation and management. J Am Acad Orthop Surg. 2012;20(9):604-613. doi: 10.5435/JAAOS-20-09-604

18. Simon P, Gupta A, Pappou I, Hussey MM, Santoni BG, Inoue N, et al. Glenoid subchondral bone density distribution in male total shoulder arthroplasty subjects with eccentric and concentric wear. J Shoulder Elbow Surg. 2014. doi:10.1016/j.jse.2014.06.054

19. Terrier A, Ston J, Larrea X, Farron A. Measurements of three-dimensional glenoid erosion when planning the prosthetic replacement of osteoarthritic shoulders. Bone Joint J. 2014;96-B(4):513-518. doi: 10.1302/0301-620X.96B4.32641

20. Walch G, Badet R, Boulahia A, Khoury A. Morphologic study of the glenoid in primary glenohumeral osteoarthritis. J Arthroplasty. 1999;14(6):756-760. doi: 10.1016/S0883-5403(99)90232-2

21. Walch G, Moraga C, Young A, Castellanos-Rosas J. Results of anatomic nonconstrained prosthesis in primary osteoarthritis with biconcave glenoid. J Shoulder Elbow Surg. 2012;21(11):1526-1533. doi: 10.1016/j.jse.2011.11.030.

CHAPTER 5 – CORRELATIONS BETWEEN BONE STRAIN AND DENSITY UNDER PHYSIOLOGIC JOINT LOADING: A FINITE ELEMENT ANALYSIS

OVERVIEW: *This chapter describes a finite element model that is built from the CT scan of a patient diagnosed with type B2 glenoid erosion. The model incorporates the patient-specific bone density distribution method reported in Chapter 2. Five different augmented glenoid component designs are compared in this simulation model. Three of these designs are based on the industry designs from Chapter 4, and two are custom designs based on the average type B2 morphology reported in Chapter 3.*

5.1 INTRODUCTION:

Osteoarthritis-induced glenoid bone loss can be classified by two common morphological erosion patterns: asymmetric and symmetric. In symmetrically eroded glenoids requiring joint replacement, the glenoid articular surface is reamed to match the curvature of the implant, ensuring full backside contact and effective fixation. This method, when used in asymmetrically eroded glenoids to level the bi-concave articular surface is referred to as eccentric reaming, and is the preferred method of glenoid preparation. However, it has been suggested that acquired retroversion correction of greater than 15° of this bi-concave morphology cannot be corrected by eccentric reaming alone.[7,15] Additionally, this bi-concavity, consisting of the native articular surface (paleoglenoid) and a new articular surface (neoglenoid),[8] may require substantial bone removal in order to facilitate the placement of standard glenoid components. This pathoanatomy therefore presents a challenging scenario for surgical joint reconstruction in these complex cases.

Alternatively, augmented glenoid components have recently gained popularity due to their inherent bone preservation design. Recent studies have suggested that these implants preserve underlying bone;[11,14] however, underlying bone density varies in the neoglenoid and paleoglenoid regions, which has unknown consequences for early implant fixation and support. Furthermore, it has been suggested that bone density varies in asymmetrically eroded type B2[22] glenoids as compared to symmetrically eroded glenoids,[13,19] which has unknown consequences for early implant fixation and support.

Current augmented glenoid component designs contain a step or wedge symmetric about the implants centerline, assuming bone loss occurs in the posterior direction. It has recently been suggested that bone loss is not purely posterior, but is oriented in a posteroinferior direction.[4,12,20] This further increases the difficulty of implant selection or reaming techniques to restore joint mobility, as this current design may result in unnecessary bone removal or malrotated implants. Furthermore, it is essential to understand the biomechanical differences imposed by altered bone density distribution and bone erosion in the pathologic joint in order to modify reaming or cement fixation techniques to optimize early bone support and fixation.

Regions of bone directly below the implant were used to determine the effect of regional variations in bone density on the stress and strain distribution induced by the augmented implant backside designs under physiologic glenohumeral joint loading

5.2 MATERIALS AND METHODS:

5.2.1 Implant Model Generation

A total of five augmented glenoid component designs were modelled to assess varying backside geometries (Figure 5.1). These included a posterior-step, posterior-wedge, full-wedge, and two custom implants (parametric wedge and parametric step). The parametric implants were identical to the posterior-wedge and posterior-step implants; however, the augment was aligned with the orientation angle of glenoid erosion relative to the glenoid superoinferior axis, reported in Chapter 3.[12]

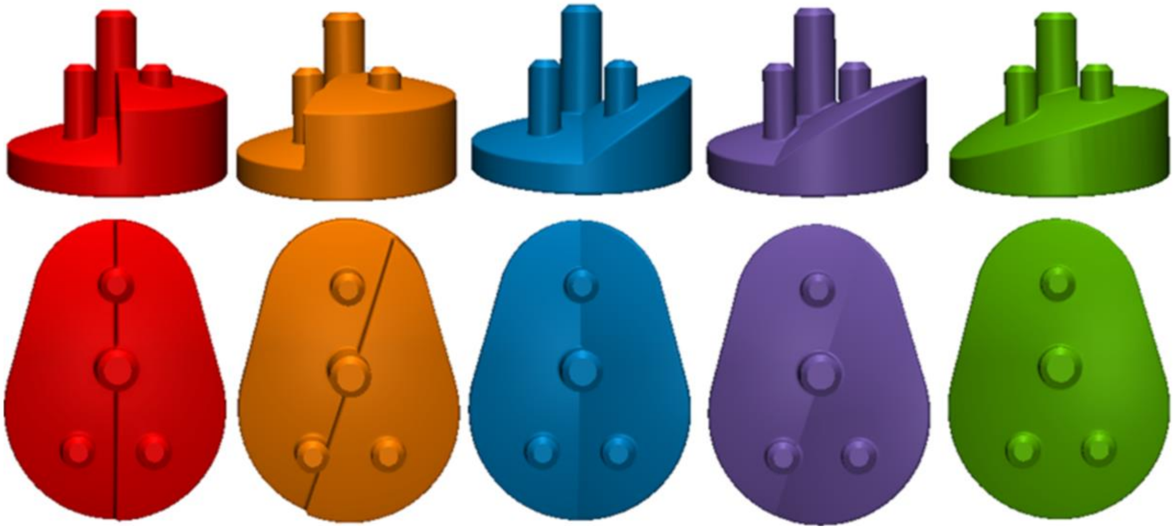

Figure 5.1: Five augmented glenoid component designs tested

Step (red), parametric-step (orange), posterior-wedge (blue), parametric-wedge (purple) and full-wedge (green). The augment angle of the parametric designs was based on the average type B2 erosion morphology of Chapter 3. All implants have the same dimensions and peg sizes/locations and differ only by backside augment geometry.

All implants were based on averaged characteristics of commercially available augmented implants, and were constructed as CAD models (Desaults Systemes Solidworks Corporation,Waltham, MA, USA) with identical peg sizes/locations, geometrical shape, and articular and backside curvatures. This was done to assess the implants on strictly the backside geometry and control for the contribution of confounding bias from fixation device design. Peripheral peg diameters were 4.75 mm and the central peg diameter was 6 mm. All implants were anatomically 'pear-shaped' with a 12 mm superior radius, 16 mm inferior radius, and a 36 mm articular surface curvature. All implants had a 4 mm non-augmented edge thickness.

Augment sizes were chosen to fully correct acquired retroversion while minimizing paleoglenoid reaming. The augments chosen by implant type were: 35° posterior-wedge, 7 mm step, and 16° full-wedge. All implants were transferred to Abaqus® (V.6.12, Simulia, Providence, RI), meshed using quadratic tetrahedral elements (C3D10), and modelled using ultra-high molecular weight polyethylene (UHMWPE) ($E=690$ MPa, $\nu = 0.4$).

Clinical practice at our institution as recommended by the implant manufacturers, is to achieve peg only cement fixation, leaving the implant backside exposed to the reamed bone surface. The mesh geometry of the simulated cement mantle around the pegs was created by dilating the peg diameters and subtracting the original pegs to ensure a uniform 1 mm cement mantle (Figure 5.2). The mantle was transferred to Abaqus®, meshed using quadratic tetrahedral elements (C3D10), and assigned poly-methylmethacrylate (PMMA) material properties ($E=2000$ MPa, $\nu = 0.3$).[21,25]

The humeral component was modelled as a half-sphere with a radius of 32 mm to produce a non-conforming mate with the recommended 4 mm mismatch to the articulation of the glenoid component. The implant was transferred to Abaqus®, meshed using quadratic tetrahedral elements (C3D10), and assigned cobalt-chromium material properties ($E=200000$ MPa, $\nu = 0.3$).[9]

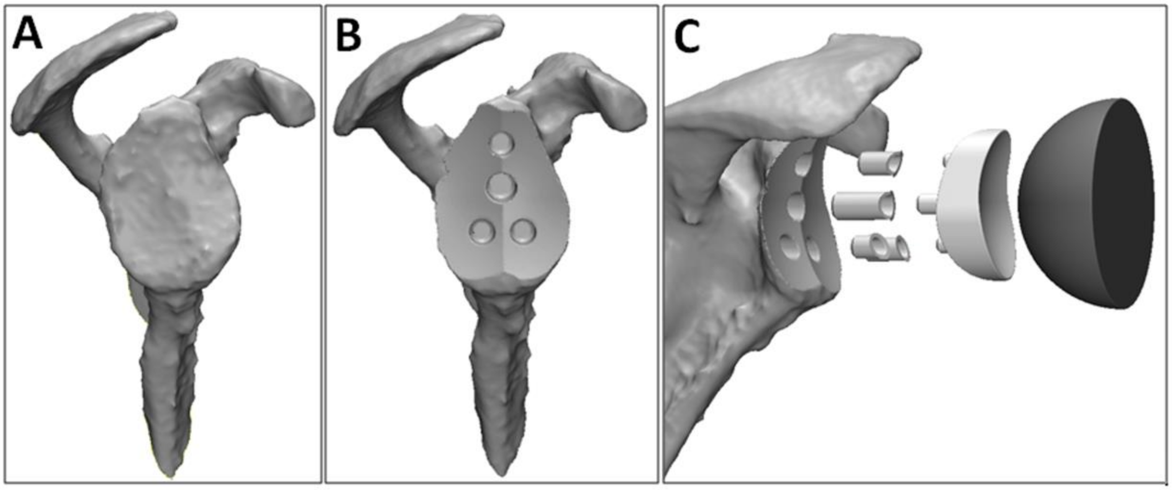

Figure 5.2: Three-dimensional reconstructions of the scapula used for finite element modeling

The intact scapula **(A)**, reamed scapula **(B)**, and reamed scapula, peg cement mantle, augmented glenoid component, and humeral component **(C)**, are depicted.

5.2.2 Scapular Model Generation

Computed Tomography (CT) scan data in digital imaging and communications in medicine (DICOM) format was collected for one patient (male, 70) using a multi-slice scanner (GE Discovery CT750 HD, Milwaukee, WI) with standard clinical settings (120KvP, 144.54 mAs, 1 mm slice spacing, 1.25 slice thickness and 250 FOV). This patient was scheduled to undergo total joint replacement surgery at our institution and was classified as having Walch type B2[22] glenoid erosion by a fellowship trained shoulder surgeon (G.S.A) using a clinically validated method.[16] A scapular model was generated from the DICOM data using Mimics® software (Materialize, V.17.0, Leuven, BE). The virtually reamed glenoid surface was completed separately for each implant design using a similar method as previously described.[14] Correction to 6° retroversion was chosen to minimize paleoglenoid reaming, while ensuring optimal backside contact. Each implant's central axis was aligned to the superoinferior axis of the glenoid. Virtual reaming was accomplished by subtracting the backside geometry of each implant from the scapula model. The implant pegs, used for virtual bone removal, were oversized by 1 mm in order to accommodate a 1 mm thick cement mantle. This method ensured perfect contact between the implant backside, cement mantle and bone. Each of the five scapula models was truncated identically to reduce the model size and computational time (Figure 5.2C). Sufficient medial bone remained for accurate boundary conditions and glenoid loading distribution.

Bone was discretized using 10-node tetrahedral (C3D10) elements (3-Matic®, Materialize, V.9.0, Leuven, BE). A mesh convergence analysis was used to determine the optimal mesh density. Following mesh generation, Mimics® material editor was used to register the model to the original DICOMs for material property assignment. A heterogeneous material property distribution was assigned to the scapula model, based on the Hounsfield Unit distribution of the patient's CT scan. The density-modulus relationship developed by Carter and Hayes[5] ($E=2875\rho_{app}^3$, $\nu = 0.3$) was applied to cancellous elements. This equation was selected due to its sensitivity to small changes in bone density in the lower density cancellous range, which is characteristic of the osteoarthritic glenoid. For cortical elements ($\rho_{app} \geq 1.85$ g/cc),[1] constant properties were applied (E=20000 MPa, $\nu = 0.3$).[10]

5.2.3 Boundary and Loading Conditions

The scapular FE model was exported to Abaqus® with the meshed humeral component, glenoid component and cement mantle. Boundary conditions were applied to fully constrain the medial scapular border.[17] The cement mantle was fully constrained to the bone and glenoid implant pegs were fully constrained to the cement mantle. The implant was assigned a surface contact constraint. A compressive load of 750 N was applied to the glenoid implant articular surface by the humeral component to represent joint contact loads determined from *in-vivo* testing.[3] This load represents 85% body weight at 75° of abduction. A tangential frictional coefficient of 0.07 was applied between the humeral and glenoid components.[6,18]

5.2.4 Measurement Regions, Outcome Variables and Statistical Analysis

Bone density and von Mises stress[17] and strain values were calculated in quadrant regions of the bone supporting the implant, at two depths 0 - 2.5 mm and 2.5 - 5 mm medial to the backside of each implant, similar to the method described in Chapters 2 and 4. The volume of each depth region was generated by medializing the implant 2.5 mm and 5 mm in order to obtain exact implant geometry, and quadrants were determined using the implant's superoinferior and anteroposterior axes as a reference coordinate system, using the same method as Chapters 2 and 4.[13,14] Stress and strain data for the bone was extracted from the Abaqus® output files within each region using custom code (Matlab®, Mathworks, Natick, MA), which also calculated average values within each quadrant region. Bone density was calculated by registering the quadrant regions to the original DICOM images in Mimics®, using the same method as in Chapter 4. Stress and strain values were also calculated for each augmented glenoid component. Additionally, under implant surface bone strain and density was determined and linear regression was used to assess the variation in under implant bone strain as a function of bone density (SigmaPlot V. 11.0, Systat Software Inc., Germany).

5.3 RESULTS

Bone density was lowest in the anterosuperior quadrant and highest in the posteroinferior quadrant for all implants at both depths (Figure 5.3). At the 0 to 2.5 mm depth, all implants had similar average bone densities with variation occurring among quadrants in the parametric augmented implant designs. Large variations by quadrant were observed among implant types at the 2.5 to 5 mm depth (Figure 5.3).

There were very weak correlations between under-implant bone strain and bone density for all implant designs. For the step, parametric-step, posterior-wedge, parametric-wedge and full-wedge, 0.7% (R^2=0.007), 0.2% (R^2=0.002), 1.8% (R^2=0.018), 1.3% (R^2=0.013), and 1.2% (R^2=0.012) of the variation in under implant bone strain was explained by the variation in the associated bone density, respectively.

By quadrant, average bone strains were greatest at both depths (0 to 2.5 mm and 2.5 to 5 mm) in the anterosuperior quadrant for all implants except for the step, which was greatest in the posterosuperior quadrant, and the parametric-step which was slightly higher in the anteroinferior quadrant. All five implants showed similar trends in average bone strains by quadrant (Figure 5.4). The step and posterior wedge implants showed the most uniform under implant distribution of strains under the applied loading (Figure 5.5).

All implants had similar bone stress distributions radiating from the central peg (Figure 5.6). The posterior-step, parametric-step, and parametric-wedge implants showed the greatest stress and strain around the central peg (Figure 5.6). The posterior-wedge and full-wedge implants showed less stress and strain.

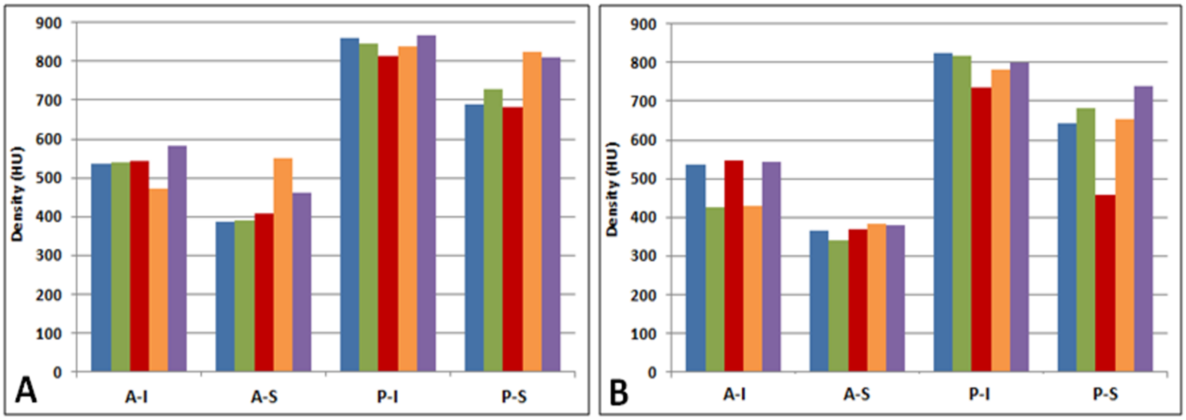

Figure 5.3: Average bone density by quadrant at two depths (A: 0 to 2.5 mm and B: 2.5 to 5 mm) below five augmented glenoid component designs

Step (red), parametric-step (orange), posterior-wedge (blue), parametric-wedge (purple) and full-wedge (green). The quadrants are anteroinferior (A-I), anterosuperior (A-S), posteroinferior (P-I), and posterosuperior (P-S).

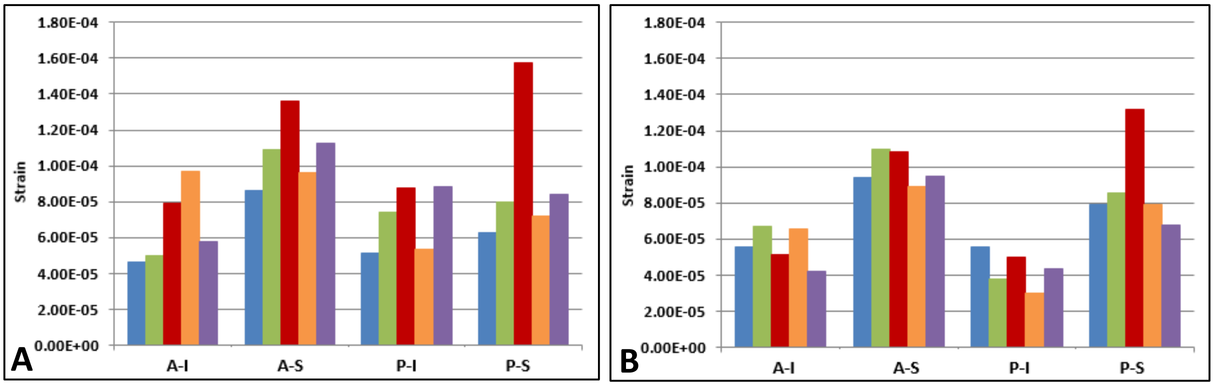

Figure 5.4: Average nodal bone strains by quadrant at two depths (A: 0 to 2.5 mm and B: 2.5 to 5 mm) below five augmented glenoid component designs

Step (red), parametric-step (orange), posterior-wedge (blue), parametric-wedge (purple) and full-wedge (green). The quadrants are anteroinferior (A-I), anterosuperior (A-S), posteroinferior (P-I), and posterosuperior (P-S).

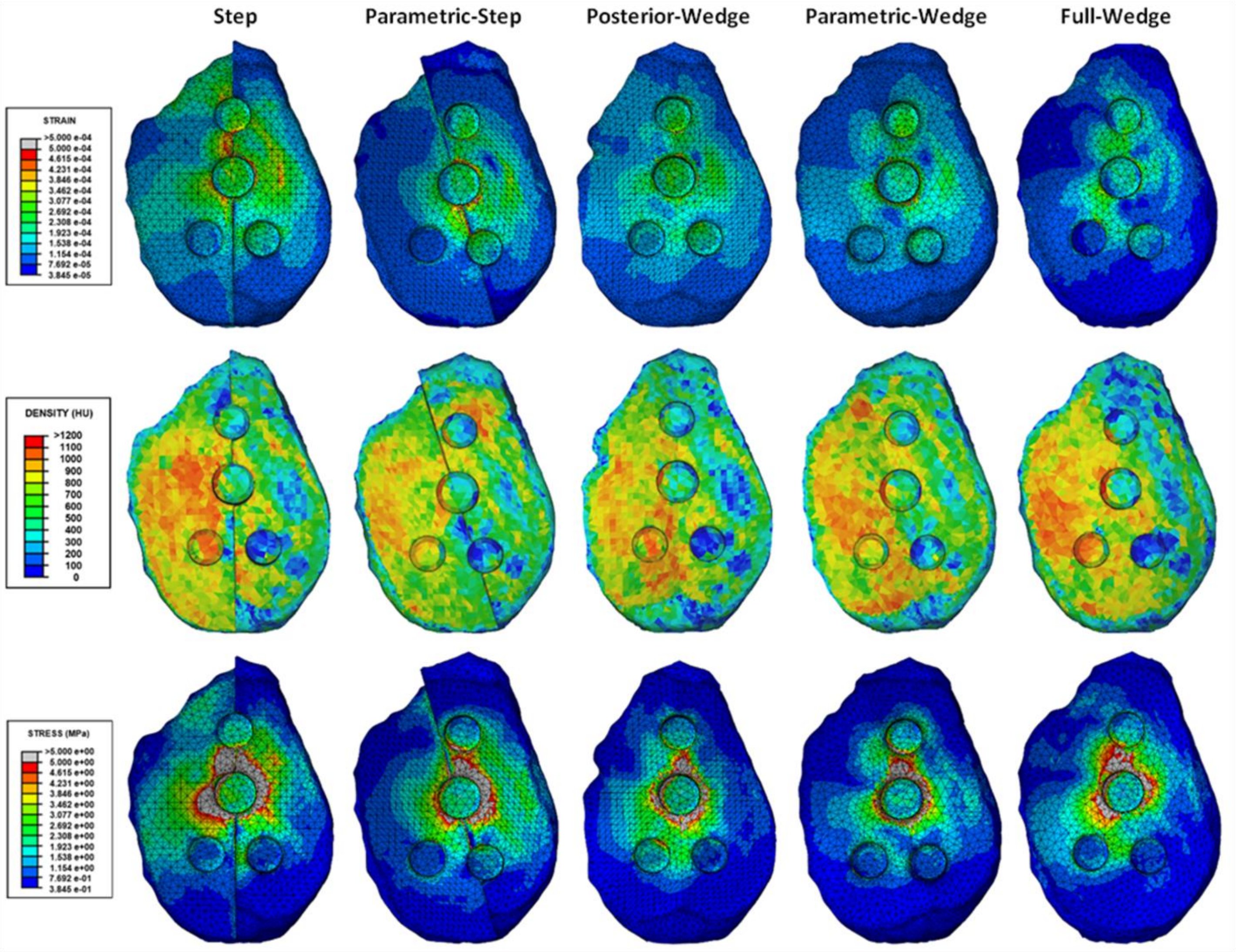

Figure 5.5: Under-implant bone strain (top), bone density (middle) and bone von Mises stress (bottom) distributions for five augmented glenoid component designs

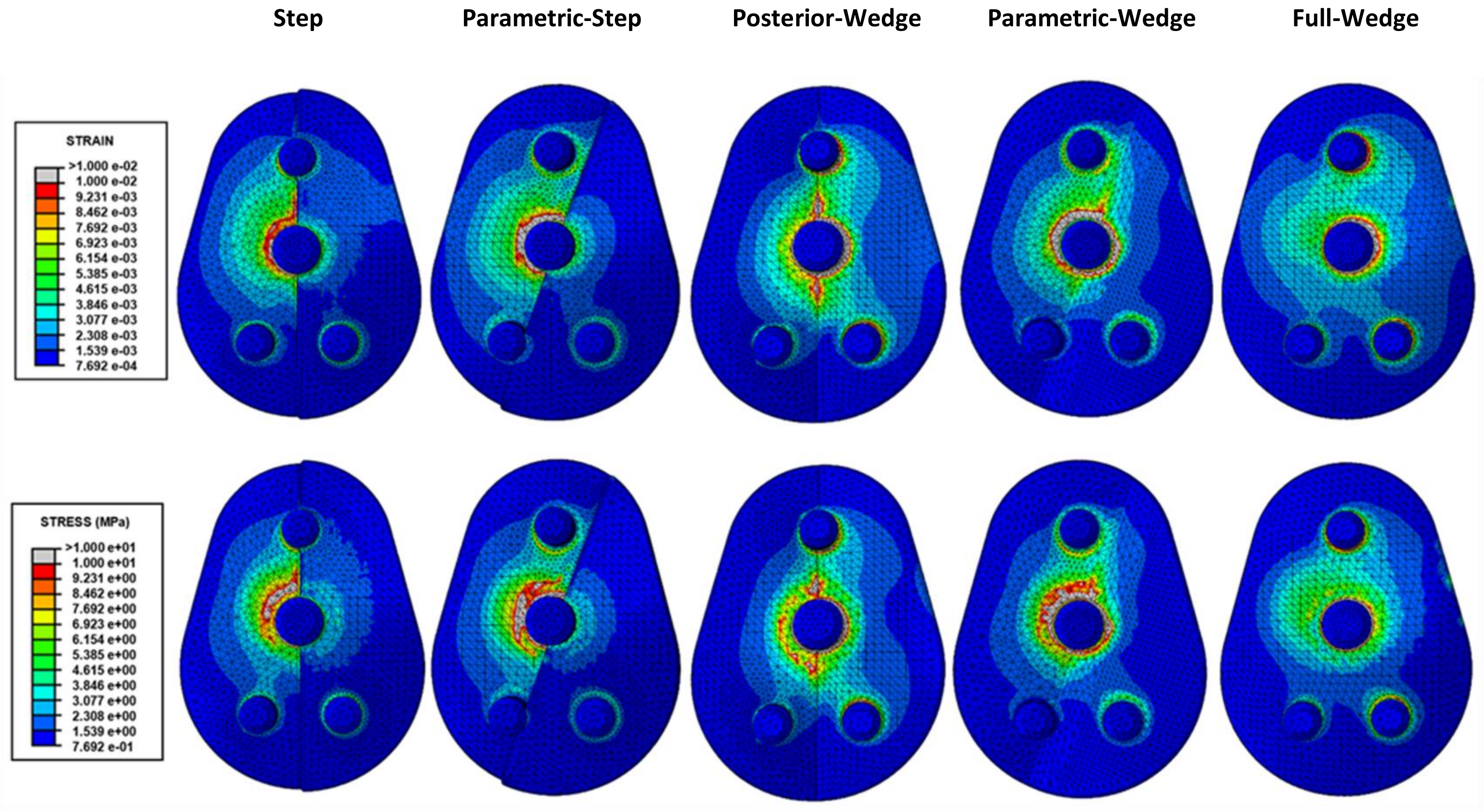

Figure 5.6: Implant strain (top), and von Mises stress (bottom) distributions for five augmented glenoid component designs.

DISCUSSION:

Recent studies have demonstrated that the bone density distribution in asymmetrically eroded glenoids differs greatly from symmetrically eroded glenoids.[13,19] It has also been suggested that the preservation of underlying bone is desirable in glenoid component placement to ensure optimal early component fixation and support in order to minimize subsidence. [14,23,24] It follows that posterior bone, with greater bone density, should be preserved for implant support. However, no studies have addressed the biomechanical effects of bone density distribution following implantation of augmented glenoid components. Furthermore, no studies have addressed variations that may occur due to bone density distributions that occur in osteoarthritic glenoids, especially those observed in asymmetrically eroded glenoids.[13,19]

This study addressed the under-implant bone strain and density as the result of physiologic joint loading of augmented glenoid components at the initial time of glenoid component fixation. The load chosen represents a joint load at 75° of abduction, representing 85% body weight, collected during *in-vivo* joint loading.[2] This net joint load vector is consistent with similar FE studies.[10] In future biomechanical simulations, loading should be varied in both magnitude and direction in order to assess variations in load transfer from the implant to the bone under a full range of arm positions and net applied load vectors.

One strength of this study is that we used a computational model of a scapula with advanced primary glenohumeral arthritis and posterior glenoid erosion that clinically required a similar treatment method. Due to the inherent alteration in bone density distribution, which is characteristic of this joint morphology,[13,19] this model may more accurately reflect the actual bone loading scenario that is imposed by the loading of optimally placed augmented glenoid components. Similar studies have decreased the bone density of ‘normal joints’ to simulate the osteoarthritic joint,[10,17] but it is likely that these models do not possess the bone density distribution patterns seen in asymmetrically eroded glenoids. The results of the current study are important in the understanding of early implant fixation techniques and conservative reaming strategies used to preserve high quality underlying bone to ensure the implant achieves effective fixation for its lifespan.

A possible limitation of this study is that we chose to address a single maximal loading case. The magnitude and direction of the joint load vector varies by individual, arm position, soft tissue strength and implant position. This study's representation of a time-zero loading case does not capture these variations. Furthermore, the implant designs chosen in this study represent an average of commercially available augmented component designs and were created to match this patient's anatomy. It is expected the implant designs are a conservative approximation of the actual stress and strain distributions that the underlying bone would experience with commercially available implants; as commercially available implants may not fully conform to the patients morphological joint. It is recommended that the full range of net joint load vectors be assessed on a cohort of type B2 eroded glenoids to provide more robust conclusions in preliminary results achieved during this study.

The results suggest that underlying glenoid bone strains may not be a function of bone density when augmented glenoid components are loaded under the current conditions. This may suggest that the preservation of the densest bone is not essential to the early support of glenoid components, and that the load transfer to the underlying bone is complex and the result of multiple factors. It is expected that as time progresses, underlying bone may remodel as a function of the induced strain field, adaptively reacting to the altered loading environment. It can be inferred that an augmented component design should be chosen that provides the most uniform strain distribution in the underlying bone to prevent bone resorption and possible premature failure. Furthermore, as each individual's morphology differs, the backside design should be chosen that preserves the most glenoid bone stock to ensure the fixation is not compromised for future revision surgeries.

5.5 REFERENCES:

1. Austman RL, Milner JS, Holdsworth DW, Dunning CE. Development of a customized density–modulus relationship for use in subject-specific finite element models of the ulna. Proc Inst Mech Eng Part H J Eng Med2009;223(6):787–794. doi:10.1243/09544119JEIM553

2. Bergmann G, Graichen F, Bender a, Kääb M, Rohlmann a, Westerhoff P. In vivo glenohumeral contact forces--measurements in the first patient 7 months postoperatively. J Biomech 2007;40(10):2139–49. doi:10.1016/j.jbiomech.2006.10.037

3. Bergmann G, Graichen F, Bender a, Rohlmann a, Halder a, Beier a, et al. In vivo gleno-humeral joint loads during forward flexion and abduction. J Biomech 2011;44(8):1543–52. doi:10.1016/j.jbiomech.2011.02.142

4. Beuckelaers E, Jacxsens M, Van Tongel A, De Wilde LF. Three-dimensional computed tomography scan evaluation of the pattern of erosion in type B glenoids. J Shoulder Elbow Surg 2014;23(1):109–16. doi:10.1016/j.jse.2013.04.009

5. Carter D, Hayes W. The compressive behavior of bone as a two-phase porous structure. J Bone Jt Surg 1977;59(7):954-962

6. Chang N, Bellare A, Cohen R., Spector M. Wear behavior of bulk oriented and fiber reinforced UHMWPE. Wear 2000;241(1):109–117. doi:10.1016/S0043-1648(00)00393-8

7. Clavert P, Millett PJ, Warner JJP. Glenoid resurfacing: what are the limits to asymmetric reaming for posterior erosion? J. Shoulder Elbow Surg 2007;16(6):843–8. doi:10.1016/j.jse.2007.03.015

8. Denard PJ, Walch G. Current concepts in the surgical management of primary glenohumeral arthritis with a biconcave glenoid. J Shoulder Elbow Surg 2013;22(11):1589–98. doi:10.1016/j.jse.2013.06.017

9. Gunther SB, Lynch TL, O’Farrell D, Calyore C, Rodenhouse A. Finite element analysis and physiologic testing of a novel, inset glenoid fixation technique. J Shoulder Elbow Surg 2012;21(6):795–803. doi:10.1016/j.jse.2011.08.073

10. Hermida J. Augmented wedge-shaped glenoid component for the correction of glenoid retroversion: a finite element analysis. J Shoulder Elbow Surg 2014;23(3):347-354

11. Kersten AD, Flores-Hernandez C, Hoenecke HR, D'Lima DD. Posterior augmented glenoid designs preserve more bone in biconcave glenoids. J Shoulder Elbow Surg 2014:In-Press doi:10.1016/j.jse.2014.12.007

12. Knowles N, Keener J. Quantification of the position, orientation, and surface area of bone loss in type B2 glenoids. J Shoulder Elbow Surg 2015;24(4):503-510

13. Knowles NK, Athwal GS, Keener JD, Ferreira LM. Regional bone density variations in osteoarthritic glenoids : a comparison of symmetric to asymmetric (type B2) erosion patterns. J Shoulder Elbow Surg 2014;1–8 doi:10.1016/j.jse.2014.07.004

14. Knowles NK, Ferreira LM, Athwal GS. Augmented glenoid component designs for type B2 erosions : a computational comparison by volume of bone removal and quality of remaining bone. J Shoulder Elbow Surg. 2015;1–9. doi:10.1016/j.jse.2014.12.018

15. Nowak DD, Bahu MJ, Gardner TR, Dyrszka MD, Levine WN, Bigliani LU, et al. Simulation of surgical glenoid resurfacing using three-dimensional computed tomography of the arthritic glenohumeral joint: the amount of glenoid retroversion that can be corrected. J. Shoulder Elbow Surg 2009;18(5):680–8. doi:10.1016/j.jse.2009.03.019

16. Nowak DD, Gardner TR, Bigliani LU, Levine WN, Ahmad CS. Interobserver and intraobserver reliability of the Walch classification in primary glenohumeral arthritis. J. Shoulder Elbow Surg 2010;19(2):180–3. doi:10.1016/j.jse.2009.08.003

17. Patel R, Wright T, Gao Y. Load transfer after cemented total shoulder arthroplasty. J Shoulder Elbow Surg 2014; In-Press

18. Saikko V. Wear and friction properties of prosthetic joint materials evaluated on a reciprocating pin-on-flat apparatus. Wear 1993;166(2):169–178. doi:10.1016/0043-1648(93)90259-O

19. Simon P, Gupta A, Pappou I, Hussey MM, Santoni BG, Inoue N, et al. Glenoid subchondral bone density distribution in male total shoulder arthroplasty subjects with eccentric and concentric wear. J Shoulder Elbow Surg;1–9. doi:10.1016/j.jse.2014.06.054

20. Terrier a, Ston J, Larrea X, Farron a. Measurements of three-dimensional glenoid erosion when planning the prosthetic replacement of osteoarthritic shoulders. Bone Joint J 2014;96-B(4):513–8. doi:10.1302/0301-620X.96B4.32641

21. Terrier A, Büchler P, Farron A. Bone–cement interface of the glenoid component: stress analysis for varying cement thickness. Clin Biomech 2005;20(7):710-717

22. Walch G, Badet R, Boulahia A, Khoury A. Morphologic study of the Glenoid in primary glenohumeral osteoarthritis. J Arthroplasty 1999;14(6):756–760. doi:10.1016/S0883-5403(99)90232-223. Walch G, Moraga C. Results of anatomic nonconstrained prosthesis in primary osteoarthritis with biconcave glenoid. J Shoulder Elbow Surg 2012;21(11):1526-1533

24. Walch G, Young A, Boileau P. Patterns of loosening of polyethylene keeled glenoid components after shoulder arthroplasty for primary osteoarthritis. J Bone Joint Surg 2012;94(2):145-150

25. Zhang J, Yongpravat C, Kim H. Glenoid articular conformity affects stress distributions in total shoulder arthroplasty. J Shoulder Elbow Surg 2013;22(3):350-356

CHAPTER 6 – GENERAL DISCUSSION AND CONCLUSIONS

OVERVIEW: *This chapter will re-evaluate the objectives and hypothesis of this research and place this work in the context of the current literature. The need for an understanding of glenoid morphology and impact of the research is briefly discussed. General strengths and limitations are addressed and future directions are presented.*

6.1 SUMMARY

An understanding of the morphology of the osteoarthritic (OA) glenohumeral joint provides essential knowledge to guide the surgical management of joint replacements and may assist in the design of prosthetic devices. Although the prevalence of glenohumeral osteoarthritis is increasing,[4] long-term outcomes for joint replacement has been concerning.[5,6,20] Current surgical techniques are focused on conservative reaming and bone preserving implant designs. These methods are important to conserve the integrity of the joint; however, little research has been done to guide glenoid preparation related to osteoarthritic joint morphology. Furthermore, posteriorly eroded glenoids present one of the most challenging and commonly revised shoulder morphologies.[6,18,20] This thesis focused on improving the body of knowledge associated with the OA glenoid, by exploring regional bone density variations (Chapter 2), characterizing joint morphology (Chapter 3), quantifying bone removal following virtual implantation of augmented glenoid components (Chapter 4), and correlating the under-implant bone strain field to bone density (Chapter 5).

Despite studies that have assessed bone density in normal glenoids[9,10,14,21] and preliminarily so in arthritic glenoids[3], there is a lack of data pertaining to the distribution of bone density in the glenoid to guide surgical reaming in OA glenoids. The majority of glenoids requiring glenoid component replacement are arthritic, creating a large gap in current knowledge. Chapter 2 focused on the two most common OA joint morphologies that require glenoid component replacement – symmetric (Walch type A1 and A2) and asymmetric (Walch type B2).[17] Reaming techniques must be altered in these two morphologies due to the acquired retroversion in asymmetrically eroded glenoids; however, the extent to which this affects underlying bone quality was previously unknown. To measure bone quality in a consistent manner, a quadrant coordinate system was used to assess regional variations at two depths from the glenoids articular surface. In these regions, bone density and void fraction was measured to assess the quality of bone for early implant stability, support and fixation. As hypothesized, symmetrically eroded glenoids had uniform bone density across the glenoid quadrants, likely due to the uniform humeral contact patterns. In contrast, as expected, asymmetrically eroded glenoids had the highest bone density in the posteroinferior quadrant, due to the altered joint stress caused by altered joint kinematics. This was also observed when neoglenoid and paleoglenoid regions were compared. These results are consistent with a similar study that was published concurrently.[15]

Expanding on asymmetrically eroded glenoids, Chapter 3 quantified the morphology of these joints. We hypothesized that current augmented glenoid components, which act to minimize bone removal, may not fully account for posteriorly eroded bone in these cases. Previous studies have assessed posterior erosion of the glenoid as related to the position and orientation of maximum erosion,[1,16] and have assessed the level of joint medialization required for placement of standard and augmented glenoid components.[12,13] However, there is no literature to assist in the placement of the glenoid component in a clinically utilizable method. Using a similar coordinate system to Chapter 2, the angle and position of the erosion in asymmetrically eroded glenoids were measured. It was found that the angle and position of erosion in asymmetrically eroded glenoids was significantly different from the glenoid’s superoinferior axis and glenoid centre. It was also found that the curvature of the neoglenoid and paleoglenoid differ significantly, further increasing the difficulty in current reaming techniques. Finally, in 35% (19 out of 55) of our cases, we found curved erosion morphologies – a previously unknown characteristic of posteriorly eroded (Walch B2) glenoids. This sub-classification may further increase the difficulty in augmented glenoid design and surgical placement.

Chapter 4 addressed the quality of underlying bone, and amount of bone removal required to optimally place three common augmented glenoid components. The tested components were manufactured to the exact dimensions of commercially available components, and fixation devices were omitted to remove bias in bone removal results. This allowed for comparison based primarily on the backside geometries of different component designs. As expected from the orientation and position of erosion measurements in Chapter 3, the hypothesis that the posterior-wedged glenoid component most closely matched the morphology of asymmetrically eroded glenoids, and therefore, had the least bone removal, was confirmed. We also hypothesized that significant differences would exist in the quality of underlying bone with all component designs, which was also confirmed. A similar concurrent study[8], and another study using surrogate scapulae models showed similar results[11].

Bone quality is assumed to have an effect on early implant support and fixation. There is only one known study that has addressed the biomechanical loading of augmented glenoid components using finite element analysis[8] – focusing on predicted cyclically-loaded bone and cement failure. This study artificially reduced the material properties of a normal non-arthritic scapular model to simulate the bone density in an osteoarthritic joint, which may reduce the accuracy in the actual *in-vivo* strain field imposed in the underlying bone. To address these limitations, the goal of Chapter 5 was to correlate the under-implant bone strain field and bone density using finite element analysis in an osteoarthritic scapular model. Intuitively, strain should be greatest in regions with the lowest bone density. However, due to the complex loading scenario and differences in material stiffness imposed by the augmented glenoid component designs, there was no correlation found between the bone strain field and the bone density. These early results may suggest that preservation of the highest quality bone is not essential for early implant support, under the loading conditions imposed in this finite element study.

The body of knowledge associated with complex glenoid morphology and its affect on glenoid component stability has been greatly improved by fulfilling the objectives of this thesis. Bone density variations that occur in different morphologies of glenoid erosion, differences between erosion patterns and augmented glenoid components, and the loading of these components will assist in the preparation of the glenoid in joint replacement surgeries. Furthermore, the knowledge disseminated from the published articles of this thesis may guide in the further development of glenoid components that are intended to minimize bone removal, optimize fixation, and match patient anatomy so that long-term outcomes for patients undergoing joint replacement surgeries may be improved. Increasing the stability and long-term outcomes for joint replacements surgeries is of utmost importance. With an aging population, reducing the cost associated with these surgeries, primarily the need for revisions surgeries, may significantly reduce future health care costs and improve the lives of patients undergoing these surgical treatments.

6.2 STRENGTHS AND LIMITATIONS

An important strength of this work is the relatively large patient cohorts. Current literature lacks comparisons between individuals with glenoid erosion morphologies. Chapters 2 and 3 represent some of the largest isolated patient cohorts with glenoid erosion (Chapter 2 – 50 patients, Chapter 3 - 55 patients) in the current literature. Evaluation of these larger patient cohorts allows for more robust conclusions based on quantified characteristics of these joint morphologies. This increases the clinical relevance and potential impact of the results presented, and the ability to positively impact surgical intervention and implant design.

The virtual implantation method of augmented glenoid components to match the precise dimensions of currently available components (Chapter 3), illustrates the effectiveness of using three-dimensional surgical planning to guide in the optimal placement of glenoid components. This method not only improves component placement, but allows for the quality and amount of remaining bone to be analyzed – a practice which cannot be achieved intra-operatively or with current pre-operative techniques. The complex relationship between glenoid morphology and augmented glenoid component geometries revealed how difficult it is to achieve optimal placement. This method also has the potential to significantly improve clinical placement.

Evaluating density on the basis of Hounsfield Units (HU), as described in Chapter 2 and Chapter 4, allow for reproducible characterization of bone density using clinically available computed tomography scans. This may allow for a more direct method to quantify bone quality and allow surgeons to modify surgical planning based on each patient’s individual density distribution. However, with this method’s strengths there are also weaknesses. Firstly, clinical patient computed tomography (CT) scans are typically collected at a common energy to reduce unnecessary radiation exposure to the patient, with the HU for a specific scanner being consistent at a given energy. In this thesis, the scans were collected retrospectively and with multiple CT scanners, creating some uncertainty in the bone density measurements collected on different scanners. Ideally, a CT calibration phantom scanned along with the patient should be used to calibrate HU and bone density – decreasing patient variability; however this is not possible in retrospective analysis. Scanning of a calibration phantom or consistency in CT scanners is recommended for future bone density comparisons.

At the time bone density measurements were collected little literature existed on the minimum bone density required to classify cancellous bone in the glenoid. In the segmentation of adjoining bones, a minimum threshold must be used to ensure accurate separation is achieved between each bone. We chose to use a minimum threshold of 200 HU,[2,9,21] and classified bone below this threshold as ‘low quality cancellous bone or voids.’ It became apparent from the large void fraction values in Chapters 2 and 4, and further evaluation of patient CT scans, that a lower threshold should have been chosen for the cancellous value. This limitation also stems from the lack of a validated density-modulus relationship for the OA glenoid. It is recommended that mechanical testing of glenoids and comparison with CT data be completed in the future to determine a minimum threshold value of cancellous bone for future studies.

Finally, the lack of the validated density-modulus relationship for the OA glenoid provides a limitation in the finite element analysis of the glenoid (Chapter 5). The equation chosen is sensitive to small changes in cancellous bone density, but is non-specific to the glenoid, especially the OA glenoid. Since comparisons are made in the same scapular model in this study, the accuracy of the bone density-modulus relationship is less significant. However, future studies making comparisons between multiple patient models should use a validated density-modulus relationship, to increase the accuracy and reduce variability in results. A final limitation of the FE study is the *in-vivo* joint loading used. The load chosen in this study represents a single net joint vector that may not be specific to this patient. Ideally, a variety of net joint vectors should be simulated to produce a bone strain field that is representative of all loading scenarios the bone and implants may undergo.

6.3 CURRENT AND FUTURE DIRECTIONS

Through the fulfillment of the objectives of this thesis, many opportunities became apparent for future work. Improvements to glenoid preparation, fixation, support, and glenoid component design may significantly improve the long-term outcomes for patients requiring joint replacement. Chapters 1 and 2 presented concerning differences in the apparent strength of underlying bone, and the morphology of the joint due to osteoarthritis. These results indicate that glenoid components may have improved long-term outcomes if fixation was optimized to each patients underlying bone density distribution. Similarly, if glenoid components more closely matched each patient’s morphological joint, underlying bone may be preserved, further increasing component stability. Patient-specific analysis and component design is now possible with the imaging modalities in modern hospitals, the associated software, and knowledge, and should be the end goal of current research as related to this thesis.

When virtually implanting commercially available augmented glenoid components, significant differences in bone densities were found in neoglenoid and paleoglenoid regions. It was also found that slight morphological variations of the glenoid were often better corrected with one glenoid design than another. It is therefore recommended that virtual implantation of glenoid components is utilized to quantify bone removal and optimize component placement. Virtual implantation allows for reproducible implant placement on three-dimensional reconstructions of patient anatomy. Pre-operative surgical planning can be optimized by choosing the best implant size and augment for each patient's individual morphology, minimizing volumetric bone removal. This method preserves the densest subchondral bone, improving implant fixation, thereby reducing implant subsidence and migration. Pre-operative planning software may significantly improve the positioning of implants and ensures that intra-operative implant placement is optimized to implant design.

The parametric augmented glenoid components proposed in Chapter 5 were designed to minimize bone removal, specifically in the posteroinferior quadrant, which was found to have the densest bone. This design ensures adequate underlying bone support, and allows for the implant to be lateralized – factors that may improve the stability of the component and the joint. Although correlations were not found between underlying bone density and the strain field using the specific loading scenario analyzed, the finite element (FE) method provides a vast amount of data that can be used to improve component design, support and fixation methods. However, a validated bone density-modulus equation does not exist for the glenohumeral joint, and it is essential to the improvement of shoulder finite element models for this validation to be performed. Cadaveric mechanical testing on a variety of shoulders must be utilized in order to validate an equation that can more accurately provide a comprehensive evaluation of the loading distribution in bone.

Once this model exists, patient-specific evaluations of glenoid implantation can be virtually completed pre-operatively. Simulations of bone remodeling, long-term cyclic loading and multiple material evaluations available using current FE techniques may increase the physiological applicability of computer simulations and allows for multiple loading scenario's and conditions to be evaluated. This patient-specific evaluation has the potential to significantly improve positive patient outcomes, reduce intra-operative time, and decrease revision surgeries. Patient-specific glenoid component placement studies have been recently reported in the literature,[7,19] showing early success, indicating that patient-specific analysis should become the normal standard of care for patients requiring joint replacements.

6.4 CONCLUSIONS

The work presented in this thesis demonstrates that symmetrically eroded glenoids have uniform bone density distribution, while asymmetric eroded glenoids have significant and potentially important regional variations (Chapter 2). In asymmetricaly eroded cases, quantifying the posterior bone loss (Chapter 3) along with the bone density may allow for conservative reaming techniques to be optimized, and glenoid components to be designed that minimize bone removal and optimize bone fixation and support.

The virtual implantation method used to align current augmented glenoid components (Chapter 4) illustrates the need for a similar method to be utilized in pre-operative planning, in order to optimize component placement and choose a component that minimizes bone removal and optimizes quality underlying bone. As glenoid component design improves and virtual techniques are optimized, the finite element method (Chapter 5) allows for a comprehensive evaluation of the loading scenario imposed throughout the components lifetime. This may allow for patient-specific devices to be utilized, and has the potential to vastly improve long-term outcomes for patients requiring total shoulder arthroplasty.

6.5 REFERENCES

1. Beuckelaers E, Jacxsens M, Van Tongel A, De Wilde LF. Three-dimensional computed tomography scan evaluation of the pattern of erosion in type B glenoids. J Shoulder Elbow Surg 2014;23(1):109–16. doi:10.1016/j.jse.2013.04.009

2. Bryce CD, Pennypacker JL, Kulkarni N, Paul EM, Hollenbeak CS, Mosher TJ, et al. Validation of three-dimensional models of in situ scapulae. J Shoulder Elbow Surg2008 Jan;17(5):825–32. doi:10.1016/j.jse.2008.01.141

3. Couteau B, Mansat P, Mansat M, Darmana R, Egan J. In vivo characterization of glenoid with use of computed tomography. J Shoulder Elbow Surg 2001;10(2):116–22. doi:10.1067/mse.2001.112884

4. Day JS, Lau E, Ong KL, Williams GR, Ramsey ML, Kurtz SM. Prevalence and projections of total shoulder and elbow arthroplasty in the United States to 2015. J Shoulder Elbow Surg 2010;19(8):1115–20. doi:10.1016/j.jse.2010.02.009

5. Denard PJ, Raiss P, Sowa B, Walch G. Mid- to long-term follow-up of total shoulder arthroplasty using a keeled glenoid in young adults with primary glenohumeral arthritis. J Shoulder Elbow Surg 2013;22(7):894–900. doi:10.1016/j.jse.2012.09.016

6. Gerber C, Costouros J. Static posterior humeral head subluxation and total shoulder arthroplasty. J Shoulder Elbow Surg 2009;18(4):505-510

7. Hendel M, Bryan J. Comparison of Patient-Specific Instruments with Standard Surgical Instruments in Determining Glenoid Component Position: A Randomized Prospective Clinical Trial. J Bone Joint Surg 2012; 94(23):2167-2175

8. Kersten AD, Flores-Hernandez C, Hoenecke HR, D'Lima DD. Posterior augmented glenoid designs preserve more bone in biconcave glenoids. J. Shoulder Elbow Surg 2015; In-Press. doi:10.1016/j.jse.2014.12.007

9. Kraljević M, Zumstein V. A comparison of subchondral bone mineralization between the glenoid cavity and the humeral head on 57 cadaverous shoulder joints. Surg Radiol 2013; 35(4):295-300. doi:10.1007/s00276-012-1034-8

10. Mochizuki Y, Natsu K, Kashiwagi K, Yasunaga Y, Ochi M. Changes of the mineralization pattern in the subchondral bone plate of the glenoid cavity in the shoulder joints of the throwing athletes. J Shoulder Elbow Surg 2005;14(6):616–9. doi:10.1016/j.jse.2005.02.016

11. Roche C, Diep P. Biomechanical Impact of Posterior Glenoid Wear on Anatomic Total Shoulder Arthroplasty. Bull Hosp Joint Disease 2013;71:S5-11

12. Sabesan V, Callanan M, Sharma V, Iannotti JP. Correction of acquired glenoid bone loss in osteoarthritis with a standard versus an augmented glenoid component. J Shoulder Elbow Surg 2014;23(7):964–73. doi:10.1016/j.jse.2013.09.019

13. Sabesan V, Callanan M, Sharma V. Guidelines for the selection of optimal glenoid augment size for moderate to severe glenohumeral osteoarthritis. J Shoulder Elbow Surg 2014;23(7):974–81. doi:10.1016/j.jse.2013.09.022

14. Schulz CU, Pfahler M, Anetzberger HM, Becker CR, Müller-Gerbl M, Refior HJ. The mineralization patterns at the subchondral bone plate of the glenoid cavity in healthy shoulders. J Shoulder Elbow Surg 2002;11(2):174–181. doi:10.1067/mse.2002.121635

15. Simon P, Gupta A, Pappou I, Hussey MM, Santoni BG, Inoue N, et al. Glenoid subchondral bone density distribution in male total shoulder arthroplasty subjects with eccentric and concentric wear. J Shoulder Elbow Surg 2014;1–9. doi:10.1016/j.jse.2014.06.054

16. Terrier a, Ston J, Larrea X, Farron a. Measurements of three-dimensional glenoid erosion when planning the prosthetic replacement of osteoarthritic shoulders. Bone Joint J 2014;96-B(4):513–8. doi:10.1302/0301-620X.96B4.32641

17. Walch G, Badet R, Boulahia A, Khoury A. Morphologic study of the Glenoid in primary glenohumeral osteoarthritis. J Arthroplasty 1999;14(6):756–760. doi:10.1016/S0883-5403(99)90232-2

18. Walch G, Moraga C, Young A, Castellanos-Rosas J. Results of anatomic nonconstrained prosthesis in primary osteoarthritis with biconcave glenoid. J Shoulder Elbow Surg 2012;21(11):1526–33. doi:10.1016/j.jse.2011.11.030

19. Walch G, Vezeridis P, Boileau P. Three-dimensional planning and use of patient-specific guides improve glenoid component position: an in vitro study. J Shoulder Elbow Surg 2014; In-Press

20. Walch G, Young A, Boileau P. Patterns of loosening of polyethylene keeled glenoid components after shoulder arthroplasty for primary osteoarthritis. J Bone Joint Surg 2012;94(2):145-150

21. Zumstein V, Kraljević M, Müller-Gerbl M. Glenohumeral relationships: subchondral mineralization patterns, thickness of cartilage, and radii of curvature. J Orthop Res 2013;31(11):1704–7. doi:10.1002/jor.22425

APPENDIX A – GLOSSARY OF MEDICAL TERMINOLOGY

__OVERVIEW:__ The following lists definitions and terminology common to the medical field used throughout this thesis.

Anterior – Towards the front of the body.

Apparent Density – Mass of mineralized tissue per total volume

Arthropathy – refers to the disease of a joint.

Arthroplasty – A surgical procedure to restore the native function of a joint.

Attenuation – loss of intensity through a medium.

Axial – Plane separating the body into cranial and caudal (head and tail) regions. Also known as the transverse plane.

Coronal – Plane separating the body into dorsal and ventral (or anterior and posterior) regions. Also known as the frontal plane.

Distal – Furthest from the body along a limb.

Excise – to remove.

Heterogeneous – A diverse and non-uniform distribution of properties.

Homogeneous – A uniform distribution of properties.

Homeostasis – regulation of the normal stability of a system.

Hounsfield Units – A linear transformation of the linear attenuation coefficient used to calibrate the radiodensity in Computed Tomography scanners.

Idiopathic – Of unknown cause.

Implant – An engineered replacement joint which is fixed to the articular surface of the joint.

Intra-Operative – During surgery.

Lateral – Further from the midline of the body.

Medial – Closest to the midline of the body.

Migration – Displacement from the original fixed position.

Morphology – Alteration to the native form and structure.

Osteoarthritis – Deficiency of a joint characterized by inflammation and articular cartilage degeneration.

Posterior – Towards to the rear of the body.

Pre-Operative – Before surgery.

Proximal – Closest to the body along a limb.

Resorption – The breakdown of bone releasing minerals into the blood.

Radiation Dose – The level of ionizing radiation absorbed by a patient.

Radiodensity – the inability of X-rays to pass through a medium.

Sagittal – Plane separating the body into right and left halves.

Subchondral – The bone directly below the articular cartilage (“chondral”) layer.

Subluxation - Incomplete or partial dislocation of a joint.

APPENDIX B - DENSITY AND POROSITY MEASUREMENT PROTOCOL IN MIMICS®

> ***OVERVIEW:*** *The following reports on the protocol to measure density of multiple glenoid regions and the method to generate data for void fraction calculations. The protocol shown here incorporates the quadrant method; however, the same steps are used when separating the quadrant into anterior and posterior facets.*

Step 1: Segmenting and Thresholding CT DICOM Images

A. Load the CT DICOM files to Mimics® using the "new project wizard." DICOM files are from the native CT patient scans and have the file extension .dcm. Press Ctrl + N to access the "new project wizard."

B. Threshold the loaded images using a minimum Hounsfield value of 200 HU. Press Segmentation → Thresholding. Leave all boxes unchecked.

C. Manually remove intersecting pixels between the glenoid and humerus. This is often required to be completed slice-by-slice to ensure all intersecting pixels are removed. Press Segmentation → Edit Masks → select Type, Width and Height of pixels to remove and manually remove in CT views.

D. Segment the scapula. Press Segmentation → Region Growing → select "Threshold" as the Source and "New Mask" as the Target. Leave all other buttons as default. Rename the mask as desired. If the humerus is included in the "New Mask," additional intersecting pixels must be removed and the process repeated.

Step 2: Three-Dimensional Model Creation and Quadrant Formation

E. Select the scapula mask and create 3D model. Press Segmentation → Calculate 3D → select desired mask → select optimal and click calculate. The 3D model should now appear in the bottom right window and in the "3D Objects" tab on the right.

F. On the glenoid face of the 3D reconstructed model insert CAD points on the superior and inferior aspects of the surface (Figure B.1). Press Medcad → Point → Draw, and select on the 3D model.

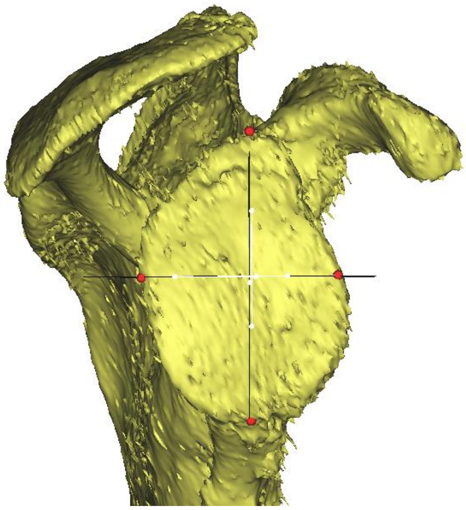

Figure B.1: Three-Dimensional Scapula Reconstruction with Quadrant Planes

G. Measure the distance between the superior and inferior points using the built-in linear measurement tools. Press Measurements → Measure Distance. At the mid-point of this line draw a perpendicular line posterior to anterior. Place CAD points at the anterior and posterior aspects as in step F.

H. Define two planes to separate the glenoid into quadrants; i) superior to inferior and ii) posterior to anterior (Figure B.1). Press Medcad → Plane → Draw. Select the superior, inferior and intersection of two lines (glenoid centre) as the three points to define the plane. If the desired angle of the plane is not achieved, repeat. Repeat for a perpendicular plane using the posterior, centre and anterior points.

Step 3: Re-Slicing Images and Creating Quadrant Masks

I. Re-slice the images separately anterior and posterior. Press File → Online Reslice → Along Plane → Create Plane. Choose the superior, inferior and anterior points. Ensure the re-sliced images are parallel to the version angle of the anterior region and name the re-sliced image plane "anterior." Repeat for the posterior plane.

J. Using the anterior re-sliced images, scroll through the sagittal slices until the most medial point in the glenoid dish is found. This may be simplified by visualizing the slices on the 3D reconstructed model. Measure 2.5 and 5 mm from this point in the sagittal slices and record the slice numbers.

K. Remove (manually edit) all of the highlighted pixels one slice medial to the slice 5 mm from the glenoid surface. Using the quadrant planes as a reference, manually remove all the pixels along the edges of the posterior-superior (P-S) quadrant (Figure B.2). Continue through each sagittal slice moving laterally toward the glenoid surface. Once all pixels have been removed, segment the P-S quadrant as previously described. Repeat for the posterior-inferior (P-I), anterior-superior (A-S), and anterior-inferior (A-I) quadrants. Note that for the anterior quadrants the "anterior" re-sliced images should be used. There should now be four masks that when combined re-create the entire glenoid 5 mm from the most medial point of the glenoid (Figure B.3).

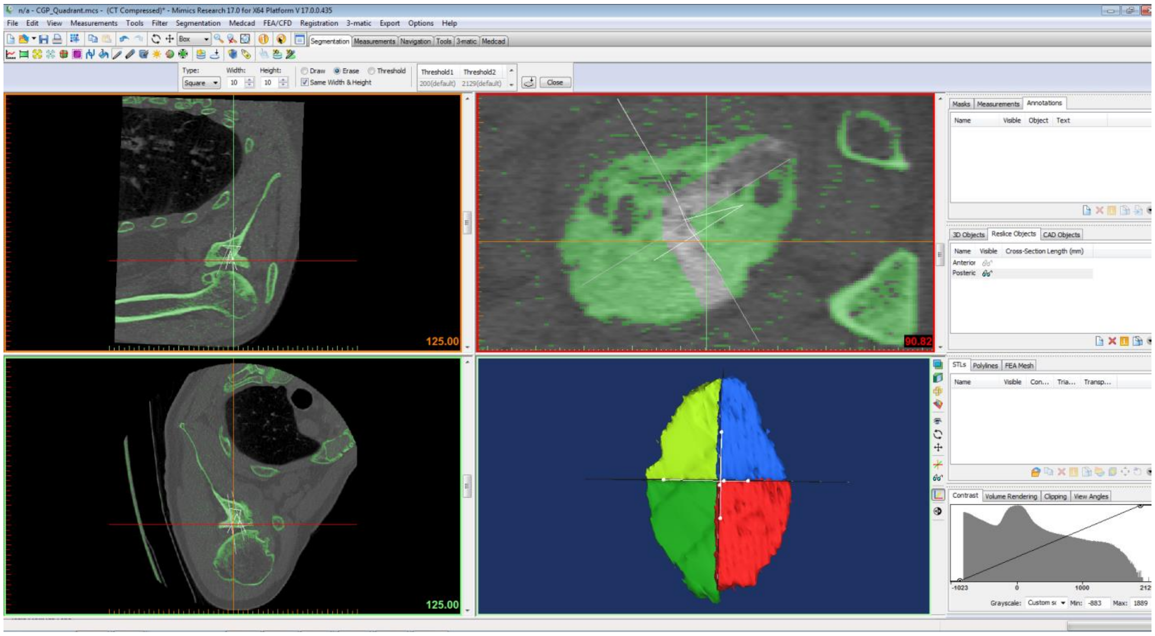

Type: Square
Width: 10
Height: 10
○ Draw ● Erase ○ Threshold
☑ Same Width & Height
Threshold1 200(default)
Threshold2 2129(default)
Grayscale: Custom Min: -883 Max: 1889

Figure B.2: Editing of threshold mask to create quadrant masks

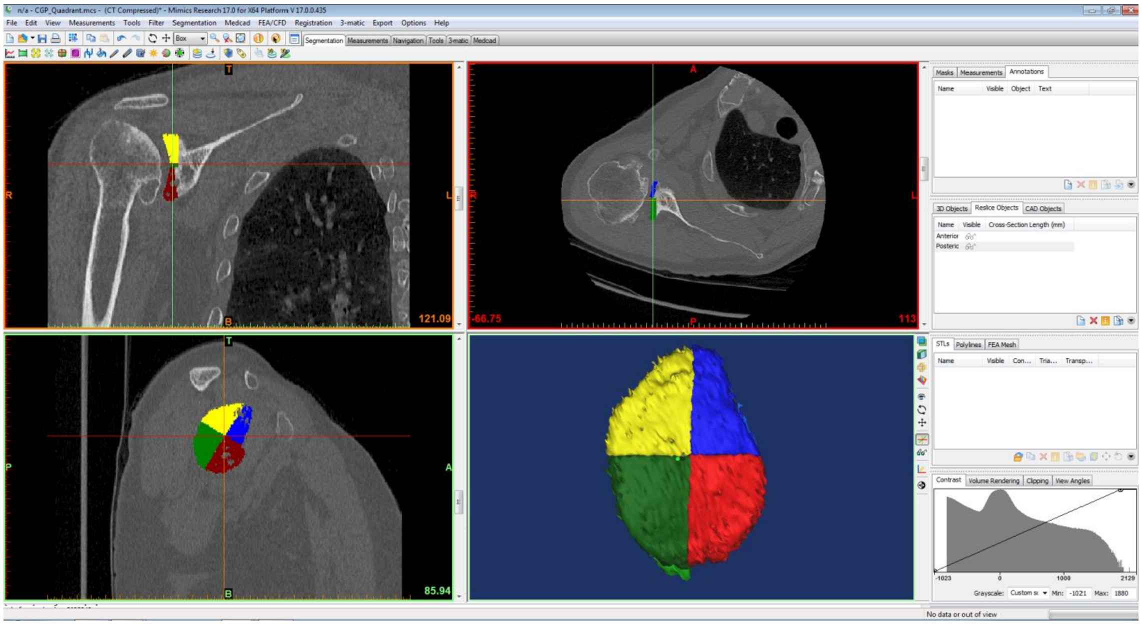

Grayscale: Custom Min: -1021 Max: 1880

Figure B.3: Mimics® view of unfilled quadrant mask formation for volume and density measurements.

J. Copy the 5 mm mask (to form two identical masks) and remove all pixels from the slice one slice medial to the previously defined 2.5 mm slice. Use the region growing function to create a new mask. Repeat for all four quadrants. There should now be four masks that represent the quadrants from 2.5 mm to the lateral surface of the glenoid.

K. Perform a Boolean subtraction of the 2.5 mm mask from the 5 mm mask for each quadrant. Press Segmentation → Boolean Operations → select the 5 mm mask as Mask A and the 2.5 mm mask as Mask B → select the minus Operation and the "New Mask" as the Result. Repeat for each quadrant. There should now be four masks that represent the quadrants from 2.5 to 5 mm from the glenoid surface (Figure B.4).

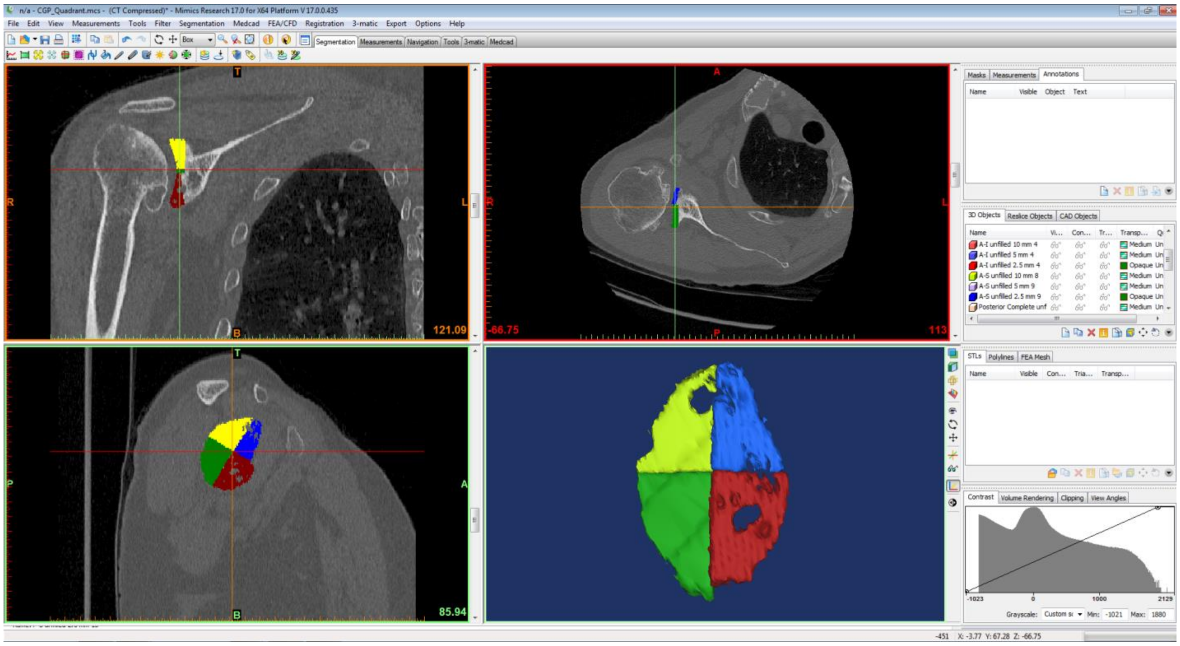

Name	Vi...	Con...	Tr...	Transp...
A-I unfilled 10 mm 4				Medium
A-I unfilled 5 mm 4				Medium
A-I unfilled 2.5 mm 4				Opaque
A-S unfilled 10 mm 8				Medium
A-S unfilled 5 mm 9				Medium
A-S unfilled 2.5 mm 9				Opaque
Posterior Complete unf				Medium

Figure B.4: Mimics® view of unfilled quadrant mask formation for volume and density measurements. Note the porosity of bone in the 3D reconstructed 2.5 - 5 mm regions.

Step 4: Recording Mask Volume and Average Density

L. Select each mask and record the mask volume and average density (Note if the density units are not in HU select Options → Preferences → select Hounsfield as the pixel unit). Right-click the desired mask → select properties. There should be recorded values for eight masks; four quadrants and two depths at each quadrant.

M. Manually fill all holes in each of the previous eight masks using the manual editing tools (Figure B.5).

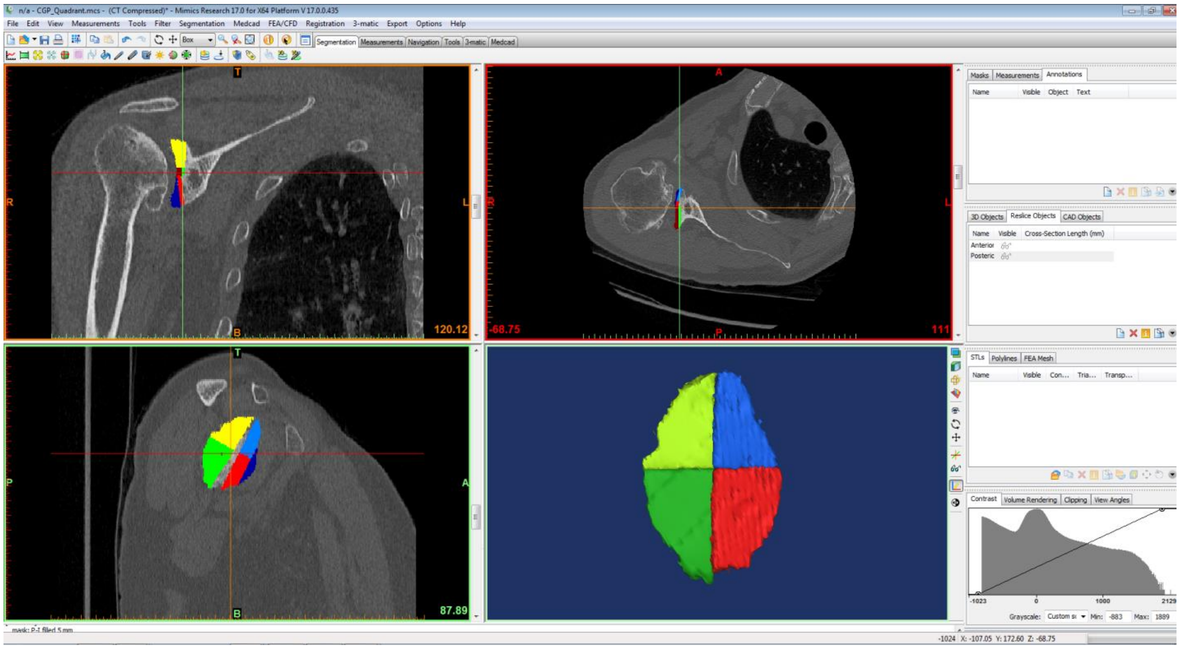

Figure B.5: Mimics® view of filled quadrant mask formation for volume and density measurements. Note the filled porous areas of bone in the 3D reconstructed 2.5 - 5 mm regions.

N. Select each mask and record the mask volume and average density as in step L.

O. Repeat protocol for additional patients.

APPENDIX C - MIMICS® THREE-DIMENSIONAL POINT EXTRACTION, 3-MATIC® SURFACE AREA AND MATLAB® PROTOCOL FOR GLENOID EROSION MEASUREMENTS

OVERVIEW: *The following reports on the protocol to measure the position, orientation, surface area and radii of curvature of glenoid erosion in asymmetrically eroded glenoids. Points are extracted from three-dimensional stereolithography models generated in Mimics® and measurements are performed using custom written mathematical algorithms in Matlab®. The code is broken down into steps in order to explain and simplify the analysis; however, as a whole, the code will output all the required figures and data when executed.*

Step 1: Extracting Three-Dimensional Point Coordinates from Mimics® on the Glenoid and Humerus

A. Segment the scapula and humerus as described in Appendix B, and create three-dimensional (3D) stereolithography (STL) models of the scapula and the humerus.

B. On the glenoid face of the 3D reconstructed model insert CAD points on the superior and inferior aspects of the surface. Press Medcad → Point → Draw, and select on the 3D model. Use the same procedure to place ten points along the visible erosion. This may require rotating the 3D to adjust the lighting. Rename the points as desired.

C. Again using the Medcad module, place points to fill the surface of the neoglenoid (posterior to the erosion points) and paleoglenoid (anterior to the erosion points)

(See Figure 3.4). Hide the scapula reconstruction and Medcad points on the glenoid by selecting them in the window on the right side of the screen and deselecting the visible button. Show the humerus 3D reconstruction and place points along the neo-articulation of the humeral head (See Figure 3.4).

D. Save the superior, inferior and ten points along the erosion into one text file. Press Export → Txt. In the dialogue box select the desired points and save the file. The output txt file should appear as shown in Figure C.1, where the “Points Name” correspond to the name of your points. The Anterior point is a reference point which is not used in the Matlab code, and points 5 to 14 represent the 3D coordinates of the erosion points in 3D Cartesian coordinates with respect to the global origin.

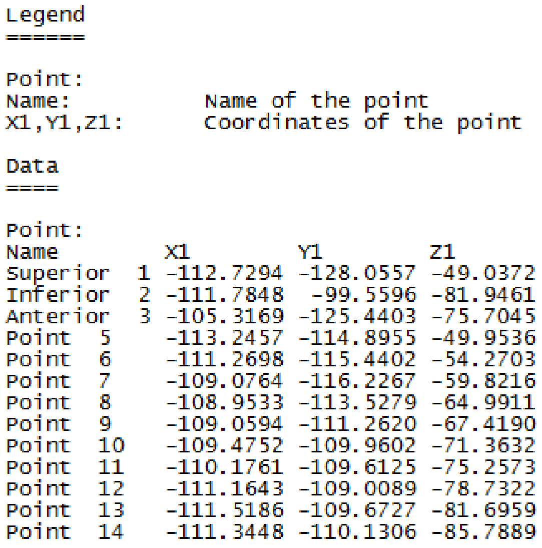

```
Legend
======

Point:
Name:           Name of the point
X1,Y1,Z1:       Coordinates of the point

Data
====

Point:
Name         X1        Y1        Z1
Superior  1 -112.7294 -128.0557 -49.0372
Inferior  2 -111.7848  -99.5596 -81.9461
Anterior  3 -105.3169 -125.4403 -75.7045
Point   5   -113.2457 -114.8955 -49.9536
Point   6   -111.2698 -115.4402 -54.2703
Point   7   -109.0764 -116.2267 -59.8216
Point   8   -108.9533 -113.5279 -64.9911
Point   9   -109.0594 -111.2620 -67.4190
Point   10  -109.4752 -109.9602 -71.3632
Point   11  -110.1761 -109.6125 -75.2573
Point   12  -111.1643 -109.0089 -78.7322
Point   13  -111.5186 -109.6727 -81.6959
Point   14  -111.3448 -110.1306 -85.7889
```

Figure C.1: Example of output txt file with coordinate and erosion point coordinates

E. Repeat step D for the neoglenoid points, paleoglenoid points and the neo-articulation of the humerus points. Save these as separate files as in step D. You should now have four text files for each patient: one file as shown in figure C.1 with the superior, inferior and erosion points, one file with the neoglenoid point cloud, one file with the paleoglenoid point cloud and one file the humerus point cloud.

Step 2: Determining Surface Area of the Neoglenoid and Paleoglenoid using 3-Matic®

F. Copy the 3D STL model of the scapula from Mimics® and ten points along the erosion line and paste in 3-Matic®. This can be accomplished by using the copy and paste feature in Mimics, or keyboard hotkeys (Ctrl-C and Ctrl-V).

G. Using the built-in cropping features, remove the entire scapula to isolate the glenoid.

H. Using the built-in surface marking tools, select the neoglenoid region posterior to the erosion points. Read the surface area measurement from the 'Properties' dialogue box. Use the same procedure to mark the remaining glenoid surface and record the total glenoid surface area. The paleoglenoid surface area is the total surface minus the neoglenoid surface area.

Step 3: Executing the Matlab® Script for Orientation and Position of the Erosion Line

I. Run the script in Matlab®. Ensure the file path for 'data1' and 'T' correspond to the locations of the coordinate/erosion and transformation text files you extracted from Mimics® in Step 1. The program will prompt you to select the points from the text files. Select the desired points and the code will output the R^2 (rsq) of the erosion fit line, distance from centre point of the glenoid and angle between the erosion best fit line and the superoinferior axis.

```
%Interactively select coordinate/erosion data
data1 = uiimport('H:\M.E.Sc Files\Posterior Wear - Erosion Study\Points w-o
Reslice\MU58_Data.txt');%Import data from text file

%Load Transformation Matrix (Auto-generated by Mimics when re-sliced)
```

```
T = dlmread('H:\M.E.Sc Files\Posterior Wear - Erosion Study\Transformation
Matricies\MU58.txt');%Load transformation matrix from Mimics output

%Add column of ones for transformation matrix
for k = 1:length(data1.data)
ones(k) = 1;
end
data = [data1.data(:, 2:4) ones'];

%Transform Points
for j=1:length(data)
trans_points_1 = T'*(data(j,1:4))';
trans_points(j,:) = trans_points_1';
end
S = trans_points(1,1:3);%superior transformed point
I = trans_points(2,1:3);%inferior transformed point
C = (S+I)/2;%centre of glenoid transformed point

%Fit polynomial (order 1) to erosion points (plane is in y-z for sagittal)
temp = polyfit(trans_points(4:13,2),trans_points(4:13,3),1);
[zfit] = polyval(temp,trans_points(4:13,2));

%Coefficient of determination (R^2)
%reference (http://www.mathworks.com/help/matlab/data_analysis/linear-regression.htm
zresid = trans_points(4:13,3) - zfit;
SSresid = sum(zresid.^2);
SStotal = (length(trans_points(4:13,3))-1) * var(trans_points(4:13,3));
rsq = 1 - SSresid/SStotal

%Visulaize the infero-superior line and erosion line in 2D
figure(1)
hold on
plot(trans_points(4:13,2),trans_points(4:13,3),'ro')%erosion points
plot(trans_points(1:2,2),trans_points(1:2,3),'r')%infero-superior axis
plot(trans_points(4:13,2),zfit,'b')%line of best fit
plot(C(1,2),C(1,3),'bx')%centre of glenoid
plot(trans_points(4:13,2),zfit,'rx')%points on best fit line

%Calculate vectors for position and orientation measurements

%Erosion line & infero-superior vectors
LOB_points = [trans_points(4:13,2),zfit];%Points on line of best fit (LOB)
E_P1 = [LOB_points(1,:)];%1st LOB point
E_P2 = [LOB_points(10,:)];%last LOB point
v_E = E_P1 - E_P2;%Erosion vector
v_IS = S(1,2:3) - I(1,2:3);%Infero-superior vector

%Perpendicular distance from glenoid centre to erosion best fit line
E = v_E./norm(v_E); %unit length; E is the erosion line
distance = norm((C(1,2:3)-E_P2)-E*dot(C(1,2:3)-E_P2,E))

%Orientation angle of erosion line w.r.t. infero-superior axis
temp_theta = (acos((dot(v_IS,v_E))/(norm(v_IS)*norm(v_E))) * (180/pi));
```

```
%Change the angle (to account for left and right scapulae) if angle
%exceeds 90 degrees
if temp_theta>90
    theta = 180- temp_theta
else
   theta = temp_theta
end
```

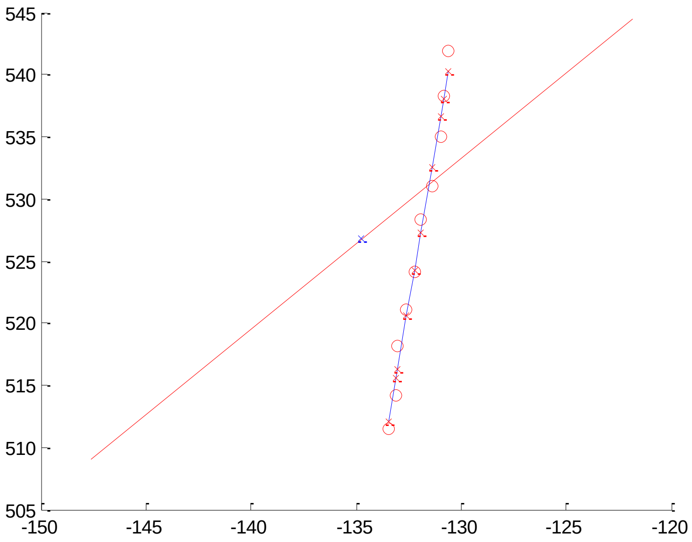

Figure C.2: Output figure of the ten erosion points (red circles), line-of-best-fit (blue line), glenoid centre (blue x), and supero-inferior axis (red line)

Step 4: Executing the Matlab® Script for Characterization of the Erosion using Circle Fitting

J. The following script can be added directly below the previous script and is used to plot and characterize the curvature of the erosion.

```
y=trans_points(4:13,2);%erosion y points
z=trans_points(4:13,3);%erosion z points

%Fit circle to original erosion points
```

```
my = mean(y); mz = mean(z);
Y = y - my; Z = z - mz; % Differences from means
dy2 = mean(Y.^2); dz2 = mean(Z.^2); % variances
t = [Y,Z]\(Y.^2-dy2+Z.^2-dz2)/2; % Solve least mean squares problem
a0 = t(1); b0 = t(2); % t is the 2 x 1 solution array [a0;b0]
r = sqrt(dy2+dz2+a0^2+b0^2); % Calculate the radius
a = a0 + my; b = b0 + mz; % Locate the circle's center
curv = 1/r % Get the curvature

%First and Last Erosion Points
erosion = trans_points(4:13,:);
min_er = min(erosion(:,3));
max_er = max(erosion(:,3));
for w = 1:length(erosion)
    if min_er == erosion(w,3)
        min_er = [erosion(w,2),erosion(w,3)];
    elseif max_er == erosion(w,3)
        max_er = [erosion(w,2),erosion(w,3)];
    end
end

%Polar coordiantes of first and last erosion points (a and b moves origin
%to circle)
[ang_min,rho_min] = cart2pol(min_er(:,1)-a,min_er(:,2)-b);
[ang_max,rho_max] = cart2pol(max_er(:,1)-a,max_er(:,2)-b);
theta = ang_max - ang_min;

%increment for 10 points on circle fit
inc2 = ang_min;
inc1 =0;
for q = 1:10
    inc2 = inc2 + inc1;
    inc1 = theta/10;
    x_circle(q) = a + r*cos(inc2);
    y_circle(q) = b + r*sin(inc2);
end

%Plot Circle Fit

hold on
t2 = 0 : .1 : 2*pi;
y = r * cos(t2) + a;
z = r * sin(t2) + b;
plot(y, z,'b')
plot(x_circle',y_circle','go')

%Characterizing the curvature

C_fit = [x_circle; y_circle]';%10 circle fit points
C_bi = (C_fit(1,:)+C_fit(10,:))/2;%Bisector of min and max circle fit points
plot([C_fit(1,1) C_fit(10,1)],[C_fit(1,2) C_fit(10,2)],'b')
plot(C_bi(1,1),C_bi(1,2),'bo')
plot(a,b,'ro')
rb = pdist([[a,b];C_bi],'euclidean');%Distance from centre of circle to bisector
```

```
ro = r-rb%distance from bisector to outside of circle

%Euclidean distance between max and min original erosion points

Erosion_dist_fit = pdist([C_fit(1,:);C_fit(10,:)],'euclidean')
```

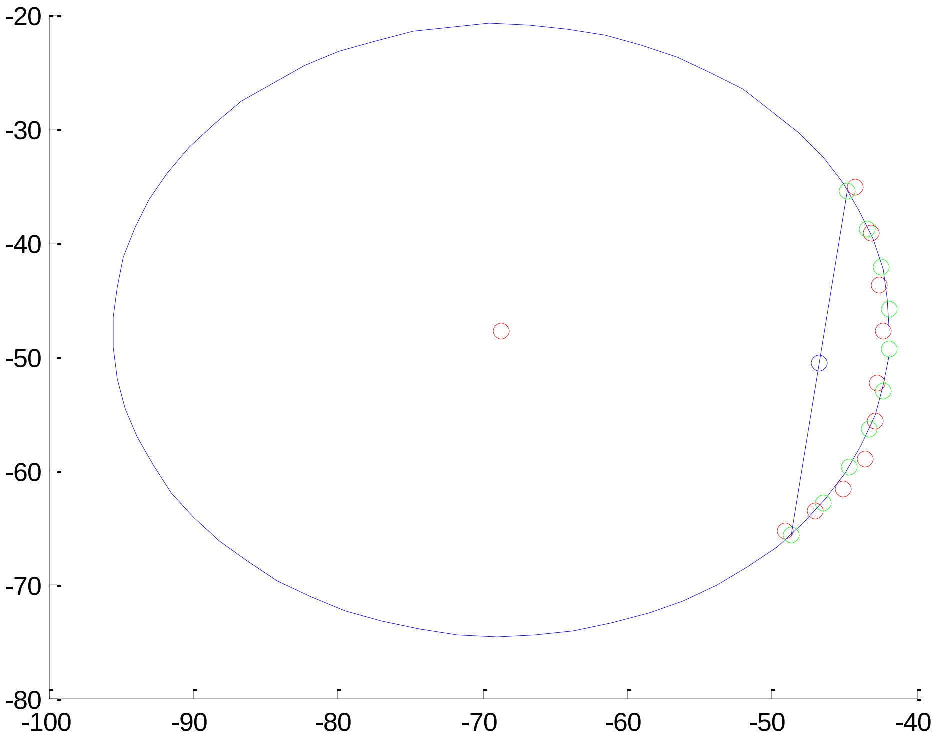

Figure C.3: Erosion circle fit and cord calculated from ten erosion points in Matlab®

Step 5: Executing the Matlab® Script for Radii of Curvature of the Neoglenoid, Paleoglenoid and Neo-Articulation of the Humerus

K. The following script can be added directly below the previous script and is used to plot and characterize the radii of curvature of the neoglenoid, paleoglenoid and humeral head.

```
Interactively select humerus data
temp1 = uiimport('File Path.txt');
%Interactively select neo and paleo data
neo = uiimport('File Path.txt');
paleo = uiimport('File Path.txt');
%Humerus Sphere Fitting
Q = (temp1.data(:, 2:4));
figure(3)
[Center,Radius] = sphereFit(Q);
plot3(Q(:,1),Q(:,2),Q(:,3),'r.')
hold on;daspect([1,1,1]);
[Base_X,Base_Y,Base_Z] = sphere(20);
surf(Radius*Base_X+Center(1),...
    Radius*Base_Y+Center(2),...
    Radius*Base_Z+Center(3),'faceAlpha',0.3,'Facecolor','b')
hum_curv_sph = 1/Radius;
hum_rad = Radius
%Neo and Paleo Sphere Fitting
X = (neo.data(:, 1:3));
figure(4)
[Center,Radius] = sphereFit(X);
plot3(X(:,1),X(:,2),X(:,3),'r.')
hold on;daspect([1,1,1]);
[Base_X,Base_Y,Base_Z] = sphere(20);
surf(Radius*Base_X+Center(1),...
    Radius*Base_Y+Center(2),...
    Radius*Base_Z+Center(3),'faceAlpha',0.3,'Facecolor','r')
neo_curv_sph = 1/Radius;
neo_rad = Radius
Y = (paleo.data(:, 1:3));
figure(5)
[Center,Radius] = sphereFit(Y);
plot3(Y(:,1),Y(:,2),Y(:,3),'r.')
hold on;daspect([1,1,1]);
[Base_X,Base_Y,Base_Z] = sphere(20);
surf(Radius*Base_X+Center(1),...
    Radius*Base_Y+Center(2),...
    Radius*Base_Z+Center(3),'faceAlpha',0.3,'Facecolor','g')
paleo_curv_sph = 1/Radius;
paleo_rad = Radius
```

APPENDIX D – DEVELOPMENT OF SCAPULAR BONE MODELS FOR FINITE ELEMENT ANALYSIS

OVERVIEW: *The following reports on the protocol to create finite element models from patient anatomy. This protocol uses the Materialize® suite (Mimics® and 3-Matic®); however, free-ware versions of medical image processing software, stereolithography editors and mesh generators can be used to produce many of these steps.*

Step 1: Segmenting and Thresholding CT DICOM Images and Three-Dimensional Bone Model Creation

A. Refer to Appendix B – Density and Porosity Measurement Protocol in Mimics®.

Step 2: Development of the CAD Implant, Reamer and Cement Mantle

B. Create implant models according to the desired dimensions in Solidworks®.

C. Increase the dimensions of the implant by at least 25%, and increase the length of the pegs and diameter by 1 mm. This will become the virtual bone 'reamer.'

D. Using the combine feature in Solidworks®, subtract sufficient volumes of the modified implant (with dilated peg diameters) and original implant to achieve the 1 mm cement mantle.

E. Save all models as binary STLs and load along with the scapula STL in 3-matic®.

Step 3: Alignment of the Components in 3-Matic® and Virtual Reaming in Meshlab

F. Align the implant in the desired position on the glenoid. Once aligned, use the 'plane-to-plane' align tool to align the reamer, and cement mantle. Note: since all parts should have been made using the same coordinate system in Solidworks®, the parts should align exactly (Figure D.1).

G. The reamer can now be used to virtual ream the glenoid surface. Export the aligned STLs and load in Meshlab. Boolean subtract the reamer STL from the scapula STL using the CSG operation. Adjust the parameters as desired.

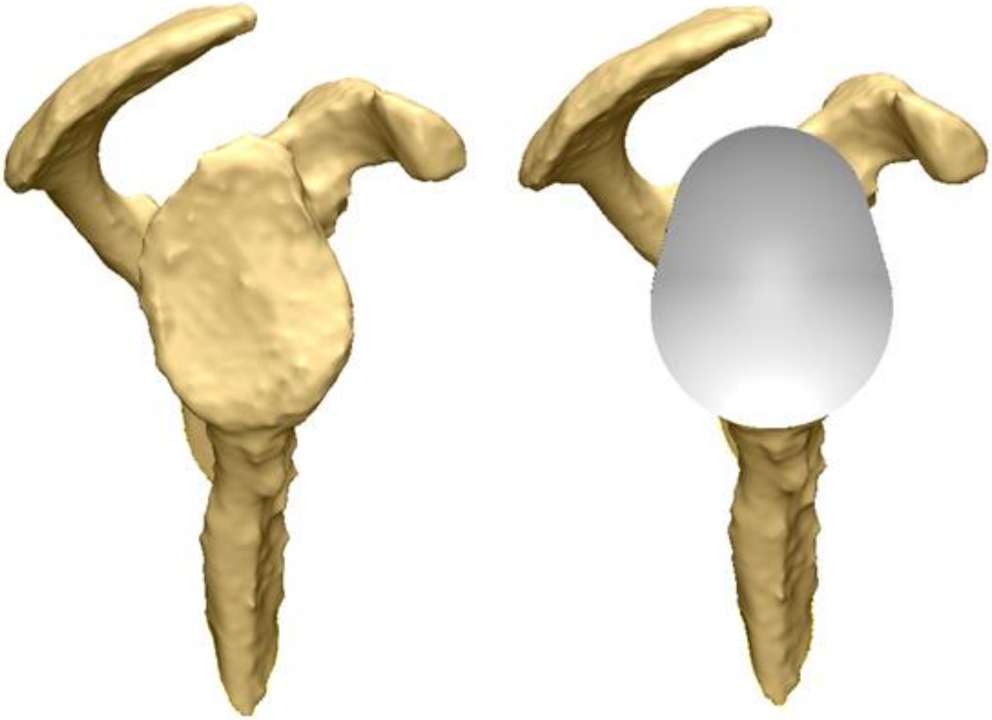

Figure D.1: Truncated scapula and aligned virtual bone reaming model in 3-Matic®

H. Load the subtracted scapula model back to 3-Matic®. The implant and cement mantle previously aligned should fit perfectly in the virtually reamed glenoid.

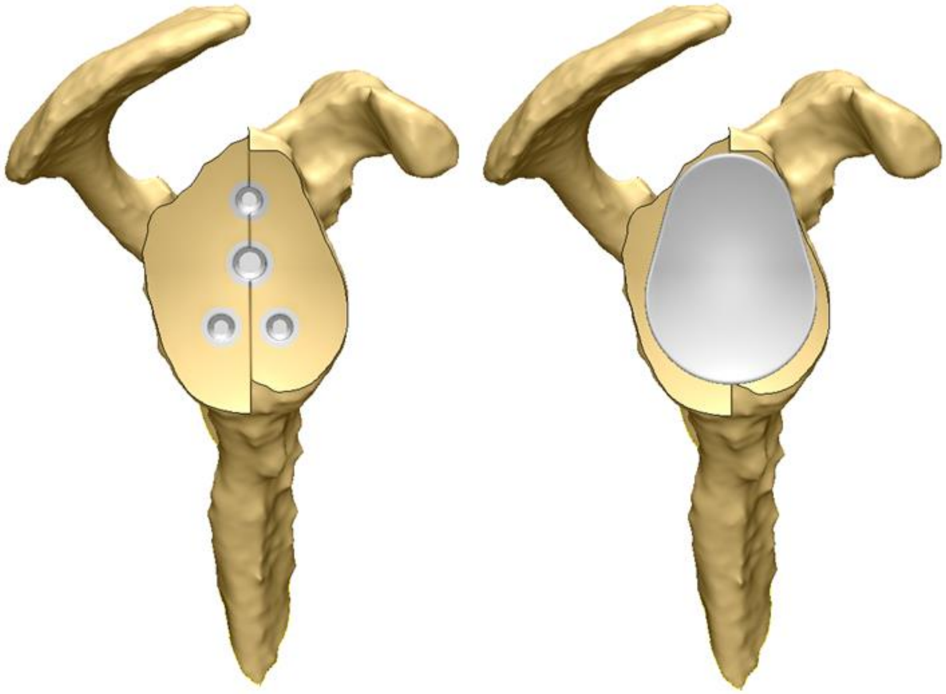

Figure D.2: Reamed scapula models with cement mantle and augmented implant

I. Auto Remesh the scapula using Height/Base (N) as the shape measure, and adjusting the parameters and maximum triangle edge length as desired. Ensure ‘preserve surface contours’ is selected. Use the fix wizard to improve the quality of the surface mesh.

J. Create volume mesh using Int and Refine. Make sure the desired maximum edge length is set. Once completed convert volume mesh from Tet4 to Tet10.

K. Copy and paste the reamed scapula from 3-matic® to Mimics®. Ensure the project is open in which the original dicoms are loaded. The scapula will appear under FEA mesh.

L. Change the units to grayvalues in Options → Preferences. Select FEA/CFD → Material and allow the calculating of grayvalues. Select uniform as the method and 399 materials (maximum). Fill in the dialogue as shown in Figure D.3.

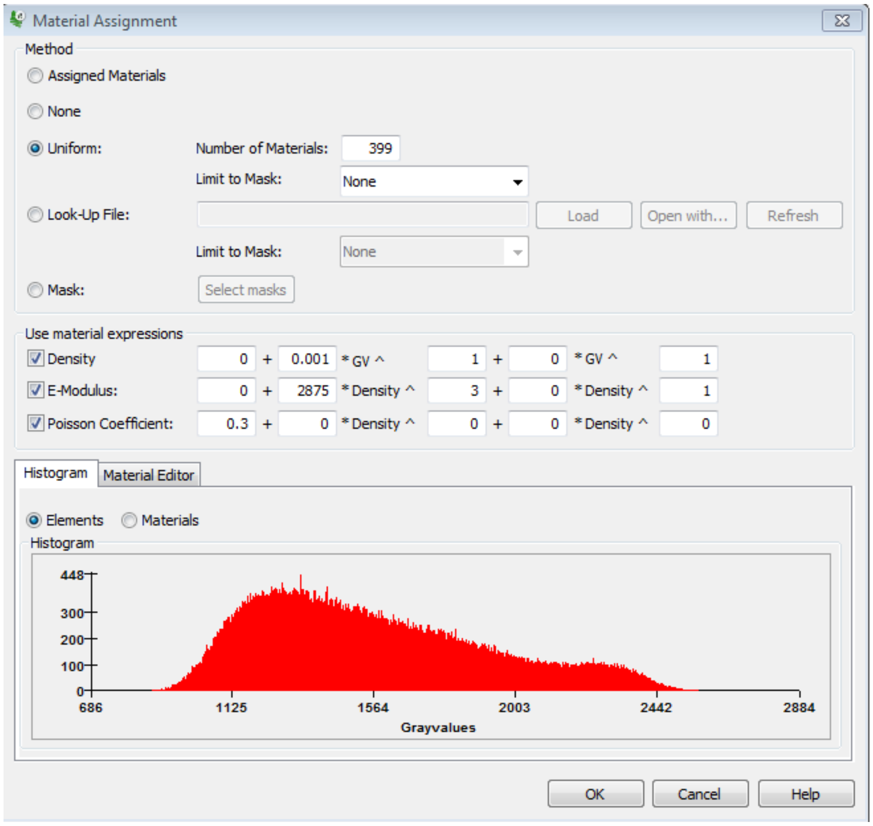

Material Assignment

Method

○ Assigned Materials

○ None

● Uniform: Number of Materials: 399

Limit to Mask: None

○ Look-Up File:

Limit to Mask: None

○ Mask:

Use material expressions

☑ Density 0 + 0.001 * GV ^ 1 + 0 * GV ^ 1

☑ E-Modulus: 0 + 2875 * Density ^ 3 + 0 * Density ^ 1

☑ Poisson Coefficient: 0.3 + 0 * Density ^ 0 + 0 * Density ^ 0

● Elements ○ Materials

Figure D.3: Material assignment in Mimics®

M. Export the model as an Abaqus file. Select Export → Abaqus…

N. Open the Abaqus INP file. Remove all materials that have a density greater than 1.85 g/cc. Set the final material to a density of 1.85 and a Elastic modulus of 20000 MPa. The last two lines of the material section of the INP should appear similar to below.

```
*MATERIAL, NAME=STEP_2MM_MAT226
*ELASTIC, TYPE=ISOTROPIC
18162.7,0.3
*DENSITY
1.84862,
**
*MATERIAL, NAME= STEP _2MM_MAT227
*ELASTIC, TYPE=ISOTROPIC
20000,0.3
*DENSITY
1.85,
**
** End of Data
```

O. Now that the materials have been edited, the corresponding elements and nodes must be modified. The elements are listed by number followed by the ten nodes connected to this element. Each element set is assigned a separate section and a corresponding material, as determined in Mimics®. In this case all elements from 227 to 399 should be assigned MAT227. Cut and paste all elements from these sections and replace all of the header information using any text editor. When completed copy all the elements and corresponding nodes back under the MAT227 header in the original INP file. An example of the header information and the first element is shown below.

```
*SOLID SECTION, ELSET=STEP_2MM_VOLUME1, MATERIAL=STEP_2MM_MAT1
*ELEMENT, TYPE=C3D10, ELSET=STEP_2MM_VOLUME1
1,22481,22482,22483,16255,22484,22485,22486,22487,22488,22489
```

P. This inp file can now be loaded in Abaqus for analysis. The implant and cement mantle will need to be loaded as STEP files and can be saved as such in Solidworks®. Note this may require positioning in abaqus, as the Solidworks® coordinate system differs from 3-Matic®.

APPENDIX E – COPYRIGHT RELEASES

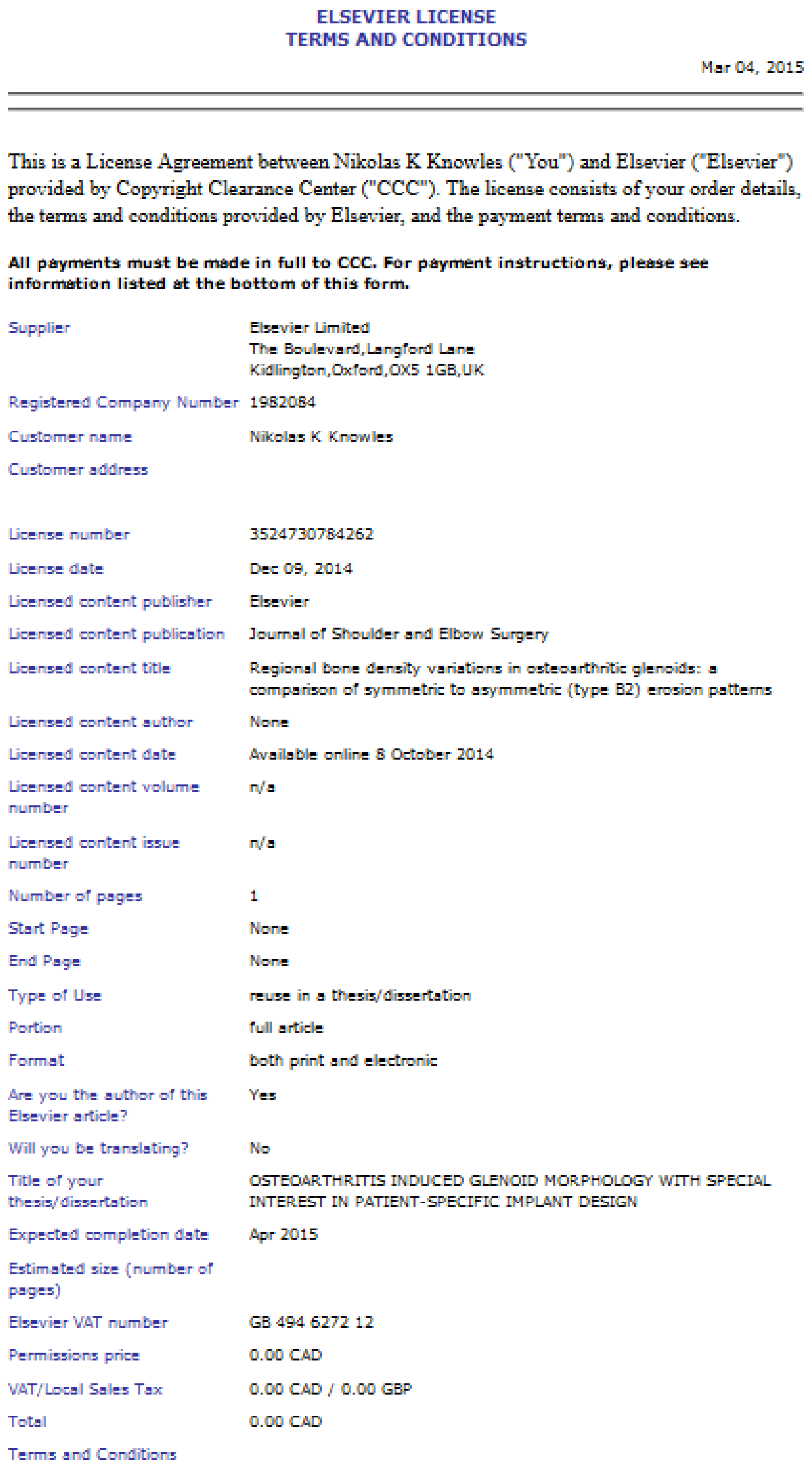

ELSEVIER LICENSE
TERMS AND CONDITIONS

Mar 04, 2015

This is a License Agreement between Nikolas K Knowles ("You") and Elsevier ("Elsevier") provided by Copyright Clearance Center ("CCC"). The license consists of your order details, the terms and conditions provided by Elsevier, and the payment terms and conditions.

All payments must be made in full to CCC. For payment instructions, please see information listed at the bottom of this form.

Supplier	Elsevier Limited The Boulevard,Langford Lane Kidlington,Oxford,OX5 1GB,UK
Registered Company Number	1982084
Customer name	Nikolas K Knowles
Customer address	
License number	3524730784262
License date	Dec 09, 2014
Licensed content publisher	Elsevier
Licensed content publication	Journal of Shoulder and Elbow Surgery
Licensed content title	Regional bone density variations in osteoarthritic glenoids: a comparison of symmetric to asymmetric (type B2) erosion patterns
Licensed content author	None
Licensed content date	Available online 8 October 2014
Licensed content volume number	n/a
Licensed content issue number	n/a
Number of pages	1
Start Page	None
End Page	None
Type of Use	reuse in a thesis/dissertation
Portion	full article
Format	both print and electronic
Are you the author of this Elsevier article?	Yes
Will you be translating?	No
Title of your thesis/dissertation	OSTEOARTHRITIS INDUCED GLENOID MORPHOLOGY WITH SPECIAL INTEREST IN PATIENT-SPECIFIC IMPLANT DESIGN
Expected completion date	Apr 2015
Estimated size (number of pages)	
Elsevier VAT number	GB 494 6272 12
Permissions price	0.00 CAD
VAT/Local Sales Tax	0.00 CAD / 0.00 GBP
Total	0.00 CAD
Terms and Conditions	

ELSEVIER LICENSE
TERMS AND CONDITIONS

Mar 04, 2015

This is a License Agreement between Nikolas K Knowles ("You") and Elsevier ("Elsevier") provided by Copyright Clearance Center ("CCC"). The license consists of your order details, the terms and conditions provided by Elsevier, and the payment terms and conditions.

All payments must be made in full to CCC. For payment instructions, please see information listed at the bottom of this form.

Supplier	Elsevier Limited The Boulevard,Langford Lane Kidlington,Oxford,OX5 1GB,UK
Registered Company Number	1982084
Customer name	Nikolas K Knowles
Customer address	
License number	3524730902110
License date	Dec 09, 2014
Licensed content publisher	Elsevier
Licensed content publication	Journal of Shoulder and Elbow Surgery
Licensed content title	Quantification of the position, orientation, and surface area of bone loss in type B2 glenoids
Licensed content author	None
Licensed content date	Available online 29 October 2014
Licensed content volume number	n/a
Licensed content issue number	n/a
Number of pages	1
Start Page	None
End Page	None
Type of Use	reuse in a thesis/dissertation
Intended publisher of new work	other
Portion	full article
Format	both print and electronic
Are you the author of this Elsevier article?	Yes
Will you be translating?	No
Title of your thesis/dissertation	OSTEOARTHRITIS INDUCED GLENOID MORPHOLOGY WITH SPECIAL INTEREST IN PATIENT-SPECIFIC IMPLANT DESIGN
Expected completion date	Apr 2015
Estimated size (number of pages)	
Elsevier VAT number	GB 494 6272 12
Permissions price	0.00 CAD
VAT/Local Sales Tax	0.00 CAD / 0.00 GBP
Total	0.00 CAD
Terms and Conditions	

ELSEVIER LICENSE
TERMS AND CONDITIONS

Mar 04, 2015

This is a License Agreement between Nikolas K Knowles ("You") and Elsevier ("Elsevier") provided by Copyright Clearance Center ("CCC"). The license consists of your order details, the terms and conditions provided by Elsevier, and the payment terms and conditions.

All payments must be made in full to CCC. For payment instructions, please see information listed at the bottom of this form.

Supplier	Elsevier Limited The Boulevard,Langford Lane Kidlington,Oxford,OX5 1GB,UK
Registered Company Number	1982084
Customer name	Nikolas K Knowles
Customer address	
License number	3581871449447
License date	Mar 04, 2015
Licensed content publisher	Elsevier
Licensed content publication	Journal of Shoulder and Elbow Surgery
Licensed content title	Augmented glenoid component designs for type B2 erosions: a computational comparison by volume of bone removal and quality of remaining bone
Licensed content author	None
Licensed content date	Available online 31 January 2015
Licensed content volume number	n/a
Licensed content issue number	n/a
Number of pages	1
Start Page	None
End Page	None
Type of Use	reuse in a thesis/dissertation
Intended publisher of new work	other
Portion	full article
Format	both print and electronic
Are you the author of this Elsevier article?	Yes
Will you be translating?	No
Title of your thesis/dissertation	OSTEOARTHRITIS INDUCED GLENOID MORPHOLOGY WITH SPECIAL INTEREST IN PATIENT-SPECIFIC IMPLANT DESIGN
Expected completion date	Apr 2015
Estimated size (number of pages)	
Elsevier VAT number	GB 494 6272 12
Permissions price	0.00 CAD
VAT/Local Sales Tax	0.00 USD / 0.00 GBP
Total	0.00 CAD
Terms and Conditions	

APPENDIX F – ETHICS APPROVALS

Washington University in St.Louis

Human Research Protection Office

Barnes Jewish Hospital
St. Louis Children's Hospital
Washington University

IRB ID# 201401059

To:	Jay Keener	
From:	The Washington University in St. Louis Institutional Review Board,	
	WUSTL	DHHS Federalwide Assurance #FWA00002284
	BJH	DHHS Federalwide Assurance #FWA00002281
	SLCH	DHHS Federalwide Assurance #FWA00002282
Re:	An anatomic study on the orientation, location and volume of posterior glenoid bone loss associated with osteoarthritis.	

Approval Date: 02/04/14

Next IRB Approval

Due Before: 02/03/15

Type of Application:	**Type of Application Review:**	**Approved for Populations:**
☒ New Project	☐ Full Board:	☐ Children
☐ Continuing Review parent	Meeting Date:	☐ Signature from one
☐ Modification parents	☒ Expedited	☐ Signature from two
	☐ Exempt	☐ Prisoners
Fetuses, Neonates	☐ Facilitated	☐ Pregnant Women,
		☐ Wards of State

☐ Decisionally Impaired

MATERIALS APPROVED

This approval has been electronically signed by IRB Chair or Chair Designee:

Mitchell Saulisbury-Robertson, BA, BA

02/04/14 2337

IRB Approval: IRB approval indicates that this project meets the regulatory requirements for the protection of human subjects. IRB approval does not absolve the principal investigator from complying with other institutional, collegiate, or departmental policies or procedures.

Recruitment/Consent: Your IRB application has been approved for recruitment of subjects not to exceed the number indicated on your application form. If you are using written informed consent, the IRB-approved and stamped Informed Consent Document(s) are available in *my*IRB. The original signed Informed Consent Document should be placed in your research files. A copy of the Informed Consent Document should be given to the subject. (A copy of the *signed* Informed Consent Document should be given to the subject if your Consent contains a HIPAA authorization section.)

Continuing Review: Federal regulations require that the IRB re-approve research projects at intervals appropriate to the degree of risk, but no less than once per year. This process is called "continuing review." Continuing review for non-exempt research is required to occur as long as the research remains active for long-term follow-up of research subjects, even when the research is permanently closed to enrollment of new subjects and all subjects have completed all research-related interventions and to occur when the remaining research activities are limited to collection of private identifiable information. Your project "expires" at midnight on the date indicated on the preceding page ("Next IRB Approval Due on or Before"). You must obtain your next IRB approval of this project by that expiration date. You are responsible for submitting a Continuing Review application in sufficient time for approval before the expiration date, however you will receive reminder notice prior to the expiration date.

Modifications: Any change in this research project or materials must be submitted on a Modification application to the IRB for prior review and approval, except when a change is necessary to eliminate apparent immediate hazards to subjects. The investigator is required to promptly notify the IRB of any changes made without IRB approval to eliminate apparent immediate hazards to subjects using the Modification/Update Form. Modifications requiring the prior review and approval of the IRB include but are not limited to: changing the protocol or study procedures, changing investigators or funding sources, changing the Informed Consent Document, increasing the anticipated total number of subjects from what was originally approved, or adding any new materials (e.g., letters to subjects, ads, questionnaires).

Unanticipated Problems Involving Risks: You must promptly report to the IRB any unexpected adverse experience, as defined in the IRB/HRPO policies and procedures, and any other unanticipated problems involving risks to subjects or others. The Reportable Events Form (REF) should be used for reporting to the IRB.

Audits/Record-Keeping: Your research records may be audited at any time during or after the implementation of your project. Federal and University policies require that all research records be maintained for a period of seven (7) years following the close of the research project. For research that involves drugs or devices seeking FDA approval, the research records must be kept for a period of three years after the FDA has taken final action on the marketing application, if that is longer than seven years.

Additional Information: Complete information regarding research involving human subjects at Washington University is available in the "Washington University Institutional Review Board Policies and Procedures." Research investigators are expected to comply with these policies and procedures, and to be familiar with the University's Federalwide Assurance, the Belmont Report, 45CFR46, and other applicable regulations prior to conducting the research. This document and other important information is available on the HRPO website http://hrpohome.wustl.edu/.

Western
Research

Research Ethics

Use of Human Participants - Initial Ethics Approval Notice

Principal Investigator: Dr. George Athwal
File Number:104316
Review Level: Delegated
Protocol Title: An anatomic study on the orientation, location and volume of posterior glenoid bone loss associated with osteoarthritis.
Department & Institution: Schulich School of Medicine and Dentistry\Surgery,St. Joseph's Health Care London
Sponsor:
Ethics Approval Date: October 08, 2013 **Expiry Date:**August 31, 2014
Documents Reviewed & Approved & Documents Received for Information:

Document Name	Comments	Version Date
Instruments	data form collection	2013/08/01
Western University Protocol		2013/08/30
Other	Database Questions	2013/09/23
Recommendations Form	Recommendations	2013/09/20

This is to notify you that The University of Western Ontario Research Ethics Board for Health Sciences Research Involving Human Subjects (HSREB) which is organized and operates according to the Tri-Council Policy Statement: Ethical Conduct of Research Involving Humans and the Health Canada/ICH Good Clinical Practice Practices: Consolidated Guidelines; and the applicable laws and regulations of Ontario has reviewed and granted approval to the above referenced revision(s) or amendment(s) on the approval date noted above. The membership of this REB also complies with the membership requirements for REB's as defined in Division 5 of the Food and Drug Regulations.

The ethics approval for this study shall remain valid until the expiry date noted above assuming timely and acceptable responses to the HSREB's periodic requests for surveillance and monitoring information. If you require an updated approval notice prior to that time you must request it using the University of Western Ontario Updated Approval Request Form.

Members of the HSREB who are named as investigators in research studies, or declare a conflict of interest, do not participate in discussion related to, nor vote on, such studies when they are presented to the HSREB.

The Chair of the HSREB is Dr. Joseph Gilbert. The HSREB is registered with the U.S. Department of Health & Human Services under the IRB registration number IRB 00000940.

Ethics Officer to Contact for Further Information

___ Erika Basile (ebasile@uwo.ca)	___ Grace Kelly (grace.kelly@uwo.ca)	[✓ Vikki Tran] (vikki.tran@uwo.ca)

This is an official document. Please retain the original in your files.

Western University, Research, Support Services Bldg., Rm. 5150
London, ON, Canada N6A 3K7 t. 519.661.3036 f. 519.850.2466 www.uwo.ca/research/services/ethics

Nikolas Kelton Knowles

BEng (Biomed Mech)
MESc Candidate

Curriculum Vitae

Affiliation:	Roth|McFarlane Hand and Upper Limb Centre St. Joseph's Health Care, London, ON

Education

2013 -	**Master of Engineering Science (MESc), Mechanical Engineering** Graduate program in Mechanical and Materials Engineering Collaborative Program in Musculoskeletal Health Research The University of Western Ontario, London, ON **Supervisor: Dr. Louis M. Ferreira** **Expected Completion: April 2015**
2009 - 2013	**Bachelor of Engineering (BEng – High Distinction), Biomedical and Mechanical Engineering** Carleton University, Ottawa, ON
2006 - 2009	**Advanced College Diploma (Honours), Mechanical Engineering Technology** Algonquin College, Ottawa, ON
2004 - 2005	**College Certificate, General Arts and Science** Fanshawe College, London, ON

Employment History

2013 -	**Research Assistant, Orthopaedic Research** Roth|McFarlane Hand and Upper Limb Centre St. Josephs Health Care, London, ON Supervisor: Dr. Louis M. Ferreira

2013 -	**Laboratory Machining Support** Roth|McFarlane Hand and Upper Limb Centre St. Josephs Health Care, London, ON Supervisor: Dr. Louis M. Ferreira
2012 (Summer)	**Research Assistant, Orthopaedic Research** Roth|McFarlane Hand and Upper Limb Centre St. Josephs Health Care, London, ON Supervisor: Dr. Louis M. Ferreira

Professional Memberships

2013 -	Professional Engineers of Ontario (PEO) – Engineer in Training (EIT)
2011 -	American Society of Mechanical Engineers (ASME) – Bioengineering Division

Societies/Committees

Dec. 2014 -	Bone and Joint Institute Communications Committee – The University of Western Ontario
Sept. 2014 -	Founder/President – Mechanical and Materials Engineering Graduate Student Society – The University of Western Ontario
Sept. 2014 -	Graduate Student Representative - Mechanical and Materials Engineering Graduate Student Society – The University of Western Ontario
June 2014 -	Society of Graduate Students (SOGS) Policy Committee Member – The University of Western Ontario

Academic Awards/Scholarships

2015	Dr. Suzanne Bernier Memorial Award in Skeletal Biology – Western University

2015	Best Poster, Shoulder and Elbow Classification, American Academy of Orthopaedic Surgeons (AAOS) Annual Meeting, Las Vegas, NV
2013 - 2015	Joint Motion Program (JuMP) CIHR Fellowship in Musculoskeletal Health Research and Leadership
2013 - 2015	Western Graduate Research Scholarship, The University of Western Ontario
2012	Western Engineering Summer Research Award (WESRA), The University of Western Ontario
2011	Carleton Academic Scholarship, Carleton University
2010	Sprott Scholarship, Carleton University
2009	Carleton Academic Scholarship, Carleton University
2009	Alstom Power Canada Inc. Award
2008	Ontario International Education Opportunity Scholarship (OIEOS)
2005- 2009	Lanxess Higher Education Scholarship

Peer-Reviewed Manuscripts

1. Ferreira, L.M., **Knowles, N.K.**, Richmond, D., Athwal, G.S. Effectiveness of CT for the Detection of Graft Resorption Following Reverse Shoulder Arthroplasty. Orthopaedics and Traumatology: Surgery & Research. Accepted Mar. 9, 2015

2. **Knowles, N.K.**, Ferreira, L.M., Athwal G.S. A Comparison of Augmented Glenoid Component Designs for Type B2 Erosions: A Computational Comparison by Volume of Bone Removal, and Quality of Remaining Bone. Journal of Shoulder and Elbow Surgery. In-Press, Available Online Jan. 31, 2015

3. **Knowles, N.K.**, Keener J.D., Ferreira, L.M., Athwal G.S. Quantification of the Position, Orientation and Surface Area of Posterior Bone loss in Type B2 Glenoids. Journal of Shoulder and Elbow Surgery. 2015;24(4):503-510

4. **Knowles, N.K.**, Athwal G.S., Keener J.D., Ferreira, L.M. Regional Bone Density Variations in Osteoarthritic Glenoids: A Comparison of Symmetric to

Asymmetric (Type B2) Erosion Patterns. Journal of Shoulder and Elbow Surgery 2015; 24(3):425-432

Invited Presentations

1. **Knowles, N.K.**, Ferreira, L.M., Jay D. Keener, George S. Athwal. (March 2015) Quantification of the Position, Orientation and Surface Area of Posterior Bone Loss in Type B2 Glenoids. 61st Annual Meeting of the Orthopaedic Research Society. Las Vegas, NV. (International) (Poster) (MESc).

Abstracts/Presentation at Conferences/Professional Meetings

1. **Knowles, N.K.**, Ferreira, L.M., Jay D. Keener, George S. Athwal. (June 2015) Quantification of the Position, Orientation and Surface Area of Posterior Bone Loss in Type B2 Glenoids. 2015 Annual Meeting of the Canadian Orthopaedic Association (COA). Vancouver, BC. (International) (Podium) (MESc)
2. **Knowles, N.K.**, Ferreira, L.M., George S. Athwal. (June 2015) A Comparison of Augmented Glenoid Component Designs for Type B2 Erosions: Evaluation by Volume of Bone Removal, and Quality of Remaining Bone. 2015 Annual Meeting of the Canadian Orthopaedic Association (COA). Vancouver, BC. (International) (Podium) (MESc)
3. **Knowles, N.K.**, Carroll, M.C., Ferreira, L.M., Jay D. Keener, George S. Athwal. (June 2015) An Anatomic Study of Normal and Osteoarthritic Humeral Head Size. 2015 Annual Meeting of the Canadian Orthopaedic Research Society (CORS). Vancouver, BC. (International) (Podium) (MESc)
4. **Knowles, N.K.**, Ferreira, L.M., Jay D. Keener, George S. Athwal. (June 2015) Regional Bone Density Variations in Osteoarthritic Glenoids: A Comparison of Symmetric to Asymmetric (Type B2) Erosion Patterns. 2015 Annual Meeting of the Canadian Orthopaedic Research Society (CORS). Vancouver, BC. (International) (Podium) (MESc)
5. **Knowles, N.K.**, Ferreira, L.M., Jay D. Keener, George S. Athwal. (June 2015) Quantification of the Position, Orientation and Surface Area of Posterior Bone Loss in Type B2 Glenoids. 2015 Annual Meeting of the Canadian Orthopaedic Research Society (CORS) and Canadian Orthopaedic Association (COA). Vancouver, BC. (International) (Poster) (MESc)

6. **Knowles, N.K.**, Ferreira, L.M., George S. Athwal. (June 2015) A Comparison of Augmented Glenoid Component Designs for Type B2 Erosions: Evaluation by Volume of Bone Removal, and Quality of Remaining Bone. 2015 Annual Meeting of the Canadian Orthopaedic Research Society (CORS) and Canadian Orthopaedic Association (COA). Vancouver, BC. (International) (Poster) (MESc)

7. **Knowles, N.K.**, Ferreira, L.M., Jay D. Keener, George S. Athwal. (June 2015) Regional Bone Density Variations in Osteoarthritic Glenoids: A Comparison of Symmetric to Asymmetric (Type B2) Erosion Patterns. 2015 Annual Meeting of the Canadian Orthopaedic Association (COA). Vancouver, BC. (International) (Poster) (MESc)

8. **Knowles, N.K.**, Ferreira, L.M., Jay D. Keener, George S. Athwal. (March 2015) Quantification of the Position, Orientation and Surface Area of Posterior Bone Loss in Type B2 Glenoids. 2015 Annual Meeting of the American Academy of Orthopaedic Surgeons (AAOS). Las Vegas, NV. (International) (Poster) (MESc)

9. **Knowles, N.K.**, George S. Athwal, Jay D. Keener, Ferreira, L.M. (October 2014) Regional Bone Density Variations in Osteoarthritic Glenoids: A Comparison of Symmetric to Asymmetric (Type B2) Erosion Patterns. American Shoulder and Elbow Surgeons Closed Meeting. Pinehurst, NC (International) (Poster) (MESc)

10. **Knowles, N.K.**, George S. Athwal, Jay D. Keener, Ferreira, L.M. (July 2014) Morphology and Density Variations in Osteoarthritic Glenoids.7th World Congress of Biomechanics, Boston, MA (International) (Poster) (MESc)

11. **Knowles, N.K.**, Gladwell, M., Ferreira, L.M. (June 2014) An Intra-Bone Axial Load Transducer: Development and Validation in an In-Vitro Radius Model. The Combined Meeting of the AOA/COA - CORS 2014, Montreal, QC (International) (Poster) (MESc)

12. **Knowles, N.K.**, Richmond, D., Athwal, G.S., Ferreira, L.M. (June 2014) Computed Tomography is Ineffective in Detecting Glenoid Bone graft Resorption Following Reverse Shoulder Arthroplasty. The Combined Meeting of the AOA/COA - CORS 2014. Montreal, QC (International) (Podium) (MESc)

13. **Knowles, N.K.**, Ferreira, L.M., Richmond, D., Athwal, G.S. (Mar 2014) The Effectiveness of CT to Determine Bone Graft Resorption After BIO-RSA. 60th Annual Meeting of the Orthopaedic Research Society. New Orleans, LA (International) (Poster) (MESc)

14. **Knowles, N.K.**, Gladwell, M., Ferreira, L.M. (Jan 2014) An Intra-Bone Axial Load Transducer: Development and Validation in an In-Vitro Radius Model. Bone and Joint Injury and Repair (BAJIR) Conference. London, ON (National) (Podium) (MESc)